The Dissertation Committee for Erik Rist Larson Certifies that this is the approved version of the following dissertation:

Admittance Measurement for Assessment of Cardiac Hemodynamics in Clinical and Research Applications

Committee:

John A. Pearce, Supervisor

Jonathan W. Valvano

Ali Yilmaz

H. Grady Rylander

Marc D. Feldman

Admittance Measurement for Assessment of Cardiac Hemodynamics in Clinical and Research Applications

by

Erik Rist Larson, B.S.E.E; M.S.E.

Dissertation

Presented to the Faculty of the Graduate School of

The University of Texas at Austin

in Partial Fulfillment

of the Requirements

for the Degree of

Doctor of Philosophy

The University of Texas at Austin

May, 2012

Dedication

This work is dedicated to my parents, who have always supported me.

Acknowledgements

I would like to thank the many people who have helped me throughout my graduate studies.

Dr. Pearce has taught me nearly everything I know about instrumentation and electromagnetics. All of the analysis and design in this work has come from something Dr. Pearce taught me. I find myself extremely lucky to have benefited from his years of experience. I really value my time as a teaching assistant for Dr. Pearce's biomedical electronics course that over the years has allowed me to refine my understanding of instrumentation through interactions with Dr. Pearce and students.

Dr. Valvano has taught me a great deal about instrumentation and embedded systems. His courses taught me some of the most practical and useful engineering skills I know. I am thankful for his guidance in the design of instrumentation, experiment planning and analysis, and overall excitement for the project.

Dr. Feldman has always enthusiastically driven our experiments. His ideas and insights give us applications to apply engineering tools. None of our experiments would be possible without him.

Dr. Rylander has taught me how to effectively convey skills to students in his instrumentation course. I am thankful he has allowed me to serve as his teaching assistant each spring. Interactions with students has helped develop my understanding of analog design and sharpened my debugging skills.

John Porterfield has helped me throughout my graduate career. I have learned a great deal from him in the courses we took together and many experiments over the years. I am especially thankful for John's skills at following and updating the

experimental protocol in my experiments. The procedure was extremely complicated, and I would not have been able to keep track of everything without him. I am also grateful for John as a resource when conducting literature reviews.

Karthik Raghavan, Lev Shuhatovich, and Katy Loeffler were all members of our research group. Karthik taught me many things about our labs research area when I started graduate school. I learned a great deal about instrumentation on our trips to San Antonio to perform experiments. Lev introduced me to many methods for design, soldering and fabrication. I especially appreciate him teaching me to use industry-standard PCB software. Katy joined our lab group in the last two years of my studies. Despite being a new member, she helped me evaluate design ideas and analyze experimental results.

I would also like to thank everyone at the University of Texas Health Science Center at San Antonio, and especially Danny Escobedo, Travis Jenkins, Marmol Velez, and Kelsey Johnson. Danny's amazing surgical skills allow us to perform many complex experiments. Travis's help setting up and running experiments was greatly appreciated. Marmol taught me many things about cardiac physiology, arrhythmias, and pacing. He found ways to perform many procedures in our experiments. Kelsey's close attention to detail was of immense help and prevented us from straying from the protocol on multiple occasions.

Finally, I would like to thank my parents and my brother for continually supporting me throughout the years. They have always encouraged me to pursue my studies; I wouldn't be where I am today without them.

Admittance Measurement for Assessment of Cardiac Hemodynamics in Clinical and Research Applications

Erik Rist Larson, Ph.D.

The University of Texas at Austin, 2012

Supervisor: John A. Pearce

The admittance method is an important tool for the indirect determination of cardiac hemodynamics in animal research and has clinical potential as a hemodynamic monitor for implantable cardioverter-defibrillators (ICDs). Animal studies use a conductance catheter to determine left-ventricular (LV) volume, but ICDs must make use of existing pacing leads to perform an admittance measurement. This work aims to further the use of the admittance method by extending its use to multi-segment conductance catheters, determining parasitic circuit element's effects on electric property measurements, using biventricular pacing leads to determine cardiac hemodynamics, and analysis of spatial sensitivity using finite element models in various configurations. Experimental results show the admittance method can be used to determine LV stroke volume with biventricular pacing leads. Modeling results show removal of the muscle component focuses the measurement's spatial sensitivity towards the left-ventricular blood pool.

Table of Contents

List of Tables x

List of Figures xii

Chapter 1: Background and Motivation 1

1.1 Specific Aims 2

1.2 Background and Significance 3

Chapter 2: Five-Segment Admittance Catheter Measurements 10

2.1 Instrumentation 12

2.2 Experiment Protocol 12

2.3 Parallel Conductance Removal 12

2.4 Analysis and Measurement Results 13

2.5 Discussion 15

Chapter 3: Complex Muscle Property Measurements 16

3.1 Murine Infarct Muscle Properties 16

3.2 Tetrapolar Measurement Circuit Model 20

3.3 Active Surface Probes 28

3.4 Discussion 39

Chapter 4: Cardiac Hemodynamic Monitoring with Biventricular Pacing Leads 42

4.1 Simplified Series Model Derivation 42

4.2 Instrument Design 44

4.3 Methods 49

4.4 Data Analysis 53

4.5 Results 55

4.6 Discussion 61

4.7 Conclusion 65

Chapter 5: Finite Element Modeling Studies of the Admittance Method 66
5.1 Tetrapolar Measurements In Uniform Media 67
5.2 Conductance Catheter In The Mouse LV 80
5.3 Multi-segment Catheters 89
5.4 Cross-Chamber Measurements 97
5.5 MRI Study 120
5.6 Discussion 122
Chapter 6: Conclusion 124
Appendix 126
A - Porcine Conductance Catheter Data and Analysis 126
B - Infarct Data and Analysis 126
C - Tetrapolar Circuit Models 126
D - Active Surface Probe Design and Analysis 127
E - Biventricular Impedance and Pacing Instrument Design Files 127
F - Stroke Volume Monitoring Experimental Results 127
G - Finite Element Models 128
References 129

List of Tables

Table 1: P-values for infarct vs. hypertrophic zone paired t-test 20

Table 2: Phantom formula 32

Table 3: Mean difference and standard deviation of phantom properties 34

Table 4: Canine myocardial property measurements.....39

Table 5: Mesh statistics for tetrapolar measurement in uniform media.....67

Table 6: Mesh statistics for murine LV model at 45 μL.....81

Table 7: Mouse model subdomain properties.....83

Table 8: Mouse catheter model G_b and G_m.....87

Table 9: Mouse model with surroundings results.....88

Table 10: Mouse model relative resistive losses.....89

Table 11: Mesh statistics for multi-segment catheter 91

Table 12: Multi-segment catheter subdomain properties.....92

Table 13: Approximate Heart Geometry Dimensions. 98

Table 14: Mesh statistics for approximate heart geometry.....99

Table 15: Model electric properties 100

Table 16: Relative contributions using parallel and series models.....103

Table 17: Relative contributions from each subdomain to $\mathrm{Re}\{\mathbf{Z}\}$ and R_b 105

Table 18: Approximate heart geometry cyclic variation 105

Table 19: Systolic and diastolic measurements 106

Table 20: RV lead motion model measurements.....107

Table 21: Measurement sensitivity to atrium geometry 109

Table 22: Comparison of cross-chamber measurements with and without a shocking lead.....113
Table 23: Relative contribution to Re{Z_G} with various electrode spacings 114
Table 24: Relative contribution to R_b with various electrode spacings.....115
Table 25: Real part of Geselowitz impedance with different electrode spacings 115
Table 26: R_b from the Geselowitz impedance with different electrode spacings 115
Table 27: Relative contribution to Re{Z_G} for all electrodes down lateral wall .117
Table 28: Relative contribution to R_b for electrodes in AV groove and lateral wall118
Table 29 Real part of Geselowitz impedance for tetrapolar LCV lead down lateral wall.....118
Table 30: R_b from the Geselowitz impedance for electrodes in AV groove and lateral wall.....119
Table 31: Mesh statistics for MRI study with 2 cm LCV electrode spacing at diastole 121
Table 32: 2cm LCV electrode spacing measurements with MRI model.....122
Table 33: 0.5 cm LCV electrode spacing measurements with MRI model.....122

List of Figures

Figure 1: Cross-chamber series circuit model 9

Figure 2: Catheter and circuit interface 10

Figure 3: Admittance measurement in complex plane 12

Figure 4: Large animal pressure-volume loops 14

Figure 5: Time-varying blood and muscle conductance.....14

Figure 6: Infarct probe penetration depth 18

Figure 7: Infarct mice muscle properties 19

Figure 8: Infarct mice sigma to epsilon ratio.....19

Figure 9: a) Complete and b) effective circuit models 21

Figure 10: Electrode circuit model at 20 kHz.....22

Figure 11: Impedance magnitude *vs.* frequency. Z_E = 152 + (33 pF || 595) Ω and C_p = 50 pF.....23

Figure 12: Impedance phase *vs.* frequency. Z_E = 152 + (33 pF || 595) Ω and C_p = 50 pF.....24

Figure 13: Tetrapolar model sensitivity to electrode impedance.....25

Figure 14: Tetrapolar model sensitivity to wire capacitance.....25

Figure 15: Tetrapolar model sensitivity to wire inductance 26

Figure 16: Scisense surface probe with Cp = 160 pF and 55 pF 27

Figure 17: Measured and modeled probe capacitance *vs.* conductivity.....28

Figure 18: Active surface probe current source.....29

Figure 19: Active Surface Probe.....30

Figure 20: Saline calibration for passive and active probes 31

Figure 21: Phantom conductivity and relative permittivity vs. frequency.....32
Figure 22: Test cell with phantom 34
Figure 23: Conductivity and permittivity linearity plots 35
Figure 24: Bland-Altman plots of phantom property measurements.....36
Figure 25: Probe permittivity error changed with field form factor and solution conductivity.....37
Figure 26: Canine conductivity and permittivity measurements 38
Figure 27: Canine conductivity to permittivity ratio measurements 39
Figure 28: Series blood and muscle circuit model.....42
Figure 29: In-phase and Quadrature Waveform Generation.....45
Figure 30: All-pass filter used to zero phase offset 46
Figure 31: Printed circuit board and enclosed instrument 47
Figure 32: Pacing circuit.....48
Figure 33: Pacemaker Interface 48
Figure 34: Biventricular pacing leads.....50
Figure 35**:** Biventricular lead measurement configurations.....50
Figure 36: Simulated Ventricular Tachycardia Examples.....56
Figure 37: Acquired signals at baseline and ventricular fibrillation.....57
Figure 38: Example data at baseline, AOO pacing, and dopamine infusion 58
Figure 39**:** (a) ΔG_b vs. SV measured from the RV to LCV and (b) ΔG_b vs. SV measured from the RA to LCV.....59
Figure 40**:** Calibrated data for (a) ΔG_b and (b) $\Delta|Y|$ vs. SV measured from the RV to LCV.....60
Figure 41: $|Y|$, G_b and LV volume during IVC Occlusion.....61
Figure 42**:** Volume from G_b vs. Volume for IVC occlusions**.**.....61

Figure 43: Geometry for tetrapolar measurement in uniform media 67
Figure 44: Cross section of tetrapolar measurement mesh 68
Figure 45: Tetrapolar model potential distribution (mV) 69
Figure 46: Tetrapolar model current density distribution (mA/m^2) with streamlines 69
Figure 47: Impedivity-sensitivity product for tetrapolar measurement (MΩ/m^3) .74
Figure 48: $\log_{10}$|impedivity-sensitivity product| ($\log_{10}$(MΩ/m^3)) for tetrapolar measurement 75
Figure 49: Equivalent circuit model as seen by a tetrapolar measurement.....76
Figure 50: Current density streamlines in negative and positive sensitivity zones78
Figure 51: Relative sensitivity zones with impedance sensitivities (%).....79
Figure 52: Equipotential contours with relative potential sensitivities [%].....80
Figure 53: Mouse catheter subdomains 81
Figure 54: Cross section of murine mesh at 45 μL 82
Figure 55: Mouse catheter subdomains with surroundings 83
Figure 56: Product of impedivity and sensitivity (top) and the product of G_b and sensitivity (bottom) at 15 μL (μS/m^3) 84
Figure 57: $\log_{10}$|impedivity · sensitivity| (top) and the $\log_{10}$|G_b · sensitivity| (bottom) at 15 μL ($\log_{10}$(μS/m^3)).....85
Figure 58: Percent contribution to G_b vs. displacement. 86
Figure 59: Volume vs. blood conductance for mouse catheter.....87
Figure 60: Mouse model results with surroundings using Wei's equation.....88
Figure 61: Multi-segment catheter subdomains.....90
Figure 62: Cross section of multi-segment catheter mesh 91
Figure 63: Five-segment catheter sensitivity for each individual segment (S/m^3) 93

Figure 64: Sensitivity of single and multi-segment catheter measurements (S/m^3)93
Figure 65: $\log_{10}|$sensitivity$|$ for each individual segment of a five-segment catheter94
Figure 66: $\log_{10}|$sensitivity$|$ for single and multi-segment catheter measurements (S/m^3) 94
Figure 67: Large animal catheter volume vs. conductance using a single segment95
Figure 68: Large animal catheter volume vs. conductance using five segments...95
Figure 69: Single segment (left) and multi-segment (right) segmental volume sensitivity 96
Figure 70: Approximate Heart Geometry 99
Figure 71: Cross section through mesh of the approximate heart geometry 100
Figure 72: Approximate geometry impedivity-sensitivity product, Re{$\mathbf{Z}$} (left) and Im{$\mathbf{Z}$} (right) (Ω/m^3) 101
Figure 73: Approximate geometry $\log_{10}|$impedivity·sensitivity$|$, Re{$\mathbf{Z}$} (left) and Im{$\mathbf{Z}$} (right) (Ω/m^3) 102
Figure 74: G_b·Sensitivity (S/m^3) from parallel model (left), R_b·sensitivity (Ω/m^3) from series model (right) 103
Figure 75: Relative contribution distribution for Re{$\mathbf{Z}$} (left) and R_b (right) ($1/m^3$)104
Figure 76: Relative contributions to Re{$\mathbf{Z}$} and R_b.....104
Figure 77: RV lead motion positions at diastole (left) and systole (right).....107
Figure 78: LV lead position effects 108
Figure 79: RV lead position effects 108
Figure 80: Approximate geometry with atrium 109
Figure 81: Parametric sweep of surrounding tissue conductivity 110
Figure 82: Pleural effusion model.....111
Figure 83: Pleural effusion results 111

Figure 84: Impedivity-sensitivity product with shocking coil [Ω/m^3].....112
Figure 85: Current density with shocking lead [A/m^2].....113
Figure 86: Tetrapolar LCV lead placements.....116
Figure 87: Tetrapolar LCV lead impedivity-sensitivity product [Ω/m^3].....117
Figure 88: Representative MRI slices at diastole and systole.....121
Figure 89: MRI mesh at diastole.....121

Chapter 1: Background and Motivation

Approximately 5.7 million Americans are living with heart failure [1]. The aim of this research is to develop methods to study and monitor heart disease using the admittance method in order to assess left ventricular (LV) volume. Traditional electrical measurements only determine the magnitude of impedance that includes contributions from blood, muscle, and other tissues. The admittance method uses the complex properties of cardiac muscle to separate the blood and muscle signal components in order to target measurements to the LV blood volume. Admittance stands to make the largest impact in the piggybacking of a measurement onto implantable cardioverter-defibrillators (ICDs) to monitor cardiac hemodynamics, enabling ICDs to provide the correct treatment for different types of arrhythmias.

The admittance method was validated as an accurate tool for measurement of LV volume in mice using a conductance catheter [2]; it is currently sold as a commercial research system by Scisense (London, Ontario). Recently, the admittance method was shown to monitor LV dilation in a porcine animal model [3] indicating it could be used as a tool to monitor worsening heart failure.

Although the calibration procedure for the admittance method can been used successfully, there is room for improvement. Admittance measurements in saline result in a significant imaginary component due not to saline permittivity, but to the parasitic properties of the probe; the mechanism behind a probe's contribution to permittivity error is not well understood. Development of a tetrapolar circuit model of admittance measurements may result in new calibration procedures or redesigned probes with improved accuracy or reproducibility.

Recent studies have revealed that one third of patients with ICDs receive an inappropriate shock within three years of implantation [4]. Inappropriate shocks are undesirable as they damage the heart, traumatize the patient, and reduce battery life. The admittance method has the potential to help ICDs determine whether it is most appropriate to observe, apply anti-tachycardia pacing, or to deliver a shock.

1.1 SPECIFIC AIMS

The primary goal of this research is to develop the admittance method so it can one day be piggybacked onto pacemakers and ICDs, and this will be accomplished as follows:

Specific Aim #1

> Develop and validate a circuit model of the tetrapolar measurement including the catheter's contribution to capacitance *in vitro*, and use this model to design or modify surface and catheter probes to reduce the probes' contribution to permittivity error.

Tetrapolar measurements in semiconductor media result in a magnitude-dependent capacitance not due to the permittivity of medium, and there is currently no model explaining this behavior. For surface probe measurements, this capacitance results in permittivity error that must be corrected using a saline calibration. Solutions with known conductivities are used to measure permittivity error across a range of admittance magnitudes. A working model of the tetrapolar measurement will provide knowledge of the critical parameters and allow optimization of probe design. This has the potential to reveal methods to minimize the catheter's contribution and reduce errors through the use of modified probes and a superior calibration technique.

Specific Aim #2

Apply the results of SA #1 to animal models in order to improve the accuracy and reproducibility of admittance measurements *in vivo*.

The catheter contribution to admittance measurements is important in both tissue properties and bulk measurements. Results of SA #1 have the potential to improve each of these measurements. *In vitro* and *in vivo* measurements with standard and redesigned surface probes will show if reduction of parasitic elements is necessary for accurate measurement of conductivity and permittivity.

Specific Aim #3

Investigate experimentally the monitoring of stroke volume using the admittance method *in vivo* with biventricular pacemaker leads.

The next step in developing the admittance method is to carry out studies in an acute animal model using commercially available biventricular pacemaker leads. It is important to develop and validate a method to detect and remove the contribution from muscle. In this way, the measurement will be sensitive to LV blood volume and insensitive to other changes in and around the heart. This will show that an admittance measurement can be piggybacked onto existing pacemaker and ICDs to serve as a monitor of LV stroke volume (SV) to determine whether to observe, shock, or apply anti-tachycardia pacing.

1.2 BACKGROUND AND SIGNIFICANCE

Implantable cardioverter-defibrillators (ICDs) are the preferred treatment for prevention of sudden cardiac death in patients surviving sustained ventricular tachycardia

or fibrillation [5]. ICDs monitor intracardiac electrograms (EGMs) to diagnose arrhythmias and respond through either observation, anti-tachycardia pacing (ATP) or by delivering a shock.

Inappropriate shocks are delivered to one third of patients within three years of implantation [4]. Testing of ICD shocks following implantation has been shown to cause elevated levels of cardiac troponin I [6], indicating myocyte death as the direct result of shocks. Results from the two clinical trials show that inappropriate shocks increase the mortality rate by a factor of two [7, 8]. Further, any shock to a patient results in significant emotional trauma.

Optimization of algorithm thresholds has been shown to reduce the number of shocks without increased morbidity [9]. However, limitations in EGM analysis algorithms remain due to misclassification of atrial fibrillation (AF) or supraventricular tachycardia (SVT), rate errors from oversensing, and mechanical lead problems. Misclassification of arrhythmias is the most common cause of an inappropriate shock while oversensing and lead fracture are less common [10]. Although algorithms have been developed to identify AF and SVT, their use delays or suppresses the application of therapy for ventricular fibrillation (VF) and ventricular tachycardia (VT). Physicians are reluctant to activate these algorithms until cases of AF and SVT are documented. Oversensing occurs when the ratio of the R- to T-wave amplitude decreases, resulting in double counting of each beat. Lead fracture can also result in double counting due to timed movement with the heart.

A new technique is proposed to aid ICD classification of arrhythmias as hemodynamically unstable or stable, through the estimation of instantaneous LV volume and SV on a beat-by-beat basis. The approach is termed the admittance method [2, 3] and determines the admittance between the RV and lateral coronary vein (LCV) leads by

applying a current between the RV tip and LCV tip electrodes and measuring the electric potential between the RV ring and LCV ring electrodes. Although others have used this approach [11], the admittance method uses the complex tissue properties to separate the blood and muscle signal components [2]. At a measurement frequency of 20 kHz, muscle exhibits significant reactance [12] whereas blood's reactance is negligible.

1.2.1 ICD/Pacemaker Prevalence

There are more than 4 million people around the world living with pacemakers or ICDs [13]. The implications of inappropriate shocks and the large number of individuals at risk make the development of new methods to assess cardiac hemodynamics highly desirable.

1.2.2 Competing Technologies for Rhythm Discrimination

There is a significant need for methods to discriminate among different types of arrhythmias due to inappropriate ICD therapy. Currently, several ICD companies include EGM morphology discrimination algorithms, and one uses an impedance measurement.

1.2.2.1 EGM Morphology Discrimination

Morphology algorithms are based on the finding that ventricular EGM morphology is the same during normal sinus rhythm and SVT but changes during VT [14]. Medtronic, St. Jude Medical, and Boston Scientific ICDs currently use morphology algorithms to identify SVT. Morphology algorithms are limited in the identification of rapid SVTs due to rate-related conduction abnormalities, template misalignment, EGM maturation, postshock distortion, and pectoral myopotentials [15]. Despite these limitations, morphology discrimination is currently the most effective algorithm to

discriminate between SVT and VT [16]. Even with the use of these algorithms, inappropriate shocks remain a problem, as shown in multiple clinical trials [8, 9].

1.2.2.2 Cross-Chamber Impedance

Biotronik is currently developing an impedance-based measurement to monitor cardiac hemodynamics [11, 17-20]. The approach is very similar to the proposed technique, but instead of applying a current across the LV, it is applied between two electrodes in the RV and the differential voltage is measured with two electrodes in the lateral vein [17]. Currently, blood and muscle components are not separated in this technique.

1.2.3 Competing Technologies for Heart Failure Detection

Several methods have been proposed to remotely monitor patients by piggybacking systems onto AICDs and pacemakers through the measurement of pressure and thoracic impedance [21, 22]. These techniques have proven successful in detecting impending heart failure, but the systems detect heart failure at a late stage in the progression of the disease, present new risks to the patient or are unable to monitor hemodynamics on a beat-by-beat basis.

1.2.3.1 LV preload as the standard of impending heart failure

The *backward heart failure concept* contends that when the LV fails to discharge its contents, blood accumulates and pressures rise in the atrium and venous system [23]. The inability of the LV to shorten against a load alters the relationship between end-systolic pressure and volume so that LV end-systolic volume rises. The following sequence then occurs: (1) LV end diastolic volume and pressure increase, (2) volume and

pressure rise in the left atrium, (3) the left atrium contacts more vigorously (Starling's Law), (4) the pressure in veins and capillary beds behind the pulmonary LV rise, (5) transudation of fluid from the pulmonary capillary beds into the pulmonary interstitial space increases, (6) elevation of LV, left atrial, and pulmonary venous pressures results in backward transmission of pressures into the pulmonary arterial circuit and leads to pulmonary hypertension, and finally, (7) right heart failure then occurs as a consequence of left heart failure. According to this hypothesis, LV preload will be the most sensitive measure of impending heart failure.

1.2.3.2 Right Ventricle (RV) Pressure

Measurement of RV pressure aims to detect heart failure late in the progression of symptoms. Medtronic's Chronicle monitoring system was rejected by the FDA following a randomized control study which failed to show a reduction in heart failure related events compared to optimal medical management [24].

1.2.3.3 Left Atrial (LA) Pressure

LA pressure measurement detects heart failure at an earlier stage than RV pressure and thoracic impedance, but the measurement puts the patient at increased risk of stroke since the sensor is on the arterial side of the circulatory system. St. Jude Medical is currently performing a clinical trial wherein 2 of 50 patients have had ischemic strokes [22]. While LA pressure is a viable method for detection of heart failure, risk of stroke makes alternative methods more desirable.

1.2.3.4 Thoracic Impedance

Medtronic's Optivol and St. Jude's CorVue heart failure detection systems aim to detect worsening heart failure though a thoracic impedance measurement. These systems detect the heart failure symptom pulmonary edema, which is at a later stage than a pressure increase.

Thoracic impedance is a bulk measurement that includes the heart, ipsilateral lung, and surrounding tissues. The impedance measurement is made at 16 Hz between an RV lead and the pacemaker case [25], where the measurement field includes much of the left thoracic cavity [26]. Optivol's detection algorithm was developed in a retrospective study of 33 patients. Detection occurred at the stage of pulmonary edema and predated the onset of symptoms by 15 days.

1.2.4 The Admittance Method

The admittance method has two main advantages: (1) the ability to separate blood and muscle components of the signal through complex variable analysis and (2) targeted measurement of the LV, where the first symptoms of heart failure appear. The system has initially been tested in an acute open chest porcine model and results show a correlation between blood conductance and LV volume.

1.2.4.1 Complex Admittance Measurement

Admittance is determined by applying a sinusoidal electric current at a frequency of 20 kHz and measuring the resulting voltage. A tetrapolar electrode configuration is used to reduce electrode effects. The measured voltage is dependent on the electric field encompassing blood, muscle, and other tissues. Because muscle has substantial permittivity at the measurement frequency, the voltage signal varies not only in

amplitude but also exhibits a phase shift. Through knowledge of cardiac muscle's electrical properties, conductivity and permittivity, it is possible to separate the blood and muscle components of the signal.

Muscle properties and bulk admittance measurements have been shown to accurately separate blood and muscle components using a conductance catheter in the murine LV [2]. The same principles apply to the proposed system, although a series blood-muscle circuit model is used rather than a parallel model. The circuit model is shown in Figure 1.

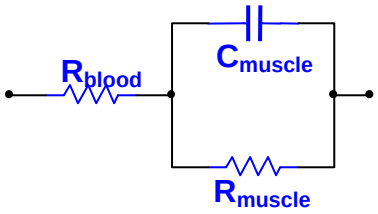

Figure 1: Cross-chamber series circuit model

1.2.4.2 Targeted LV Measurement

It is critical that the electric field be confined to the LV in order for the measurement to have high specificity and accuracy. Targeting the measurement to the LV will be accomplished through the use of commercial biventricular pacemaker leads. These leads are placed in the RV and lateral coronary vein, opposing sides of the LV. This placement is used clinically for patients receiving biventricular pacemakers; thus, piggybacking the admittance measurement will require no additional leads.

Chapter 2: Five-Segment Admittance Catheter Measurements

The conductance catheter allows investigators to assess left ventricular pressure-volume relationships in real time. It is a useful tool in the study of drugs, genes, and optimization of biventricular pacemaker lead placement [27, 28]. The technique was first used in canines in 1981 by Baan *et al* [29] and was extended to mice in the late 1990s.

An improvement, using the complex nature of cardiac muscle to remove parallel conductance and a nonlinear conductance to volume relationship, was recently validated in mice [2]. This allows removal of parallel conductance without the need for hypertonic saline injections. This work shows the extension of the method to large animals for the first time.

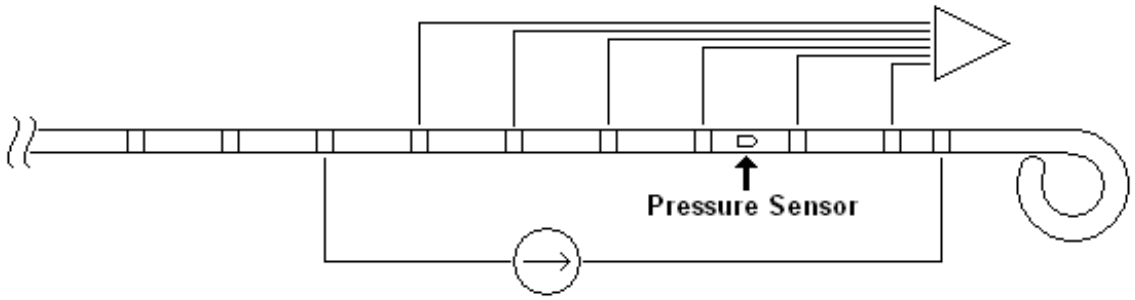

Figure 2: Catheter and circuit interface

Traditional conductance only measures the magnitude of admittance while the admittance method measures both magnitude and phase angle. The additional information from phase angle allows separation of the muscle and blood signals. Conductance and capacitance are defined in terms of the bulk measurement in the following equations,

$$G = \frac{I}{V} = \frac{\iint_S \sigma \boldsymbol{E} \cdot d\boldsymbol{S}}{\int_b^a \boldsymbol{E} \cdot d\boldsymbol{L}} = \sigma F, \tag{1}$$

and

$$C = \frac{Q}{V} = \frac{\iint_S \epsilon \boldsymbol{E} \cdot d\boldsymbol{S}}{\int_b^a \boldsymbol{E} \cdot d\boldsymbol{L}} = \epsilon F, \tag{2}$$

where G is conductance, C is capacitance, I is current, V is voltage, σ is conductivity, E is the electric field, Q is charge, and F is the field form factor or probe constant determined by the geometry. The surface integration in the numerator of both equations is any complete surface between the current carrying electrodes. The line integral in the denominators is any curve connecting the voltage sensing electrodes. Dividing equation (1) by (2) results in the sigma-to-epsilon ratio,

$$\frac{G}{C} = \frac{\sigma}{\epsilon} \tag{3}$$

Blood and muscle domains are modeled as parallel circuit elements. The total admittance measurement is,

$$\boldsymbol{Y} = G_b + G_m + j\omega C_m + j\omega C_{probe}, \tag{4}$$

where G_b is blood conductance, G_m is muscle conductance, ω is the radial frequency, C_m is the muscle capacitance, and C_{probe} is the capacitance from the catheter. These signals are diagramed in the complex plane in Figure 3. Catheter capacitance, C_{probe}, is removed through a calibration procedure performed is saline. This allows the determination of muscle capacitance, C_{muscle}. Through knowledge of the myocardial conductivity and permittivity one can then calculate the muscle conductance, G_{muscle}. The equation for blood conductance is,

$$G_b = Re\{Y\} - \ G_m = Re\{Y\} - \frac{\left[Im\{\boldsymbol{Y}\} - \omega C_{probe}\right]}{\omega}\frac{\sigma_m}{\epsilon_m} \tag{5}$$

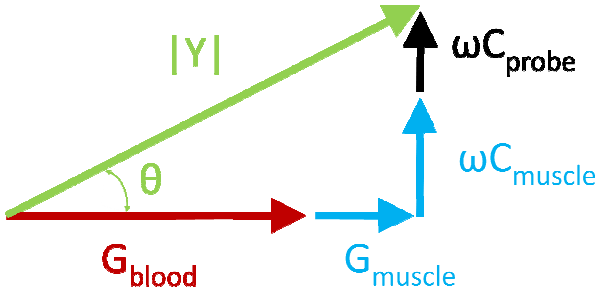

Figure 3: Admittance measurement in complex plane

2.1 INSTRUMENTATION

A five-channel admittance system was designed for these experiments [30]. The system was medically isolated using an isolation transformer and isolation amplifiers. Measurements were made at 20 kHz and the signal processing was performed using an analog magnitude and phase measurement [12].

2.2 EXPERIMENT PROTOCOL

All experiment protocols were approved by the University of Texas Health Science Center at San Antonio's Institution for Animal Care and Use Committee. A Scisense multi-segment conductance catheter with a pressure sensor was placed in the left ventricle via the right carotid artery under fluoroscopy, and segments were selected to span the entire left ventricle. Sonomicrometry crystals (Sonometrics, London, Ontario) were used as the standard of comparison for LV volume.

2.3 PARALLEL CONDUCTANCE REMOVAL

The myocardial contribution to the signal was removed using the admittance method. A sigma-to-epsilon ratio of 900,000 was used for the muscle properties. This

value was not based on measurements, but was used because a larger sigma-to-epsilon ratio produced negative volumes. Hypertonic saline injection was also performed in order to compare results to the traditional conductance method.

2.4 ANALYSIS AND MEASUREMENT RESULTS

Measurements were performed successfully in two pigs. Sonomicrometry crystals (Sonometrics, London, Ontario, Canada) were used as a comparison for volume. Data were analyzed using several techniques,

1) Traditional conductance method using Baan's equation calibrated with stroke volume [29],

$$Volume = \frac{1}{\alpha}\rho L^2 \left(G - G_p\right) \tag{6}$$

2) Admittance method with Wei's equation [31],

$$Volume = \frac{\gamma}{\gamma - G_b}\rho L^2 G_b \tag{7}$$

3) Single segment admittance method with Wei's equation.

While the traditional technique uses five segments, there is interest in simplifying the technique by using only a single segment. Results of the three analysis methods are shown in the pressure-volume loops in Figure 4. Both the traditional conductance technique and the admittance method produce results that correlate well with sonomicrometry crystals. The single segment method tends to underestimate volume.

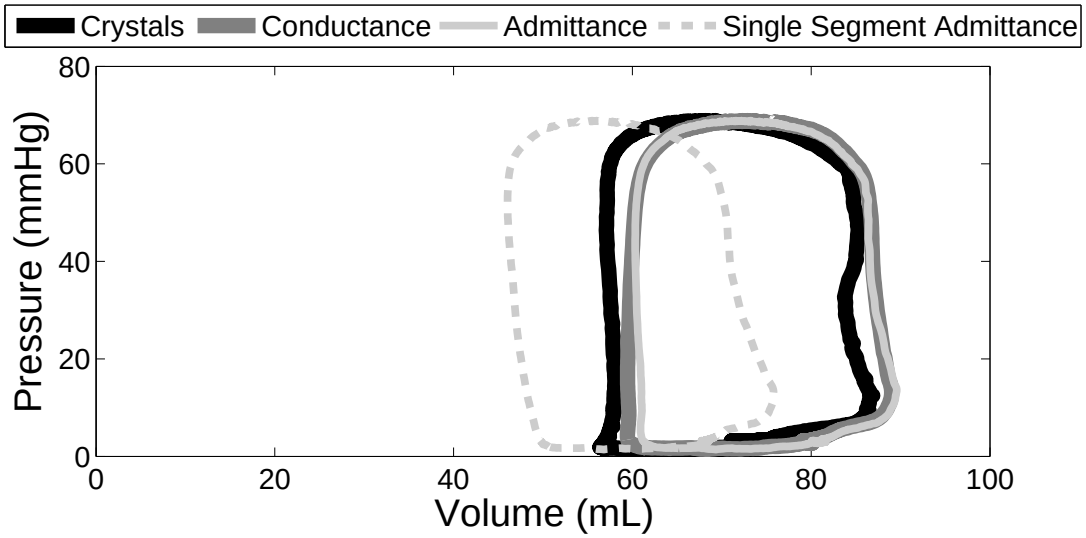

Figure 4: Large animal pressure-volume loops

Time-varying blood and muscle conductance are shown in Figure 5. A constant value for parallel conductance was measured using the hypertonic saline method (dashed line).

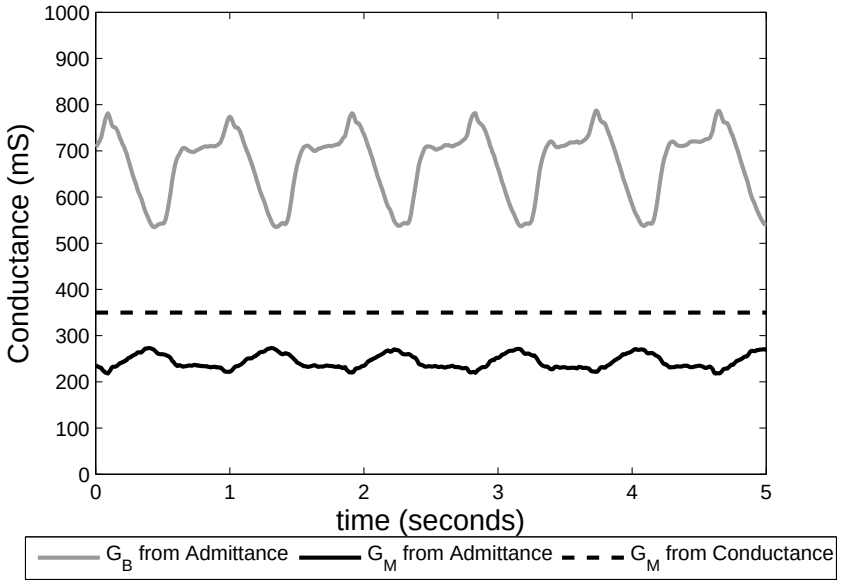

Figure 5: Time-varying blood and muscle conductance

2.5 DISCUSSION

These results demonstrate that the admittance method can be applied to large animal studies and that G_m varies over the cardiac cycle. This removes the need for injection of hypertonic saline to remove parallel conductance. More studies are necessary to determine which method is more accurate and reliable.

Chapter 3: Complex Muscle Property Measurements

Accurate measurements of electrical conductivity and permittivity are central to the admittance method. Non-ideal probe characteristics limit the accuracy of *in vivo* measurements. This chapter examines variations in muscle properties in infarct mice, the underlying mechanisms for errors in conductivity and permittivity measurements, and explores methods to increase the accuracy of surface property measurements.

3.1 MURINE INFARCT MUSCLE PROPERTIES

Volume measurements are often applied to disease models where muscle properties are likely to change. One such disease model is infarcted myocardium. In this model a coronary artery is ligated to reduce perfusion to an area of the heart. This results in muscle cell death and scarring in the infracted zone and the rest of the heart becomes hypertrophic. Not only are there different myocardial properties, but the properties vary throughout the left ventricle. This study was performed to quantify the myocardial properties in infracted and hypertrophic muscle in order to determine the effect on the admittance method as applied to murine infarct models.

3.1.1 Probe Design

Left ventricular wall thickness in the infarct zone varies from 0.5 mm to 0.8 mm [32] in C57 mice aged 6 to 8 months. Standard muscle property probes for mice are designed to have a penetration depth of 0.6 mm [12], and therefore cannot be applied to infracted muscle without inducing measurement error. A new probe was designed to have

a shallower penetration depth to be used for infarcted myocardium property measurements.

COMSOL Multiphysics, a finite-element software package, was used to determine the electrode spacing necessary to obtain a penetration depth of 0.39 mm. The model was based on one designed by Kottam [33], and uses a 2D quasistatic electric model. Simulations were performed with varying distance between the probe and an insulating medium, mimicking penetration depth measurements made in saline. Electrode spacing was decreased iteratively until the desired penetration depth was achieved. The resulting spacing for the desired penetration depth was 0.25 mm between each electrode made of 36 awg platinum wire. Scisense manufactured a probe to these specifications that was used for all of the measurements.

3.1.1.1 In Vitro Penetration Depth Measurement

The penetration depth was experimentally determined in saline [12, 33]. A micromanipulator was used to place the probe against an insulating surface. This probe was then moved away from the insulator in increments of 0.05 mm. Measurements were made until the admittance measurement reached a constant value. Defining the penetration depth to be where the admittance magnitude was 90% the maximum value, the measured penetration depth was 0.375 mm. This value is just less than the simulated value, 0.39 mm.

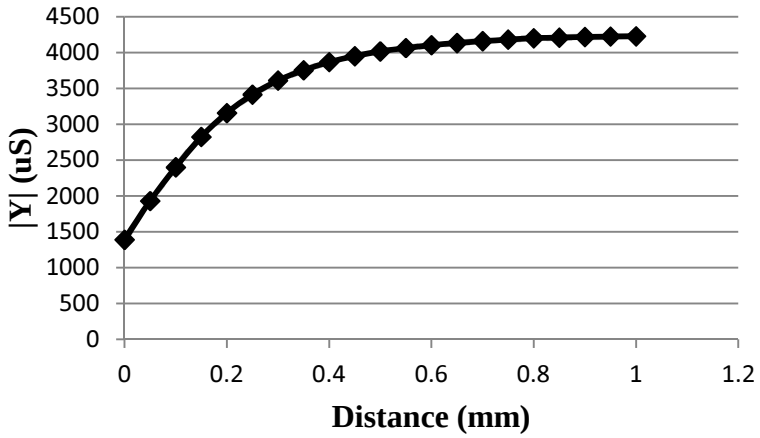

Figure 6: Infarct probe penetration depth

3.1.2 Experiment Protocol

All experiment protocols were approved by the University of Texas Health Science Center's Institute for Animal Care and Use Committee. Mice (n=5) were anesthetized using isoflurane. Measurements were determined at frequencies of 1000, 1953, 5000, 10000, 19195, 31250 and 50000 Hz using the RamsES instrument [33] in swept frequency mode. Saline calibrations were performed before each experiment. Measurements were performed in the infarct and hypertrophic zones.

3.1.3 Infarct Model Measurement Results

Measurements of conductivity and permittivity in the infarct and hypertrophic zones were performed in five mice and are shown in Figure 7. Infarcted muscle exhibits higher conductivity and lower permittivity than hypertrophic muscle. The infarct zone exhibits a higher sigma-to-epsilon ratio at all frequencies, shown in Figure 8.

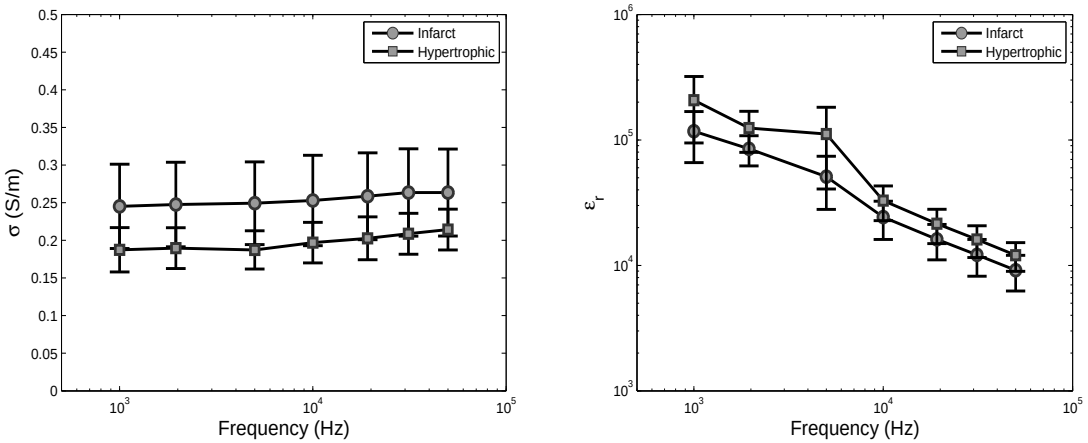

Figure 7: Infarct mice muscle properties

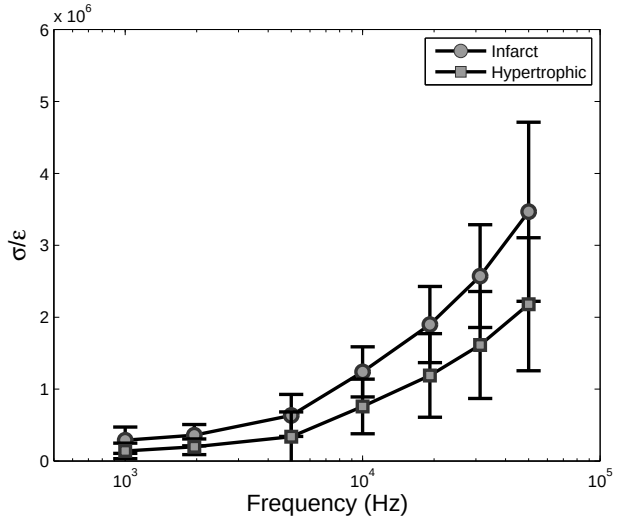

Figure 8: Infarct mice sigma to epsilon ratio

A two-sided, paired t-test was performed at each frequency. Most measurements were shown to be statistically different, $p < 0.05$. Results of the statistical analysis are shown in Table 1.

	Frequency (Hz)						
	1 kHz	2 kHz	5 kHz	10 kHz	20 kHz	30 kHz	50 kHz
σ (S/m)	0.0295	0.0273	0.0239	0.0332	0.0271	0.0300	0.0394
ε_r	0.0557*	0.0521*	0.0489	0.0177	0.0169	0.0220	0.0299
σ/ε (S/F)	0.0593*	0.0564*	0.0780*	0.0204	0.0111	0.0142	0.0352

Table 1: P-values for infarct vs. hypertrophic zone paired t-test

3.1.4 Discussion

These results mimic the expected changes in the tissue properties in an infarct model. Myocyte death occurs in the infarcted region, reducing the permittivity. Myocytes are replaced with fibrous tissue, which has higher conductivity and lower permittivity. Both myocyte death and fibrous tissue cause the sigma-to-epsilon ratio to increase. Hypertrophic zone measurements are comparable to those presented in the recent publication on banded mice, 1.06 ± 0.58 M S/F at 20 kHz [2].

These results show that the infarcted region has a sigma to epsilon ratio of two to three times that of the hypertrophic zone. It is therefore not possible to apply the admittance method to remove parallel conductance without introducing error. The degree of error will depend on the size of the infarct and would have to be quantified experimentally.

3.2 TETRAPOLAR MEASUREMENT CIRCUIT MODEL

The effects of wire capacitance and electrode impedance are readily observed by placing a tetrapolar probe in saline. Large probes produce limited effects but small probes necessary to perform *in vivo* measurements are affected by non-ideal circuit properties.

* Indicates difference is not statistically significant

At frequencies below 100 kHz the relative permittivity of water is 80. There should be no measurable permittivity in saline; however, the appearance of permittivity is observed in tetrapolar systems where the wire capacitance and electrode impedance are significant. This permittivity is an error in the measurement. It is dependent on the conductivity of the saline as well as the field shape. This error is an order of magnitude larger than the contribution from the capacitance between two wires, owing to interaction between associated poles.

The circuit model in Figure 9 was used to explore the apparent dependence of the permittivity measurement on saline conductivity. Although a similar model was analyzed by Kottam [34], the effects on permittivity were not closely examined.

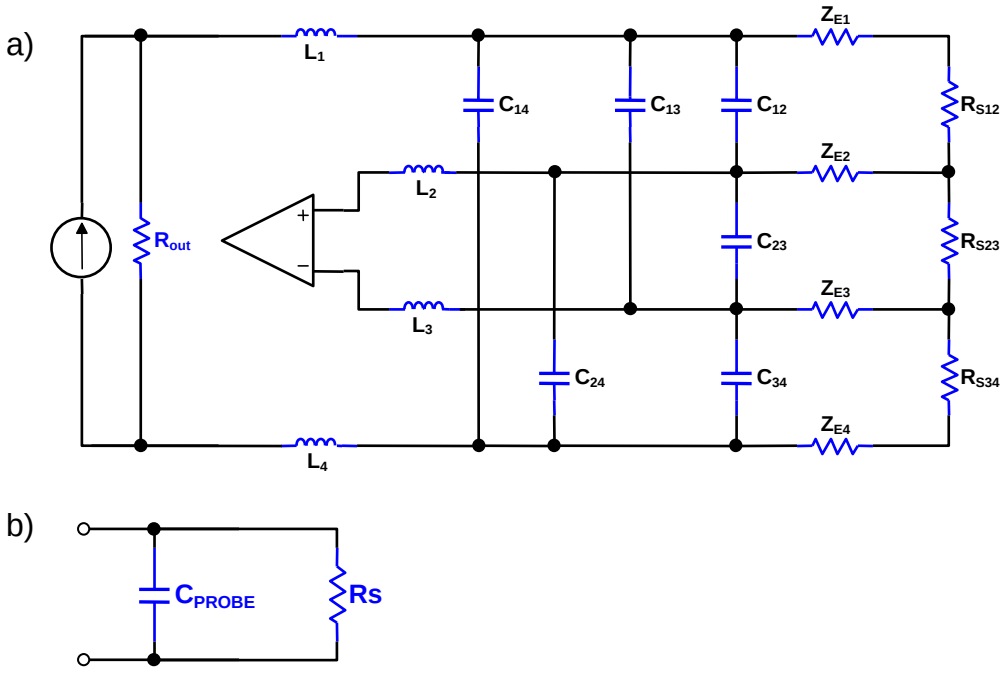

Figure 9: a) Complete and b) effective circuit models

A nodal admittance matrix was constructed and solved using MATLAB. The current source's output impedance was set to R_{out} = 1 MΩ. The instrumentation

amplifier's differential input impedance was set to Z_{IN} = 1 TΩ || 2 pF. Analysis was performed by calculating the measured impedance over frequency, and through a parametric study that varied saline conductivity, wire capacitance, and electrode impedance. Electrode impedances are modeled as constant phase elements [35] with the electrode impedance given by,

$$Z_E = \mathrm{R}_\Omega + \frac{Q}{(j\omega)^{(1-\alpha)}} \tag{8}$$

Parameter values of $R_\Omega = 152\ \Omega$, $\alpha = 0.25$ and $Q = 1.52 \times 10^6\ \Omega$ are used from measurements on Scisense rat surface probes with platinum electrodes [34]. At 20 kHz, this is equivalent to circuit model in Figure 10.

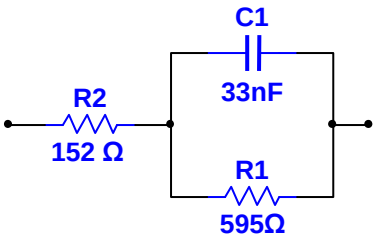

Figure 10: Electrode circuit model at 20 kHz

The probe constant, F, is used to relate the measured conductance to conductivity. It is determined by the geometry of the probe. In this model the baseline probe constant is set to 0.003 m, but remains affected by frequency dependent elements. The resulting real and imaginary parts of admittance are,

$$Re\{\boldsymbol{Y}\} = \sigma F \tag{9}$$

and

$$Im\{\boldsymbol{Y}\} = \omega\epsilon_r\epsilon_0 F + \omega C_{probe}. \tag{10}$$

Additional terms in the real part of admittance are neglected but become significant at frequencies greater than 100 kHz. The second term in the imaginary component of admittance represents error due to the non-ideal characteristics of the

tetrapolar measurement. The error in the imaginary component of admittance creates an error in permittivity,

$$\epsilon_r \text{ error} = \frac{C_{probe}}{\epsilon_0 F}. \tag{11}$$

The frequency sweep in Figure 11 shows the movement of zeros. Two poles are located around 100 kHz, and their frequency depends on saline conductivity, electrode impedance, and wire capacitance. At 20 kHz, the magnitude response does not appear to be affected by the poles, but significant varations to the phase response are present.

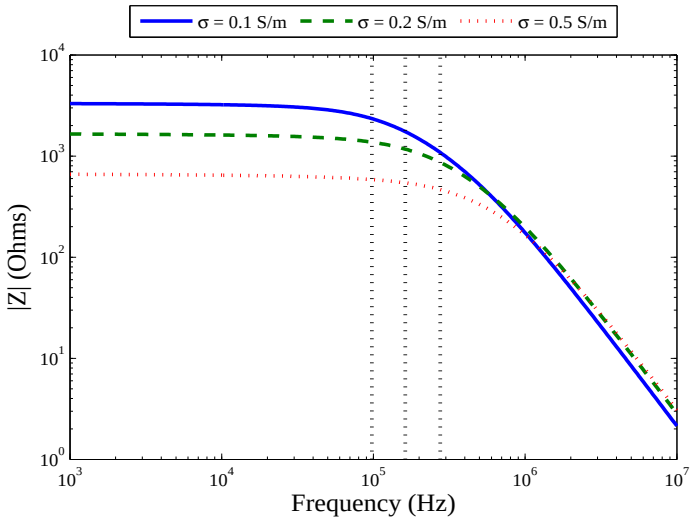

Figure 11: Impedance magnitude *vs.* frequency. Z_E = 152 + (33 pF || 595) Ω and C_p = 50 pF

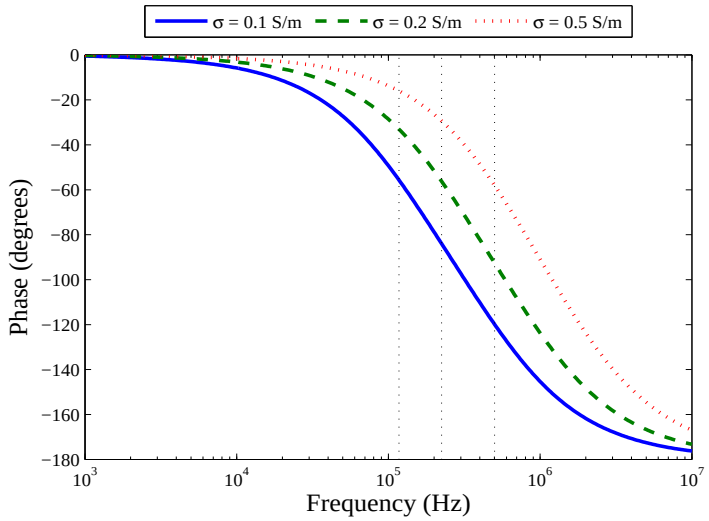

Figure 12: Impedance phase *vs.* frequency. Z_E = 152 + (33 pF || 595) Ω and C_p = 50 pF

Sweeping the solution conductivity gives results similar to those observed experimentally. A slight decrease in the probe constant is observed as conductivity is reduced. With increasing conductivity there is increasing permittivity error. The measured permittivity error is linear with conductivity.

Figure 13 shows the probe constant and relative permittivity error over a range of conductivities for several values of electrode impedance with wire capacitances of 50 pF. As the electrode impedance is reduced, variation in the probe constant reduces as well as the permittivity error. Further reduction of the electrode impedance results in a nonzero but constant apparent permittivity. The value is an order of magnitude larger than the contribution a single 50 pF C_{23} capacitor would alone contribute.

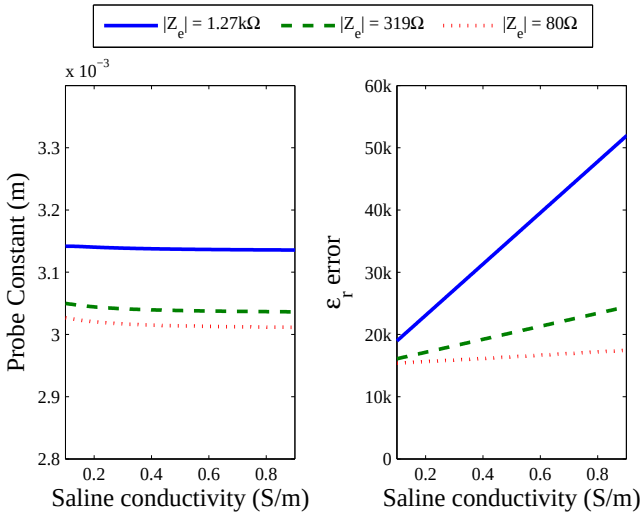

Figure 13: Tetrapolar model sensitivity to electrode impedance

The analysis for several values of wire capacitance is shown in Figure 14, with the electrode impedance held constant at the measured value shown in Figure 10. Similar effects are observed to those of varying the electrode impedance.

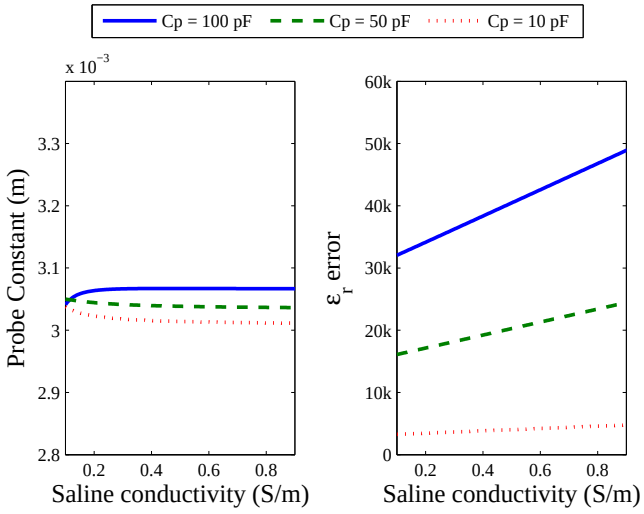

Figure 14: Tetrapolar model sensitivity to wire capacitance

The effects of wire inductance were also studied, with the results shown in Figure 15. Interwire capacitance was set to 50 pF. The first inductor value was set to match the value obtained by measurements on similar probes [34]. The tetrapolar measurement is insensitive to reasonable wire inductances, as a value of 30 mH is required before any changes to the probe constant or permittivity errors are observed. A value of 30 μH is three orders of magnitude above a physically realistic wire inductance, 30 nH.

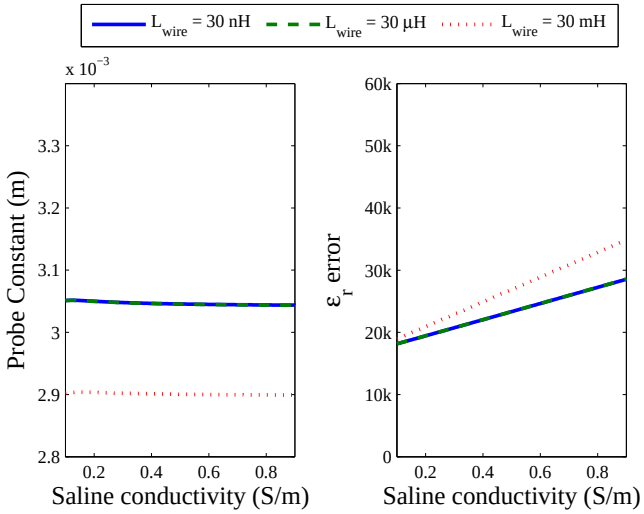

Figure 15: Tetrapolar model sensitivity to wire inductance

3.2.1 Experimental Modification of Interwire Capacitance

Experimental reduction of the probe parasitic capacitance effects may be accomplished by simply shortening the cable length between the electrodes and the amplifier. Measurements of a surface probe with variable cable length resulting in interwire capacitances of 160 pF and 55 pF are shown in Figure 16. A 100 pF decrease in capacitance clearly reduces the permittivity error across a range of solution conductivities.

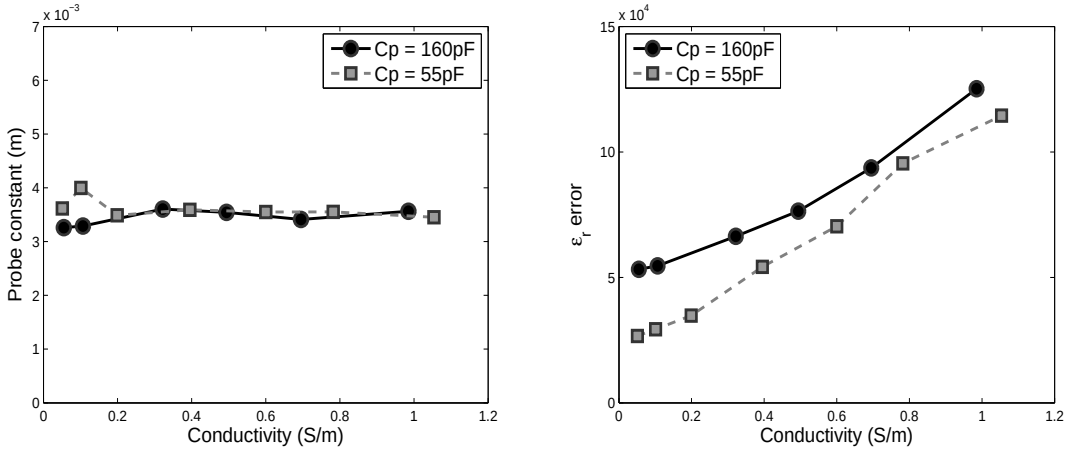

Figure 16: Scisense surface probe with Cp = 160 pF and 55 pF

3.2.2 Experimental Modification of Electrode Impedance

In order to assess the sensitivity of the tetrapolar admittance measurement to electrode impedance experimentally, saline calibrations were performed before and after modifications to the electrode impedance using electrolytic etching and platinization. These methods increase the surface area of electrodes in order to decrease their impedance.

Results are shown in Figure 17. Permittivity error decreases by approximately 8 to 10 percent in response to etching, and platinization reduces the probe capacitance even more. These results confirm that electrode impedance is an important factor in the determination of permittivity error. Further reduction in permittivity error may be accomplished through refinement of the technique. Electrode impedance can be minimized through optimization of plating time for example.

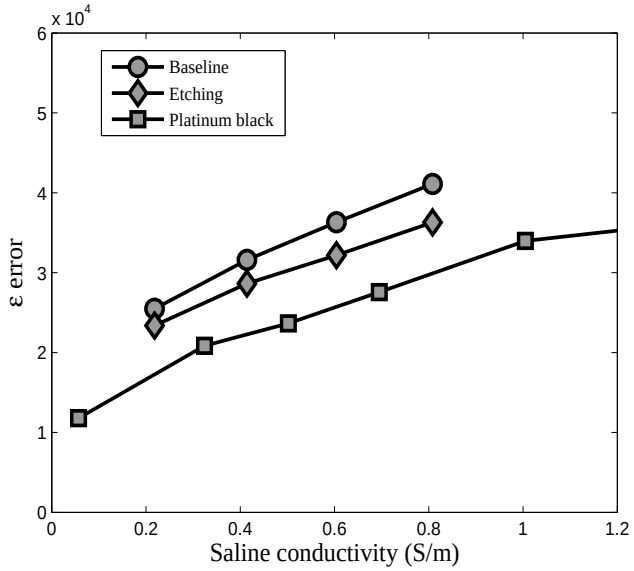

Figure 17: Measured and modeled probe capacitance *vs.* conductivity

3.2.3 Discussion

Experimental results show the dependence of property measurements on interwire capacitance and electrode impedance. Experimental and simulated results show the same relationships among the probe constant, permittivity error, wire capacitance, and electrode impedance. Fluctuations in electrode impedance may prevent direct application of the circuit model to correct errors. These results provide a better understanding of the underlying error mechanisms in the use of the tetrapolar configuration for property measurements. Improvement in the accuracy of property measurements is most likely to be achieved through significant reduction in interwire capacitance.

3.3 ACTIVE SURFACE PROBES

New surface probes were designed and constructed to minimize the effects of interwire capacitance. This method was chosen because the circuit model shows reduced

interwire capacitance gives a significant reduction in permittivity error and it is the most feasible improvement in the technique.

3.3.1 Instrument Design

Two buffer amplifiers and a current source were placed on a small printed circuit board with the electrodes connected at the edge of the board. An Improved Howland current pump [36] was used for the current source. A simple feedback current source was not used as it proved to be greatly dependent on parasitic capacitance. The current source schematic is shown in Figure 18. The trace length between the amplifiers and the electrodes is less than 1 cm.

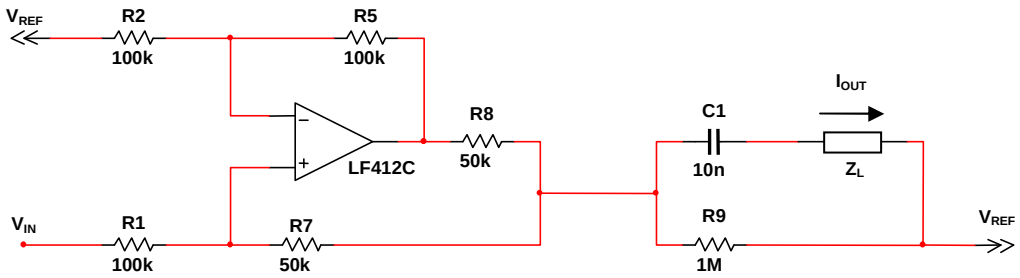

Figure 18: Active surface probe current source

Components C1 and R9 form a DC current blocking circuit with a cutoff frequency of 15 Hz; this is far enough away from 20 kHz such that it does not induce phase in measurement. The applied current is set according to the following equation [36],

$$I_{OUT} = \frac{V_{IN}}{R_1 + R_7}\left(1 + \frac{2R_2}{R_8}\right). \quad (12)$$

The surface probe is connected to a modified version of the instrument used in section 4. This circuit provides a sine wave that is used to apply the measurement current. A picture of the assembled circuit is shown in Figure 19.

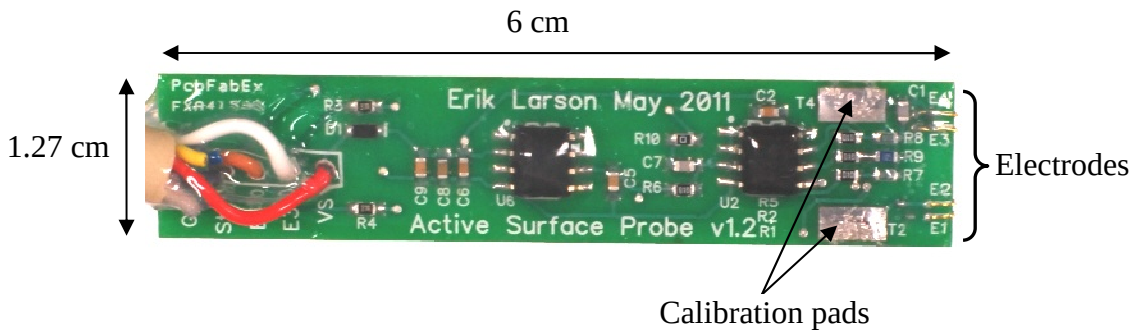

Figure 19: Active Surface Probe

Exposed pads are located near the electrodes and are used to calibrate the instrument with known test loads. Two more pads are located on the back of the board. Alligator clips can be used connect each pair of pads, which shorts together a current and voltage pair for calibration. The board is coated in silicone to protect the circuit during measurements.

3.3.2 Active Surface Probe Calibration

Following construction of the active surface probe, a saline calibration was performed. A similar passive probe was also calibrated for comparison. The resulting saline calibration for each probe is shown in Figure 20. Although the active surface probe reduced permittivity error in the range of cardiac muscle conductivity, the slope of the permittivity error increased. This may be due to differences in the electrodes, as model results show the permittivity error's slope increases with electrode impedance. Gold-wire electrodes were used for both probes.

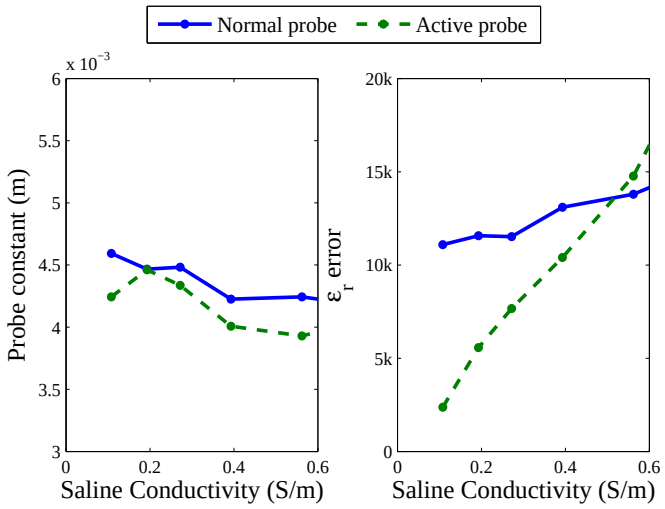

Figure 20: Saline calibration for passive and active probes

3.3.3 *In Vitro* Measurements

A phantom material provides a means to assess the accuracy of permittivity measurements *in vitro*. While saline is excellent for probe calibration, it has negligible permittivity in the frequency range of interest as ϵ_r = 80 at 20 kHz. A phantom material was constructed as described by Kao *et al* [37] to have properties similar to cardiac muscle, σ = 0.16 S/m and ϵ_r = 11,800 at 20 kHz [12].

The phantom is a mixture of agar, saline, and graphite. The conductivity and permittivity of the phantom mixture are shown in Figure 21. Measurement of the phantom properties was accomplished using a test cell with large area electrodes, minimizing the effects of electrode impedance. Accuracy and reproducibility of permittivity measurements can now be assessed using this phantom with properties measured using the test cell as a standard of comparison.

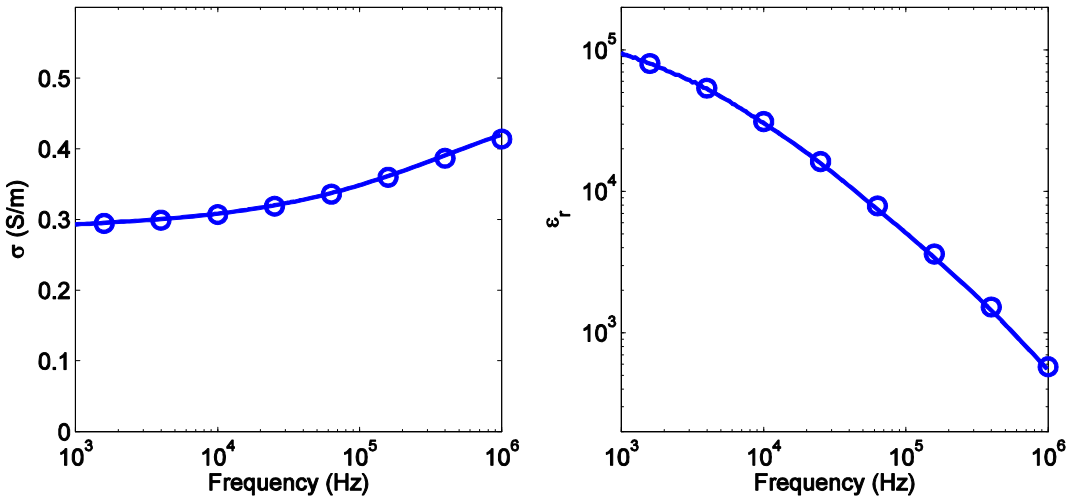

Figure 21: Phantom conductivity and relative permittivity vs. frequency

Three phantoms were produced to measure conductivity and permittivity over the range of expected values. The formula for each phantom is shown in Table 2. Phantoms were made according to [37]: Water and salt were first combined and heated to 85°C. Agar and graphite were then added and stirred using a magnetic stirrer. Heat was removed once the mixture returned to 85°C. The mixture was stirred as it cooled and was then poured into the test cell when it reached 40°C. Manual stirring continued until the phantom thickened.

	Phantom		
	1	2	3
Distilled Water (ml)	100	100	100
Salt (g)	0.1	0.2	0.3
Agar (g)	1.4	1.4	1.4
Graphite (g)	5	10	15
σ (S/m)	0.25	0.40	0.59
ε_r (F/m)	15,000	37,000	71,000

Table 2: Phantom formula

Measurements were made 24 hours after making the phantom to ensure the temperature of the phantom was uniform at 25°C. Measurements were made at the center

of the phantom to reduce the effects of evaporation most likely to occur at the surface. In between measurements, the phantom was placed in a sealed container with minimal air volume to minimize evaporation. Surface probes were cleaned between each set of measurements.

3.3.4 Test Cell

Analysis was performed using linearity plots and further analyzed using Bland-Altman plots because the true electrical properties are unknown. A tetrapolar test cell was used as the standard of comparison, shown in Figure 22. The dimensions of the test cell were based on dimensions of a similar probe used by Kao [37], but tetrapolar electrode configuration was used rather than a bipolar configuration. The length, width, and height of the test cell are 10 cm, 3 cm and 2 cm respectively. Stainless steel needle electrodes were centered in the test cell at a spacing of 6 cm. Copper plate electrodes sit at the far ends of the test cell and were silver plated using silver plating powder (Cool-Amp, Lake Oswego, Oregon). The large dimensions of the test cell reduce error due to increased electrode surface area and increased sample volume size in comparison to standard surface probes.

Measurements were performed by connecting the two plate electrodes to a current source, and the needle electrodes to a wideband instrumentation amplifier, AD8253ARMZ (Analog Devices). An improved Howland current pump and a current to voltage amplifier were used to apply and measure the current. Both voltage and current measurements are digitized using a high speed LabVIEW data acquisition card at 4 MHz with simultaneous sampling.

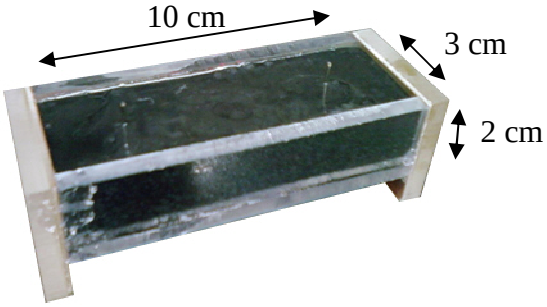

Figure 22: Test cell with phantom

The mean bias of the two probes in the measurement of electric properties is shown in Table 3. Measurement results are shown in Figure 23 and Figure 24. Each group from left to right represents measurements from phantoms 1, 2 and 3 respectively. These results show that the accuracy of the active and normal surface probes is comparable under controlled conditions.

	Active Surface Probe			Normal Surface Probe		
	σ (S/m)	ε_r (F/m)	σ/ε (S/F)	σ (S/m)	ε_r (F/m)	σ/ε (S/F)
Mean difference	0.0556	5,422	82,430	0.0414	3,510	74,720
Std. dev. of difference	0.0218	4,620	240,900	0.0184	4,607	149,460

Table 3: Mean difference and standard deviation of phantom properties

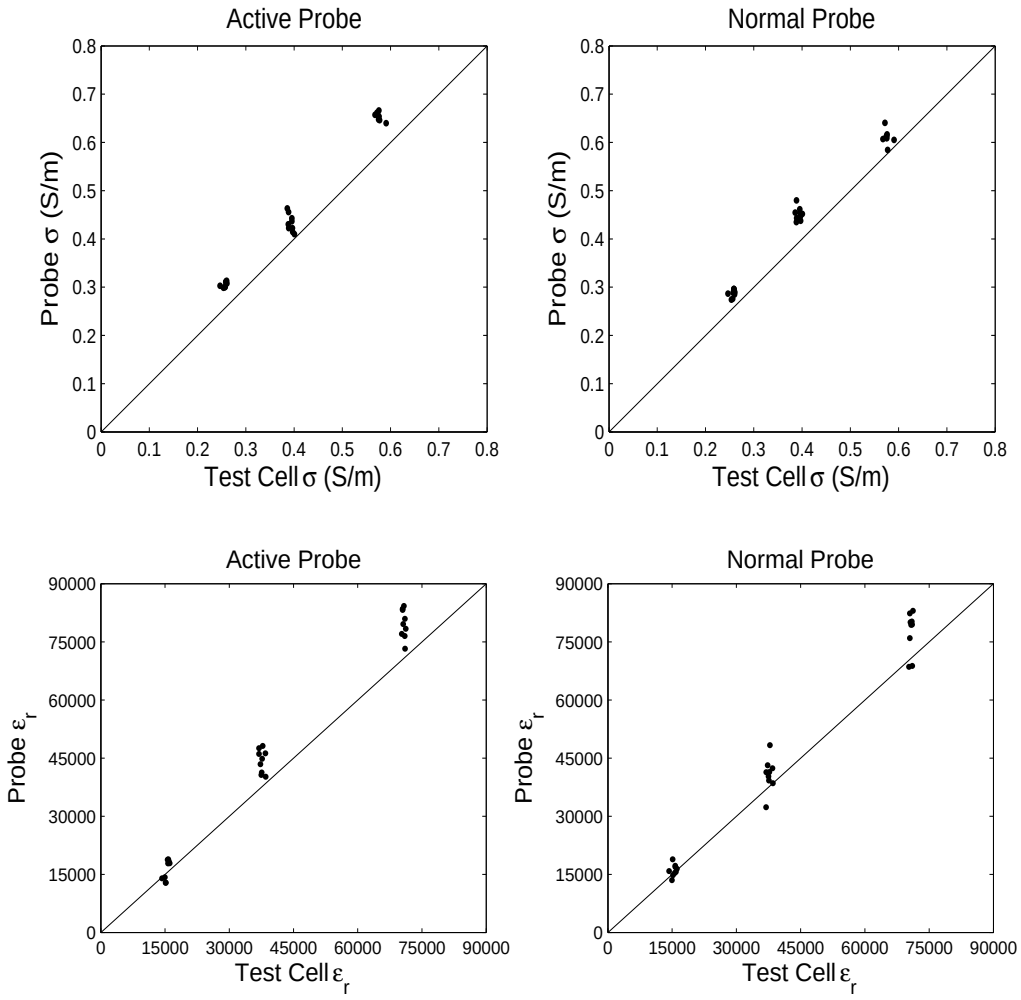

Figure 23: Conductivity and permittivity linearity plots

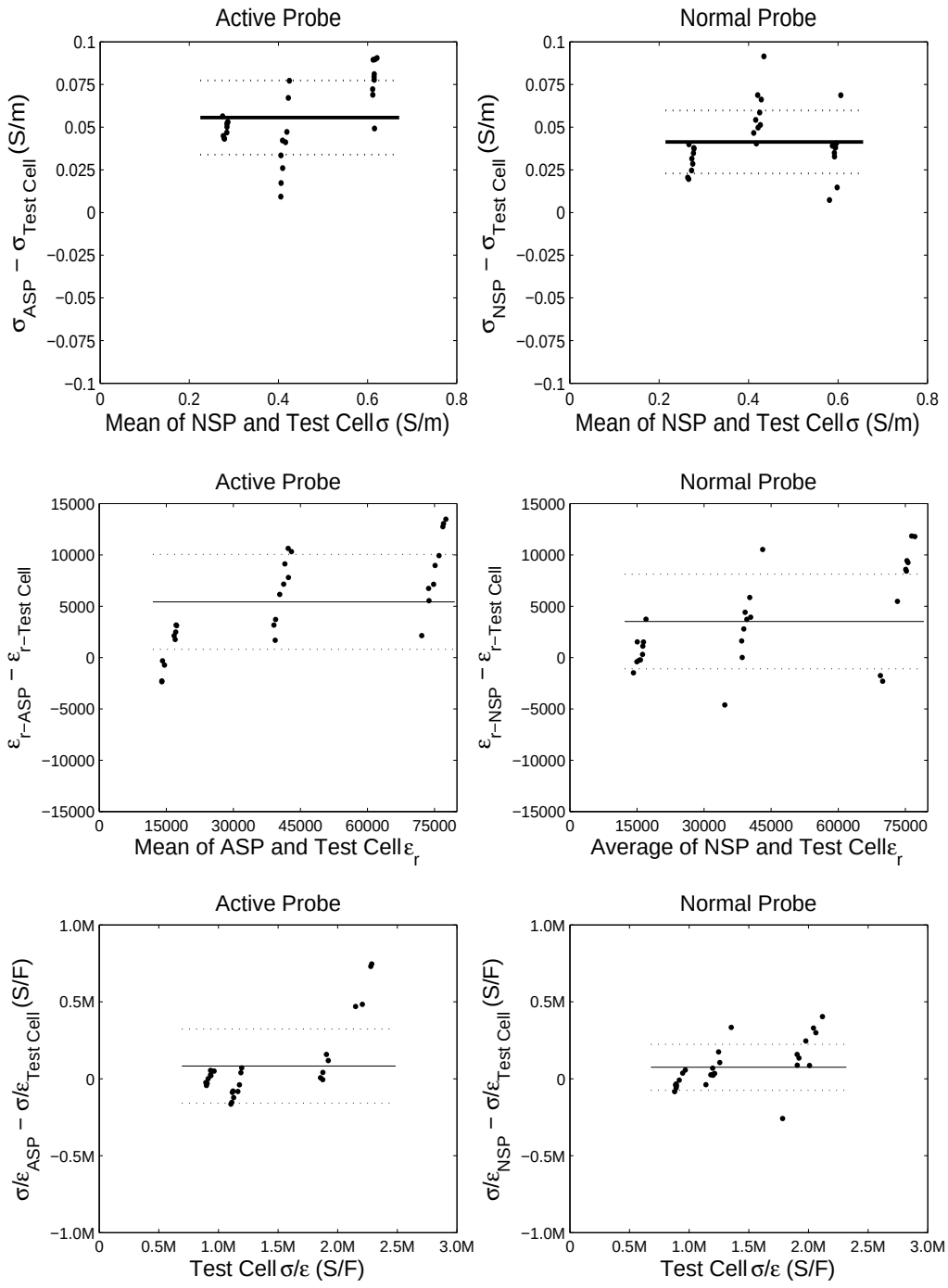

Figure 24: Bland-Altman plots of phantom property measurements

3.3.5 Field Form Factor Effects

A saline calibration measures the probe capacitance with a nearly constant field shape. To examine the effects of the field shape on the measured probe capacitance, a Petri dish with varying levels of 0.4 S/m saline was used, similar to a penetration depth measurement. Measurements for the active and normal surface probes are shown in Figure 25.

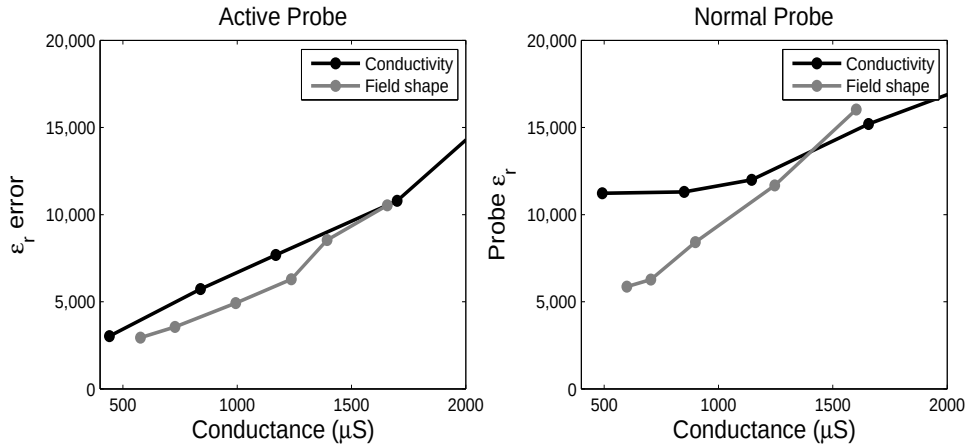

Figure 25: Probe permittivity error changed with field form factor and solution conductivity

These results show that the permittivity error is affected by field shape, especially the normal probe at conductance values less than about 1250 μS. If the field shape is changed during a measurement due to anisotropy, the measured permittivity would be underestimated since the saline calibration would overcorrect for permittivity. This effect was not seen the phantom measurements, as the field shape was constant.

3.3.6 Canine Myocardium Measurements

Epicardial surface properties were measured in canine (n = 5) subjects with normal and active surface probes. These measurements were performed as part of the experiments in Chapter 4.

Measurements were made on the anterior surface of the LV, which was wiped clean prior to each set of measurements. Probes were placed at end expiration to minimize motion artifact. The results of the five experiments are shown in Figure 26 and Figure 27.

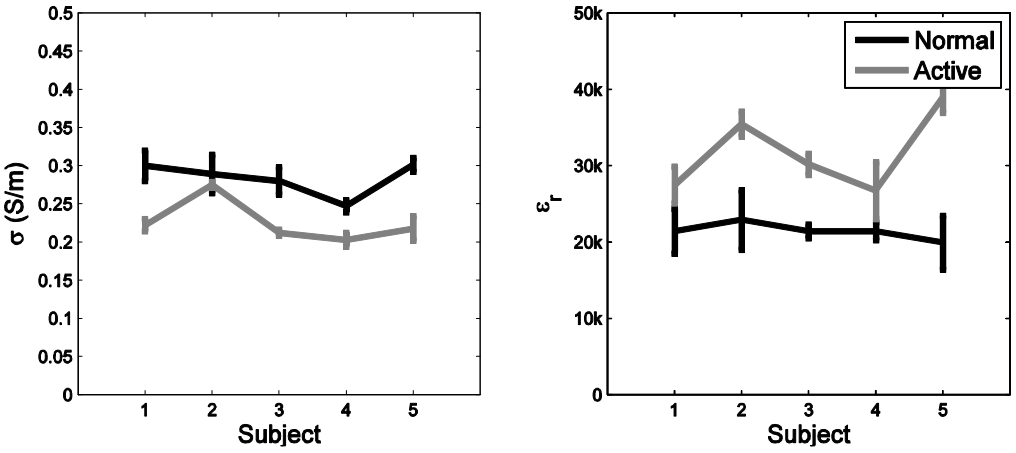

Figure 26: Canine conductivity and permittivity measurements

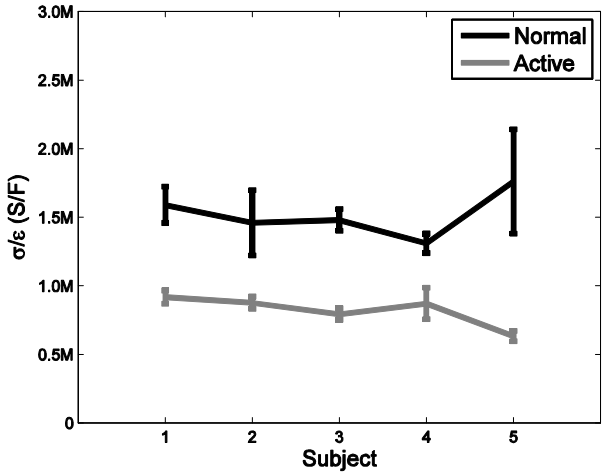

Figure 27: Canine conductivity to permittivity ratio measurements

Probe	Conductivity (S/m)	Relative Permittivity
Normal Surface Probe	0.283 ± 0.022	21,400 ± 1061
Active Surface Probe	0.226 ± 0.028	31,744 ± 5276

Table 4: Canine myocardial property measurements

A two sided paired t-test was performed at a confidence level of $\alpha = 0.05$. This analysis showed that $\sigma_{Normal} \neq \sigma_{Active}$ ($p = 0.011$), $\varepsilon_{Normal} \neq \varepsilon_{Active}$ ($p < 0.015$), and $\frac{\sigma}{\epsilon}_{Normal} \neq \frac{\sigma}{\epsilon}_{Active}$ ($p < 0.01$).

3.4 DISCUSSION

New analysis of the tetrapolar circuit model characterizes the origin of medium dependent probe capacitance for the first time. Results show that interwire capacitance and electrode impedance are significant factors that affect probe permittivity error. While calibrations can be performed using a measured relation between admittance magnitude and probe capacitance, permittivity error changes with electrode impedance. Since permittivity error can be on the same order as the permittivity of the medium under

measurement, this greatly limits the accuracy of surface probe measurements. Thus, interwire capacitance should be reduced as much as possible to increase measurement accuracy; electrode impedance should also be minimized if possible.

The active probe was expected to have higher accuracy than the standard probe, but *in vitro* phantom studies show they have comparable accuracy. This active probe design did not reduce the permittivity error by a large factor, which may be the reason that no significant increase in accuracy was observed. However, the active surface probe was seen to be less susceptible to field shape effects than the standard probe.

In vivo measurements with the active surface probe show that the sigma-to-epsilon ratio may be lower than previous measurements have suggested, due to underestimation of muscle permittivity. One possible reason for the lower permittivity measured with the normal probe is its susceptibility to field shape effects. If the effects of anisotropy are similar to restricting the field shape, the result may be overcorrecting for probe capacitance resulting in underestimated permittivity.

The measured sigma-to-epsilon ratio was halved to maintain positive blood conductance values in epicardial porcine experiments [3]. This scaling was justified because the measurement was across the ventricle, so the current travels in the transverse direction relative to muscle fibers. Surface probe measurements are made in the longitudinal direction, in the same plane as muscle fibers. Transverse conductivity has been shown to be a factor of two less than longitudinal conductivity [38]. Therefore, the sigma-to-epsilon ratio was scaled accordingly.

Conductance catheter measurements include a muscle component that is largely longitudinal, and in Chapter 1 it was also necessary to use a lower sigma-to-epsilon ratio to produce reasonable results. Accurate volumes were obtained using a sigma-to-epsilon

ratio of 900,000 S/F. A larger sigma-to-epsilon ratio resulted in negative volumes using Wei's equation.

Unless a uniform field can be established, any measurement will be a mixture of longitudinal and transverse properties, including surface probes. New measurements with active surface probes suggest that the true sigma-to-epsilon ratio may not need to be scaled for use in cross-chamber admittance models.

Chapter 4: Cardiac Hemodynamic Monitoring with Biventricular Pacing Leads

The admittance method has previously been used with conductance catheters and epicardial electrodes to assess left ventricle (LV) volume [2, 3]. Due to the large number of ICD patients that receive inappropriate shocks, the admittance method stands to make the largest clinical impact by piggy-backing the measurement on ICDs as an additional method to determine whether to only observe, apply anti-tachycardia pacing or deliver a shock. This study assesses the feasibility of using the admittance method with clinical pacing leads to track acute changes in stroke volume varied with pacing and dopamine infusion.

4.1 Simplified Series Model Derivation

The real and imaginary parts of impedance are separated using the admittance method as described previously [3]. The derivation of the equation to separate blood and muscle components has been simplified using an impedance formulation. The circuit diagram of the series blood and muscle model is shown in Figure 28.

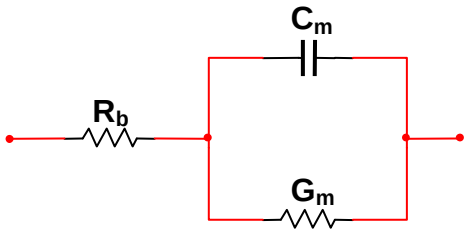

Figure 28: Series blood and muscle circuit model

The impedance across this model is,

$$Z = R_b + \frac{1}{G_m + j\omega C_m} = R_b + \frac{1}{G_m + j\omega C_m}\frac{G_m - j\omega C_m}{G_m - j\omega C_m} \tag{13}$$

The equation can be simplified by defining the constant κ.

$$\kappa = \frac{1}{(G_m + j\omega C_m)(G_m - j\omega C_m)} = \frac{1}{G_m^2 + \omega^2 C_m^2} \tag{14}$$

$$Z = R_b + \kappa G_m - j\omega\kappa C_m \tag{15}$$

$$Re\{Z\} = R_b + \kappa G_m \tag{16}$$

$$Im\{Z\} = -\omega\kappa C_m \tag{17}$$

$$C_m = -\frac{Im\{Z\}}{\kappa\omega} \tag{18}$$

The conductance capacitance relationship is,

$$\frac{G_m}{C_m} = \frac{\sigma_m}{\epsilon_m} \tag{19}$$

Substituting equation (18) into (19) and rearranging,

$$\kappa G_m = -\frac{Im\{Z\}}{\omega}\frac{\sigma}{\epsilon} \tag{20}$$

Next, substitute equation (20) into (16) and solve for R_b.

$$R_b = Re\{Z\} + \frac{Im\{Z\}}{\omega}\frac{\sigma}{\epsilon} \tag{21}$$

This derivation results in the same equation for R_b as the equation found by Porterfield [3].

4.2 INSTRUMENT DESIGN

The admittance method has traditionally used analog instrumentation to measure magnitude and phase of admittance. For this study, the synchronous demodulation technique was used.

The advantage of using synchronous demodulation is its ability to limit the bandwidth of interest by demodulating only the frequencies of interest. Magnitude and phase measurements include additional bandwidth since the corner frequencies of band-pass filters must be kept at least a decade away from the center frequency to limit attenuation.

4.2.1 Complex Measurement Technique

Synchronous demodulation is a well-known technique to measure in-phase and quadrature signals. This section reviews the basics principles of the technique and how it is used to determine complex impedance in this instrument.

The measurement of impedance at a carrier frequency results in a waveform that can be represented mathematically as,

$$x(t) = p(t)\cos(\omega t) + q(t)\sin(\omega t), \tag{22}$$

where $p(t)$ is the in-phase signal, and $q(t)$ is the quadrature signal. These are equivalent to the real and imaginary parts of impedance for this instrument and must be extracted from the measured signal. Synchronous demodulation is performed by multiplying the measured voltage waveform by an in-phase or quadrature carrier frequency signal. The calculations for the in-phase signal extraction are,

$$y(t) = \big(p(t)\cos(\omega t) + q(t)\sin(\omega t)\big) \times \cos(\omega t) \tag{23}$$

The signal components can be separated through the application of a trigonometric identities, $\cos^2(u) = \frac{1}{2}[1 + \cos(2u)]$ and $\sin(u)\cos(u) = \frac{1}{2}\sin(2u)$.

$$y(t) = p(t)\frac{1}{2}\left(1 + \cos(2\omega t)\right) + \frac{1}{2}q(t)\sin(2\omega t) \tag{24}$$

The in-phase signal can now be extracted by using a low-pass filter. While multiplication of a sine wave is not easily achieved with analog components, square wave multiplication can be used as an alternative. This is implemented with a multiplexer to select between the original signal and an inverted signal, where the gating is driven by either the in-phase or quadrature square wave. Reference signals are generated using two D flip-flops that divide a 76.875 kHz signal down to 19.2 kHz in-phase and quadrature waveforms.

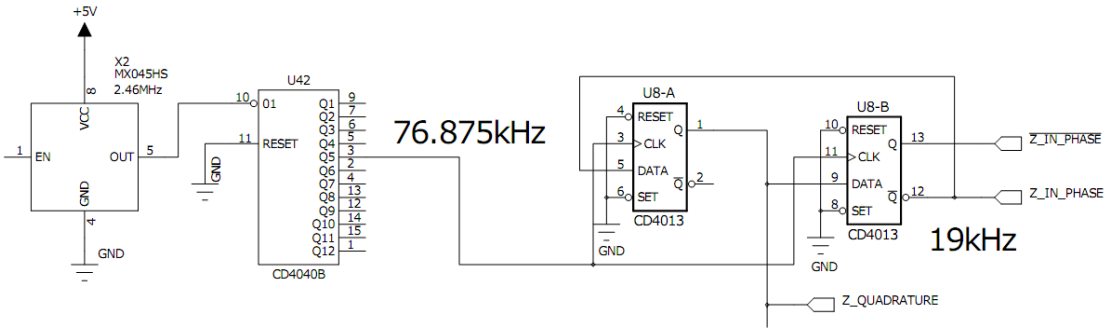

Figure 29: In-phase and Quadrature Waveform Generation

An all-pass filter, Figure 30, is used to zero out the instrumentation phase shift. The transfer function of this all-pass filter is,

$$\frac{Vout}{Vin} = \frac{j\omega(R_{109}||R_{110})C_{108} - 1}{j\omega(R_{109}||R_{110})C_{108} + 1}, \tag{25}$$

where the potentiometer, R_{110}, is used to vary the phase offset. This allows the output of the instrument to be the real and imaginary parts of impedance, without any required calibration. In order to reduce drift, all components have a C0G temperature coefficient. This is especially critical for the sine wave generation from the square wave because it is most sensitive to component variation.

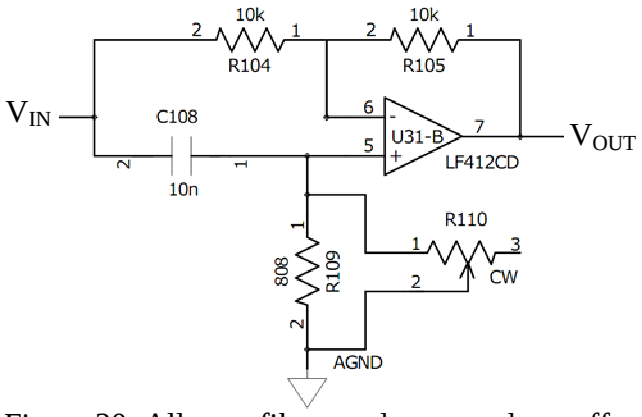

Figure 30: All-pass filter used to zero phase offset

4.2.2 ECG, EGMs and Pacing

In addition to the impedance channel, the experiment also required a surface electrocardiogram (ECG), three intracardiac electrograms (EGM), and three pacing channels. Since each of these measurements requires various connections to the pacing leads, they were all included in a single instrument. Mentor Graphic's PADs (Wilsonville, Oregon) was used to design and layout a printed circuit board. The complete schematic for the instrument is included in the Appendix.

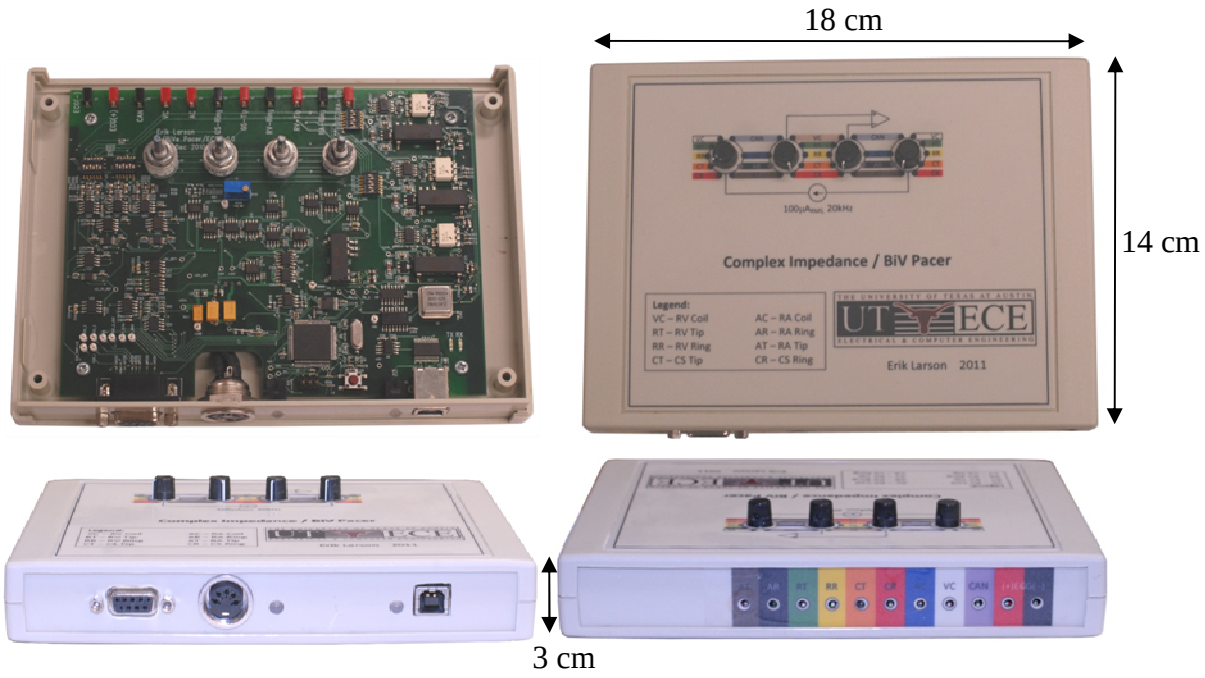

Figure 31: Printed circuit board and enclosed instrument

The three pacing channels were individually isolated using DCP010515DBP (Texas Instruments, Dallas, Texas) isolated power supplies. This was required in order to pace and measure impedance simultaneously. Pacing was implemented using a balanced current output stimulation stage [39], see Figure 32. When the circuit is not pacing, the capacitor is recharged to the stimulation voltage through the resistor and current passes in the reverse direction during stimulation. When V_{IN} = 5 V, the capacitor is shorted across the electrodes and stimulation occurs at the cathode. Since all charge must go through the capacitor, the current pulses are always balanced.

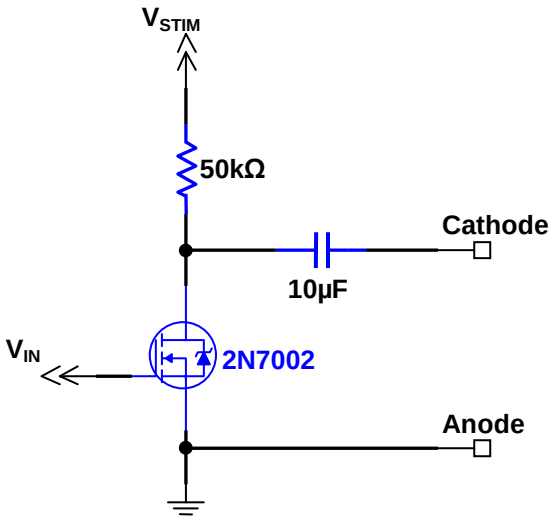

Figure 32: Pacing circuit

The surface ECG has a bandwidth of 0.05 to 200 Hz and a digitally selectable gain from 100 to 100,000. All three intracardiac EGM channels have a bandwidth of 30 to 500 Hz and digitally selectable gains between 100 and 100,000.

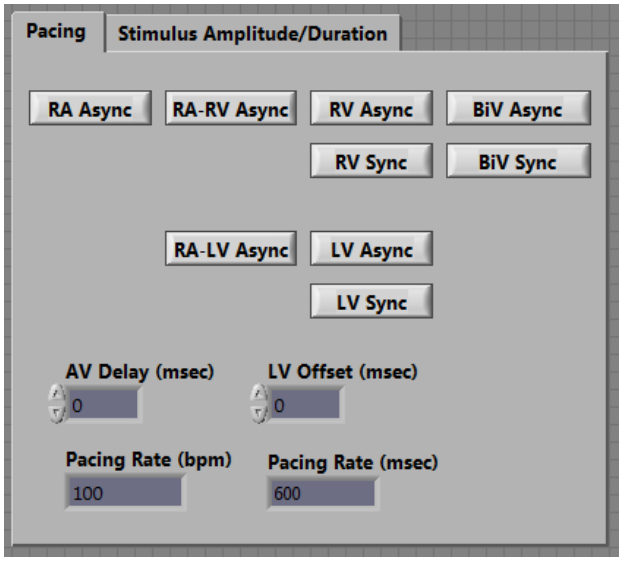

Figure 33: Pacemaker Interface

4.3 METHODS

All experiments were approved by the Institute for Animal Care and Use Committee at the University of Texas Health Science Center at San Antonio. Twelve canines weighing between 21 kg and 35 kg, mean weight of 28 kg, were anesthetized using an even mixture of ketamine and diazepam at a dosage of 1 cc/5 kg. Anesthesia was maintained with 1% to 2% isoflurane with 100% oxygen. The subjects were placed on their right side to facilitate lead placement. A solution of 6% hetastarch in 0.9% sodium chloride was infused at 0.8 to 1.2mL/kg/hr through the cephalic vein and was stopped after the pacing protocol.

A micro-tip pressure sensor (Scisense, London, Ontario) was placed in the femoral artery to monitor blood pressure. A left lateral thoracotomy was performed in order to place an ultrasonic flow probe (Transonics, Ithaca, New York) and 2D ultrasonic crystals (Sonometrics, London, Ontario). The flow probe was placed around the ascending aorta and crystals were placed into the endocardium to measure the apex-base and anterior-posterior dimensions of the LV.

Endocardial pacing leads (St. Jude Medical, St. Paul, Minnesota) were placed through the right jugular vein under fluoroscopic guidance. The leads used were the QuickFlex™ left heart lead, Tendril™ ST pacing lead for the right ventricle, and Tendril™ DX pacing lead for the RA. In one subject an OptiSense™ pacing lead was used for the right ventricular lead. The location of lead placement was chosen to simulate those used clinically. Hetastarch infusion was stopped ten minutes prior to the dopamine protocol.

The approach measures the complex impedance between the RV and lateral coronary vein (LCV) leads by applying a current between the RV tip and LCV tip

electrodes and measuring the electric potential between the RV ring and LCV ring electrodes as seen in Figure 35.

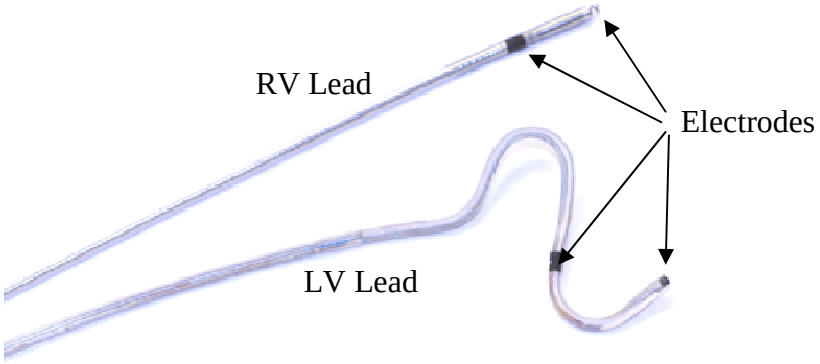

Figure 34: Biventricular pacing leads

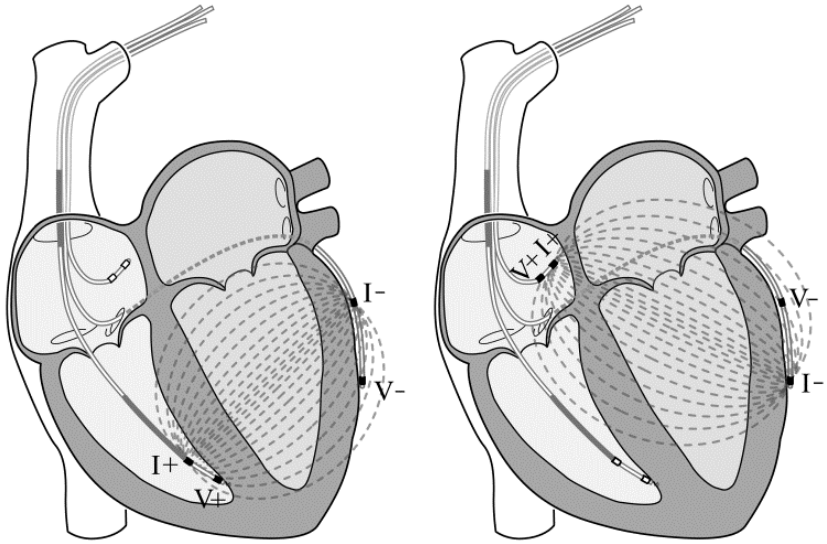

Figure 35**:** Biventricular lead measurement configurations

4.3.1 Pacing Protocol

Atrial asynchronous pacing (AOO) was performed as a steady state method to decrease stroke volume. Data was acquired at baseline (without pacing) and several rates above the intrinsic sinus rhythm in increments of 20 beats per minute (BPM) until capture

became intermittent. Ventricular asynchronous pacing (VOO) was next performed at the same rates to simulate VT.

4.3.2 Dopamine Protocol

Dopamine infusion was performed to increase LV SV. Measurements were performed at baseline and infusion rates of 1.25, 2.5, 5, 7.5 and 10 μg/kg/min. Measurements were taken ten minutes after the start of each pacing rate. Dopamine infusion was stopped if the subject became unstable as determined by femoral artery pressure and heart rate.

4.3.3 Inferior *Vena Cava* Occlusion

In a subset of 5 subjects, inferior vena cava occlusions (IVCOs) were performed as a method to determine the effect of beat-to-beat changes in LV volume on G_b. Umbilical tape was looped around the inferior vena cava and used to perform the transient occlusion.

4.3.4 Blood Conductance (G_b) Measurement

A cross LV chamber tetrapolar impedance measurement was made between the RV and LCV leads using custom instrumentation. As a secondary endpoint, similar recordings were performed between the RA and LV leads. Real and imaginary components of impedance are used to calculate G_b with the admittance method using a series muscle model [3].

An instrument was designed and constructed to measure the surface ECG, three endocardial EGMs, three pacing channels, and measure complex impedance using a 20 kHz, 100 μA_{RMS} current. Pacing was controlled using a LabVIEW (National

Instruments, Austin, Texas) graphical user interface. The device was isolated from earth ground using an isolated power supply and isolation amplifiers. The instrument uses the synchronous demodulation technique to measure real and imaginary parts of electric impedance.

All signals were sampled at 1 kHz using a data acquisition system (ADInstruments, Dunedin, New Zealand). Pacing spikes on the impedance measurements were removed by applying a 13 point median filter. Noise was present on the blood conductance signal due to electrical interference from the ultrasonic crystals. This noise was suppressed by applying a 20Hz, 10^{th} order low-pass filter in MATLAB using the Signal Processing Toolbox. Measurements were performed with the respirator off at end expiration.

4.3.5 Properties Measurement

Myocardial properties were measured between the pacing and dopamine protocols. A tetrapolar surface probe was used to measure myocardial conductivity and permittivity as well as blood conductivity. Measurement techniques are described in our previous studies [3, 12]. The probe was placed on the surface of the LV and data were collected over two or more heart beats. Five successive measurements were taken and the average conductivity to permittivity ratio was used for calculation of G_b.

Blood conductivity was monitored for stability throughout each study, as variations affect G_b. Measurements were performed before and after the dopamine protocol, which is most likely to affect blood conductivity. Hematocrit was measured using a centrifuge to determine the packed cell volume as a second method to monitor changes in blood properties.

4.4 DATA ANALYSIS

4.4.1 Ventricular Tachycardia

Each subject's VT data were searched for episodes with variations in LV SV. Unstable rhythms provide a means to show the ability of G_b to track hemodynamics in real time. LV volume was calculated from 2D sonomicrometry crystals using a prolate ellipse model [40, 41]. G_b was compared to crystal volume during irregular cardiac contractions. Ventricular fibrillation was induced in one additional subject by applying a DC voltage to the surface of the right ventricle.

4.4.2 Stroke Volume Monitoring

The ability of G_b to track SV is analyzed using results from the pacing and dopamine protocols. G_b is compared to SV derived from the ultrasonic flow probe. Aortic SV was determined from the flow probe by averaging the integrating over 3 consecutive beats.

The relationship between peak-to-peak blood conductance, ΔG_b, and SV was assumed to be linear. Baan's equation [29] was not used because it only applies to fixed electrodes, and in the current application the electrodes are in motion. SV was calculated as $SV = m \cdot \Delta G_b + b$, where ΔG_b is the peak to peak blood conductance over three heart beats. Constants m and b are derived from the acquired data using the linear mixed-effects model results for the mean slope. Baseline SV from each dataset was to calculate the offset, b, such that the baseline measurement was forced to the correct SV. This same method was also applied to peak-to-peak magnitude, $\Delta|Y|$.

4.4.3 Volume Tracking During Inferior Vena Cava Occlusions

Maximum and minimum G_b are compared to diastolic and systolic LV volume during IVCOs. G_b is converted to volume similarly to the ΔG_b conversion to SV. A linear relationship is again assumed, only the conversion results in LV volume rather than SV.

4.4.4 Statistical Analysis

Statistical analysis was performed on data acquired during the pacing and dopamine protocols as well as IVCO. Correlation analysis was not performed because multiple samples were obtained from each subject, violating the sample independence assumption. A linear mixed-effects model was used rather than a repeated-measures linear model due to the variable sample sizes from each subject.

Analysis was performed using R [42] and the linear mixed-effects model [43] to determine if a significant relationship exists between SV and ΔG_b. Subject was included as a random effect and ΔG_b was used for the fixed effect to predict SV.

Model significance was tested by obtaining p-values using a likelihood ratio test comparing the model with fixed effects to a null model with only random effects and were considered significant at the $\alpha = 0.01$ level. This analysis method was also used to determine if a significant relation exists between SV and $\Delta|Y|$ as well as between crystal volume and G_b.

4.5 RESULTS

4.5.1 Baseline Hemodynamics

Studies were completed in n=12 subjects. The mean hemodynamics at baseline were a heart rate of 120 ± 18 bpm, an LV SV of 30 ± 12 mL determined by flow probe, systolic femoral pressure of 99 ± 12 mmHg, diastolic femoral pressure of 56 ± 11 mmHg, and end-diastolic and end-systolic volumes of 43 ± 17 mL and 30 ± 14 mL determined by endocardial crystals.

Surface property measurements were successfully recorded in all but one experiment. The mean myocardial conductivity was 0.27 ± 0.02 (S/m), mean relative muscle permittivity was 20,900 ± 2,300, and the mean sigma to epsilon ratio was 1,492,000 ± 154,000 (S/F), n = 10. The mean sigma to epsilon ratio was used to apply the admittance method in subject 5, where the muscle property measurements were corrupted due to interference from an ECG monitor.

The mean blood conductivity was 0.73 ± 0.08 S/m before the dopamine protocol and 0.70 ± 0.09 S/m afterwards, n=11. The mean difference in the final minus the initial blood conductivity was -0.02 ± 0.07 S/m, n=11.

Hematocrit was also stable with a mean value of 38 ± 3 % before dopamine and 40 ± 5 % afterwards. The mean difference in the final minus the initial hematocrit was 2 ± 4 %.

4.5.2 Ventricular Tachycardia

Simulated VT was performed in 12 subjects, and 8 exhibited variations in LV SV with successful 2D crystal measurements and were the basis of further analysis. The ECG, |Y|, G_b and 2D crystal derived LV volume for all subjects exhibiting

atrioventricular dyssynchrony at rates of 140 or 160 bpm are shown in Figure 36. G_b and LV volume waveforms show similar morphologies in the presence of irregular and steady-state beats.

Hemodynamic signals before and following the inducement of ventricular fibrillation are shown in Figure 37. G_b correctly reduces to negligible amplitude during fibrillation.

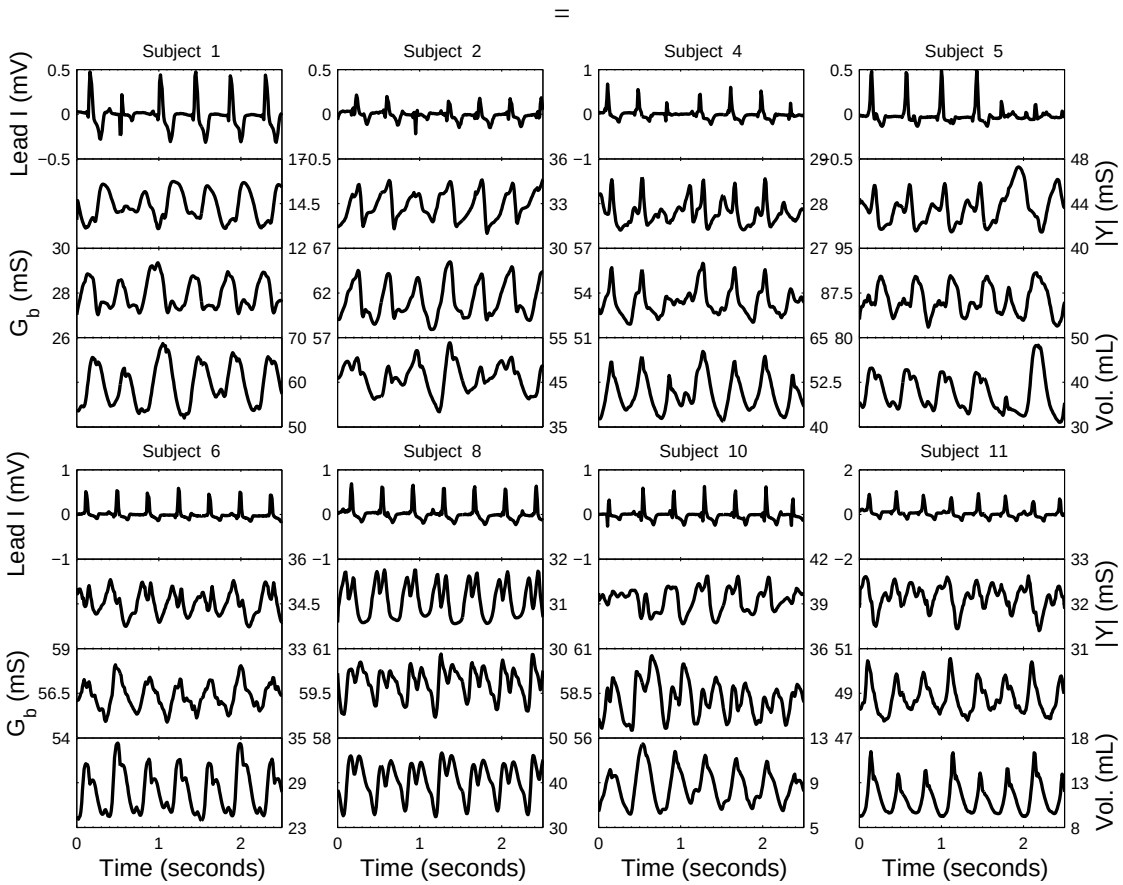

Figure 36: Simulated Ventricular Tachycardia Examples

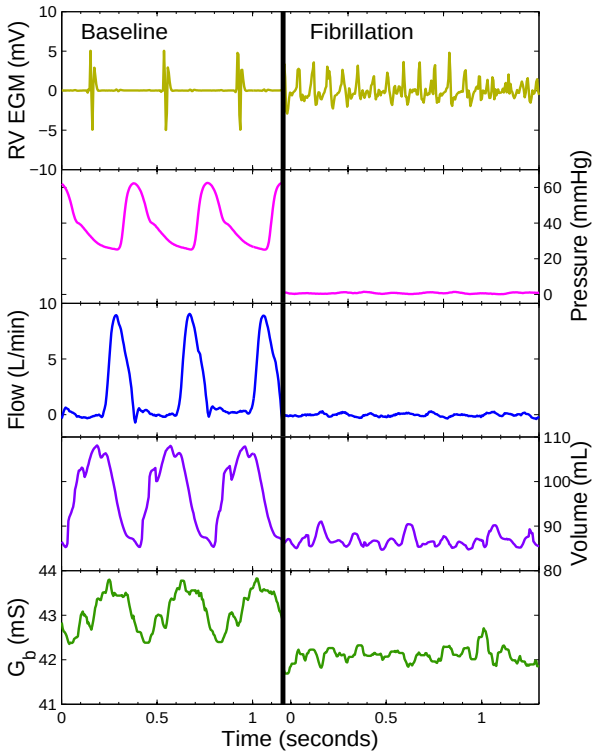

Figure 37: Acquired signals at baseline and ventricular fibrillation

4.5.3 Stroke Volume Monitoring

Dopamine infusion and pacing were used to alter SV. Example data from a single subject is shown in Figure 38. Rapid atrial pacing demonstrates G_b responds appropriately by detecting the decreasing volumes and SV. Dopamine infusion shows G_b responds appropriately by detecting decreasing end-systolic volume and increased SV. Anticipated classic responses to pacing and dopamine are evident in both the hemodynamic signals as well as G_b. One subject was excluded from analysis due to an inappropriate hemodynamic response to dopamine.

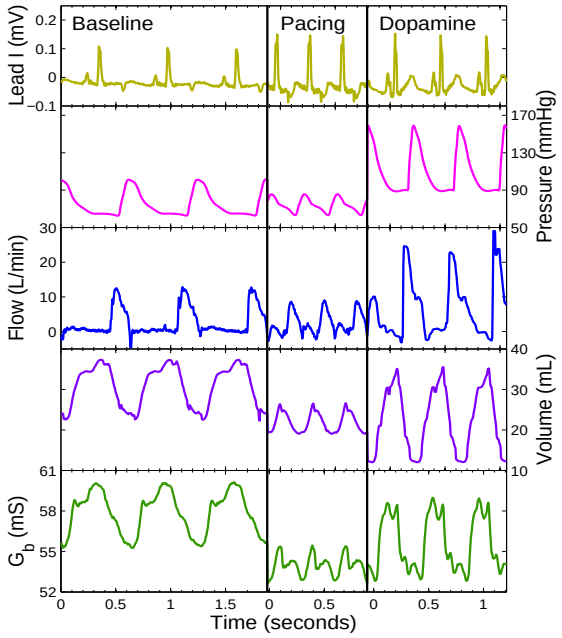

Figure 38: Example data at baseline, AOO pacing, and dopamine infusion

Results for RV to LCV measurements show that SV and ΔG_b have a significant relation ($p < 0.001$) with a mean slope of 6.54 ± 0.87 mL / mS ($t = 7.53$). SV and $\Delta|Y|$ also have a significant relation ($p = 0.003$) with a mean slope of 9.36 ± 2.94 mL / mS ($t = 3.18$). The raw data for the RV to LCV measurements are shown in Figure 39a.

Further analysis was performed to determine if removal of the myocardial signal (ΔG_b) was superior to the magnitude signal ($\Delta|Y|$), since both produced a significant relation with SV. A combined model with both ΔG_b and $\Delta|Y|$ as fixed effects was compared to a reduced model using a likelihood-ratio test by removing either the ΔG_b or $\Delta|Y|$ fixed effect. ΔG_b show a significant relationship ($p < 0.001$) whereas $\Delta|Y|$ did not show a significant relationship ($p = 0.067$), showing that ΔG_b tracks SV more accurately than $\Delta|Y|$ for monitoring SV. The raw data for the RA to LCV measurements are shown in Figure 39b.

ΔG_b and SV results for RA to LCV measurements also show a significant relation ($p < 0.001$) with a mean slope of 8.29 ± 1.85 mL/mS ($t = 4.47$). $\Delta|Y|$ also produced a statistically significant relation with SV ($p < 0.001$). Further analysis with a combined model shows that ΔG_b is not statistically significant ($p = 0.303$) but $\Delta|Y|$ is statically significant ($p = 0.007$), showing that $\Delta|Y|$ is more accurate than ΔG_b when measured from the RA to LCV.

SV from ΔG_b measured from the RV to LCV were calculated following the calibration procedure. This resulted in a good fit of the line of equal values between SV from ΔG_b and measured SV from the flow probe in most subjects, shown in Figure 40a. Although |Y| produced a significant relationship with SV, variability of the mean slope across subjects prevents SV from |Y| from fitting the line of equal values in nearly every subject in Figure 40b.

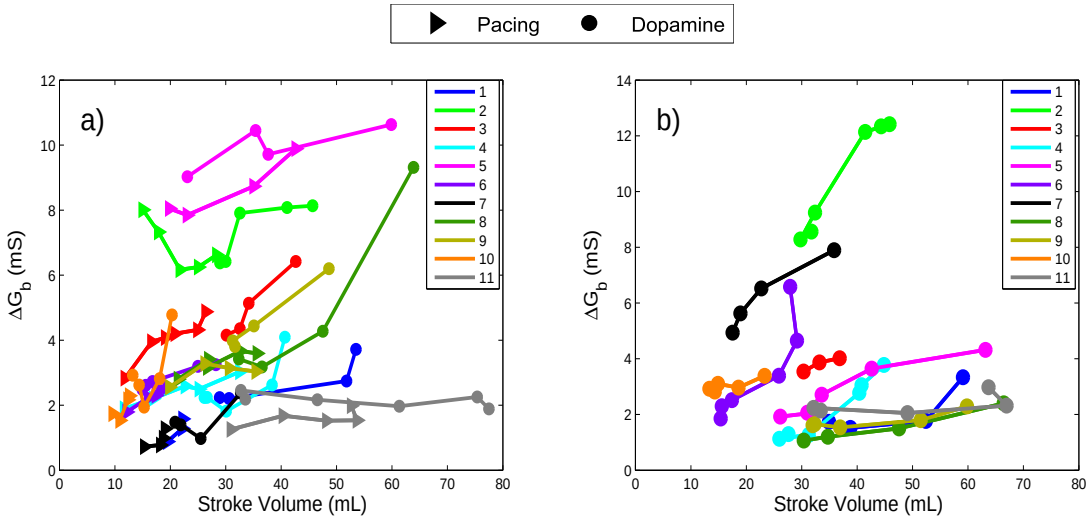

Figure 39**:** (a) ΔG_b vs. SV measured from the RV to LCV and (b) ΔG_b vs. SV measured from the RA to LCV

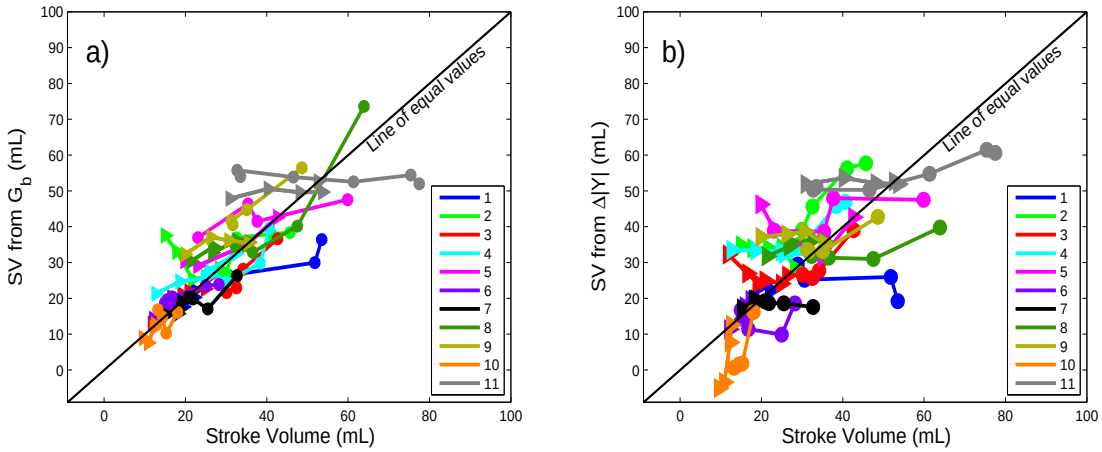

Figure 40**:** Calibrated data for (a) ΔG_b and (b) $\Delta|Y|$ vs. SV measured from the RV to LCV

4.5.4 Volume Tracking During Inferior Vena Cava Occlusions

IVCOs were successful in all 5 subjects where it was attempted. A representative measurement is shown in Figure 41. End-diastolic and end-systolic G_b consistently tracks crystal volume, including the greater decrease in EDV than ESV and fall in SV on a beat-by-beat basis in 4 of 5 subjects. |Y|, however, tracks the fall in volume but is not physiologic since the fall in ESV is too extreme, and the SV increases down the ramp in 3 of 5 subjects.

Analysis of all n=5 subjects derived from the end systolic and end diastolic volumes are shown in Figure 42. The linear fixed-effects model results for the RV to LCV measurements during IVCOs indicate a significant relation between crystal volume and G_b ($p = 0.002$) with a mean slope of 3.06 ± 0.62 mL/mS.

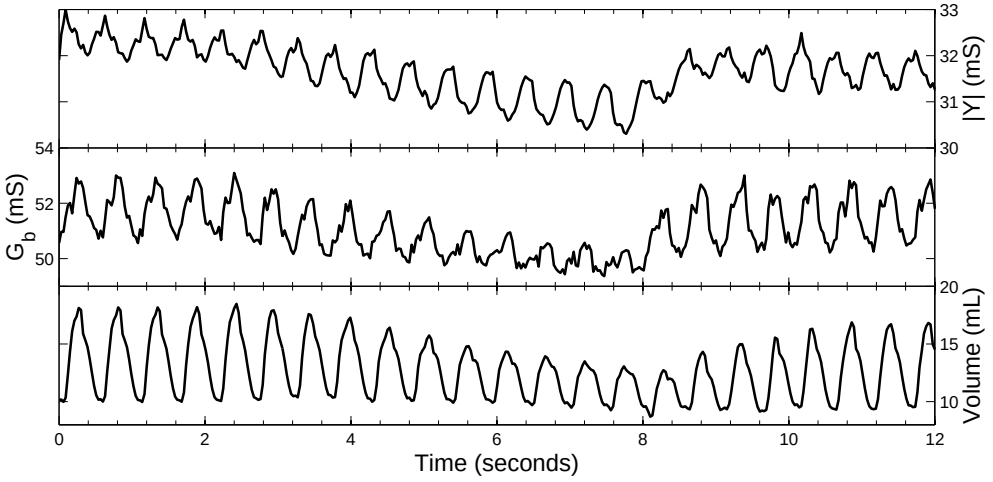

Figure 41: |Y|, G_b and LV volume during IVC Occlusion

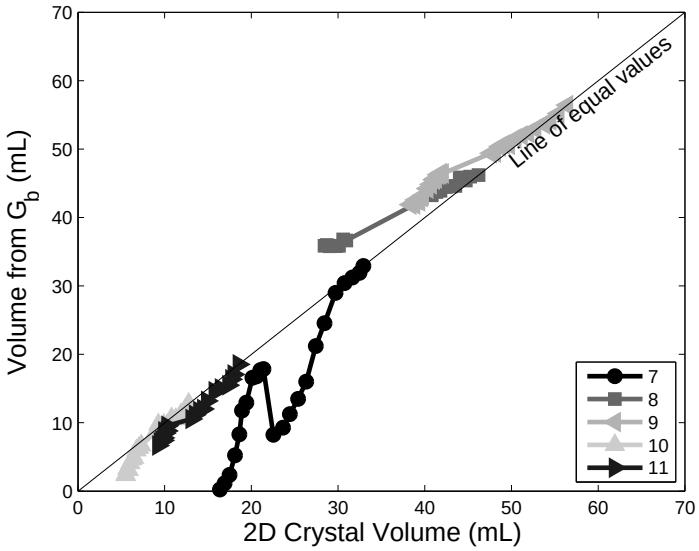

Figure 42**:** Volume from G_b vs. Volume for IVC occlusions**.**

4.6 DISCUSSION

Biventicular pacing leads were used to determine LV G_b using the admittance method for the first time. Results from this study demonstrate that 1) G_b tracks LV

volume during simulated VT better than |Y| with beat-to-beat variations in LV SV due to AV dyssynchrony, 2) the relationship between ΔG_b and SV is statistically superior to $\Delta|Y|$ and SV, 3) G_b tracks the correct LV volume physiology during IVCOs and 4) FE models show the admittance method shifts the weight of the measurement towards the LV blood pool. It is clearly advantageous to remove the muscle component from the signal, which results in improved reliability in monitoring of LV hemodynamics.

Simulated VT data in Figure 36 shows that the admittance method more often matches the morphology of 2D crystal derived LV volume and is more robust to artifact than magnitude only analysis. G_b shows a similar morphology to volume in 7 out of 8 subjects whereas |Y| is only similar in subjects 2, 4, 6 and 8, and |Y| contains artifact in subjects 4 and 6. On a beat-to-beat basis, G_b is able to track reduced or increased SV, and missed beats in all subjects more reliably than |Y|. The best examples of G_b tracking 2D crystal volume are subjects 2, 4, 6, 8 and 11, where the morphology, timing and beat-to-beat variations line up extremely well.

Pacing and dopamine results demonstrate the improved reliability of ΔG_b vs. $\Delta|Y|$ for the monitoring of LV SV. ΔG_b was found to be statistically superior to $\Delta|Y|$, and the variability in the mean slope across subjects is larger for $\Delta|Y|$. This is evident in Figure 40, where for most subjects SV from ΔG_b follows to the line of equal values, whereas SV from $\Delta|Y|$ does not. Similar sensitivities of ΔG_b to LV SV across subjects allow more robust ICD algorithms to differentiate between stable and unstable rhythms.

Finally, IVCOs show G_b can more reliably track LV volume than |Y|. It is apparent that removal of the muscle component of the signal improves the reliability of G_b tracking classic physiology compared to |Y|.

Modeling results show the application on the admittance method with biventricular leads focuses the measurement sensitivity towards the LV blood pool.

Electrical measurements are inherently weighted towards changes in close proximity to the electrodes where the current density is highest, near the myocardium. The admittance method is unable to completely remove the muscle signal due to the complex geometry of the electric current densities, but despite this limitation, the admittance method is able to reduce the contribution of the myocardium in the area closest to the electrodes.

The most common cause of inappropriate shocks is due to the inability to discriminate between AF or SVT and VT [44, 45]. The large number of patients receiving inappropriate shocks demonstrates a clear need for better algorithms to discriminate between hemodynamically stable and unstable arrhythmias with ICDs. Almost every patient in need of a shock receives one. EGM analysis is excellent at identifying arrhythmias that may require a shock, but has trouble differentiating between necessary and unnecessary shocks. Thus, the false positive rate for rhythms to be shocked is too high, and we are proposing the addition of hemodynamic monitoring with G_b to current algorithms to reduce the number of inappropriate shocks in patients through sequential testing to increase specificity. Specifically, G_b could be included in ICD algorithms to 1) differentiate between hemodynamically stable and unstable arrhythmias assessed by LV SV monitoring, and 2) reduce oversensing and double counting errors via SV monitoring. The addition of G_b allows for treatment or observation of VT episodes safely, by withholding shocks unless a significant drop in cardiac output (CO) is detected. This allows arrhythmias to self terminate or respond to anti-tachycardia pacing.

G_b can be incorporated into ICD algorithms as follows. EGM signals would continue to be the initial method to indicate the presence of an arrhythmia. Only once EGM results suggest delivery of a shock will G_b be analyzed. Analysis of ΔG_b as well as HR from G_b will determine whether or not to observe, apply anti-tachycardia pacing or deliver a shock. The algorithm will continue as follows: 1) HR is determined from G_b and

compared to HR from EGMs. If the rate from EGMs is twice the rate from G_b, the activity will be noted as double counting or oversensing and no shock will be delivered. 2) G_b and HR will be used to determine cardiac output (CO). If CO is critically low, a counter is incremented and the EGM analysis continues. Once the counter reaches 4, a shock is delivered. If the EGM analysis does not advise a shock, the counter is reset.

Rate errors can occur due to QRS double counting or T-wave oversensing. Since device programming consists of treatment zones based on HR, the incorrect assessment of an elevated HR may result in a shock. Oversensing and double counting errors may be eliminated through G_b rate analysis since G_b is periodic with heart rate due to mechanical changes of heart volume, unlike EGM signals. The addition of G_b for rhythm determination could eliminate inappropriate shocks due to HR measurement errors.

4.6.1 Limitations

Our method of sonomicrometry crystal placement was chosen to minimize myocardial damage. The base crystal was placed in the lateral wall of the LV rather than the fibrous trigone. Crystals were placed through perpendicular incisions in the myocardium, rather than oblique angles [46]. Although this crystal placement technique results in an underestimation of LV volume and calculated SV (compared to flow probe), the dynamic waveforms are representative of the true LV volume signal. This is acceptable for the purposes of the current study since the dynamic crystal signal was used for qualitative comparison to G_b data during simulated VT.

The effects of lead fibrosis could not be determined in this acute study. Fibrosis may positively impact G_b measurement, as the motion of the catheter will be reduced. This may stabilize the measurement and allow long term monitoring of LV volume in addition to SV.

Shocking leads were not used in the RV in this study. Since G_b measurement is most useful to ICDs, future studies must verify the method is unaffected by the presence of the metal coil on the shocking leads.

Shocking leads were not used in this study. Since G_b measurement is most useful to ICDs, future studies must verify the method is unaffected by the presence of shocking leads.

4.7 CONCLUSION

Cross-chamber measurement of G_b using the admittance method provides a new technique to monitor cardiac hemodynamics. The technique can be piggybacked onto ICD technology and uses standard pacing leads.

Chapter 5: Finite Element Modeling Studies of the Admittance Method

Tetrapolar measurements of impedance were studied using finite element models to compare and contrast measurements and sensitivity distributions of murine conductance catheters, multi-segment catheters, and cross-chamber measurements. Analysis was performed using the Geselowitz method [47], which determines the spatial sensitivity of tetrapolar impedance measurements.

All models were implemented using COMSOL Multiphysics. The quasi-static electric model was used which uses the following governing equations for a source-free medium:

$$\boldsymbol{J} = \left((\sigma + j\omega\epsilon)\nabla V\right) \tag{26}$$

$$\nabla \cdot \boldsymbol{J} = 0 \tag{27}$$

Here, $\boldsymbol{J}$ is the current density, σ is the conductivity, ω is the radial frequency, ϵ is the permittivity, and V is the electric potential. The quasi-static model is acceptable since the maximum dimension of the geometry is much smaller than the wavelength at 20 kHz.

Four electrodes were used in each model representing the tetrapolar measurement. The current source is set with the boundary equation,

$$\iint_{E1} -\boldsymbol{n} \cdot \boldsymbol{J} dS = I, \tag{28}$$

where E1 is the surface of electrode 1 and I is the current. Electrode 4 was the current sink where and the potential boundary condition was set to V = 0. The outermost boundary surrounding the medium is set to electrical insulation, $-\boldsymbol{n} \cdot \boldsymbol{J} = 0$. The remaining internal boundary conditions were set as $\boldsymbol{n} \cdot (\boldsymbol{J_1} - \boldsymbol{J_2}) = \boldsymbol{0}$, where $\boldsymbol{J_1}$ and $\boldsymbol{J_2}$ are the current densities at the material interface.

5.1 TETRAPOLAR MEASUREMENTS IN UNIFORM MEDIA

This model was constructed to analyze the properties of tetrapolar measurements in uniform media. Four electrodes were placed in line with a 20 kHz current of 100 μA_{RMS} applied to the outermost electrodes. The model geometry is shown in Figure 43. The conductivity and relative permittivity of the domain are 0.2 S/m and 50,000, respectively; electrode conductivity was set to 1,000,000 S/m.

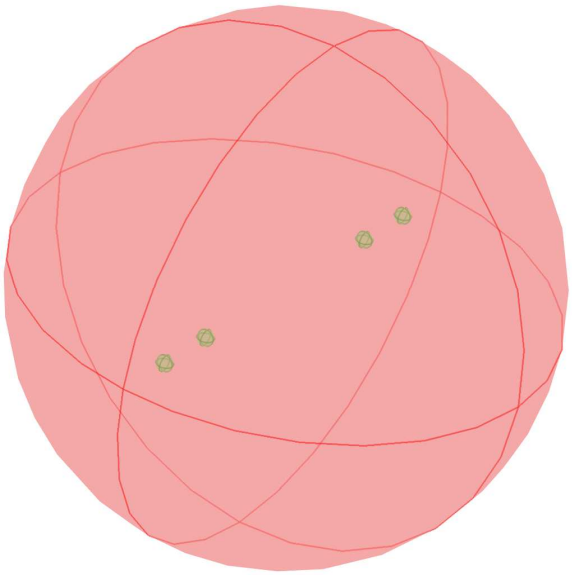

Figure 43: Geometry for tetrapolar measurement in uniform media

A cross section of the mesh is shown in Figure 44 and the mesh statistics are shown in Table 5.

Number of elements	72654
Minimum element quality	0.359
Average element quality	0.8262
Element volume ratio	1.321E-5

Table 5: Mesh statistics for tetrapolar measurement in uniform media

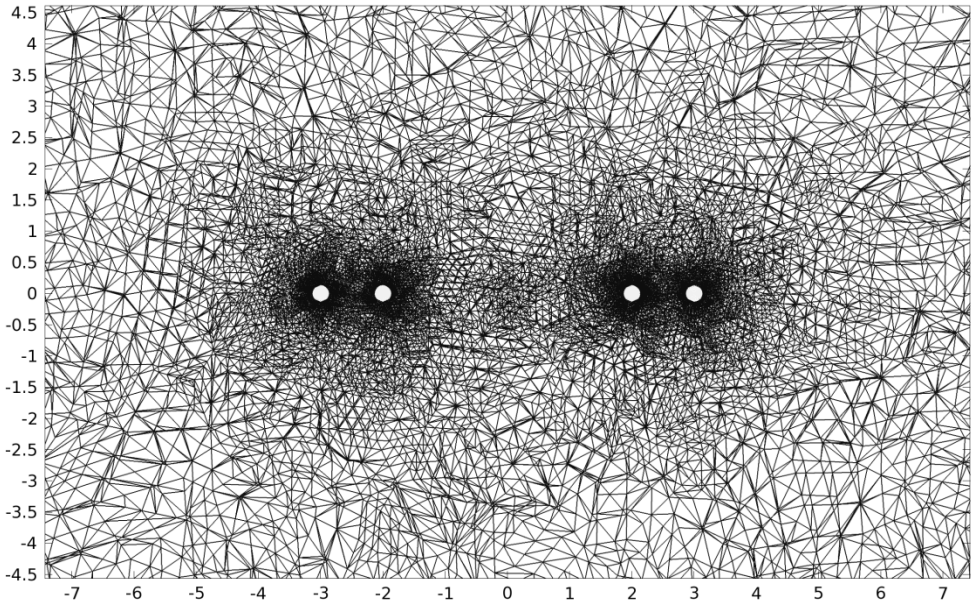

Figure 44: Cross section of tetrapolar measurement mesh

The resulting electric potential is shown in Figure 45 and the current density in Figure 46. From the potential plot one can observe that the largest changes in potential occur near the current-carrying electrodes. The current density plot also shows the highest values near these electrodes. Disturbances in the current density in Figure 46 occur near the voltage-sensing electrodes. Further analysis of the tetrapolar measurement is necessary to understand the spatial sensitivity of the impedance measurement.

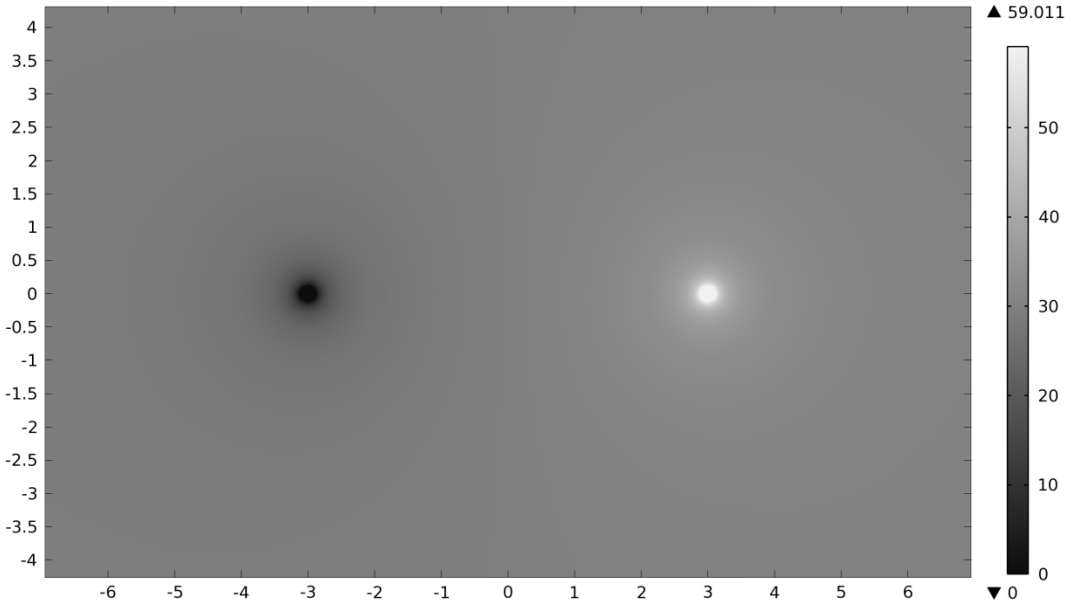

Figure 45: Tetrapolar model potential distribution (mV)

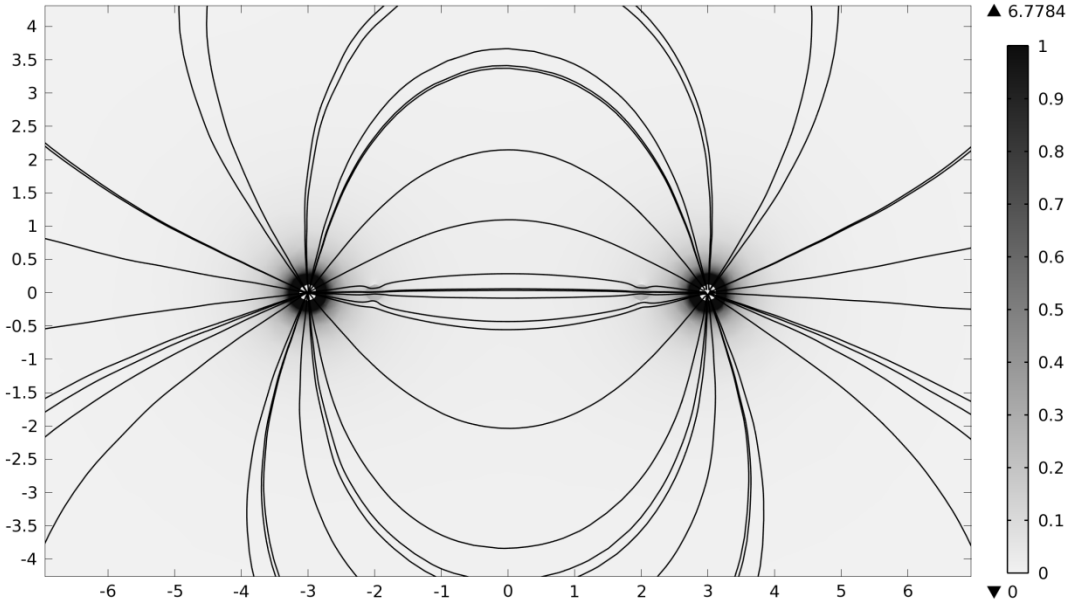

Figure 46: Tetrapolar model current density distribution (mA/m^2) with streamlines

5.1.1 Geselowitz Relation for Semiconducting Dielectric Media

Electric properties are commonly defined with respect to the bulk measurement. A medium with finite conductivity and permittivity is modeled as a parallel resistor-capacitor network. Electric conductance, G, and capacitance, C, are defined as,

$$G = \frac{I}{V} = \frac{\iint_S \sigma \boldsymbol{E} \cdot d\boldsymbol{S}}{\int_b^a \boldsymbol{E} \cdot d\boldsymbol{L}} = \sigma F, \tag{29}$$

and

$$C = \frac{Q}{V} = \frac{\iint_S \epsilon \boldsymbol{E} \cdot d\boldsymbol{S}}{\int_b^a \boldsymbol{E} \cdot d\boldsymbol{L}} = \epsilon F, \tag{30}$$

where I is the applied current (A), V is the measured voltage (V), Q is the charge (C), σ is the conductivity (S/m), ϵ is the permittivity (F/m) and $\boldsymbol{E}$ is the electric field (V/m). The surface S is any cross-section between the current carrying electrodes and the line integral is any path between the voltage sensing electrodes.

This bulk definition may lead to the incorrect conclusion that the measurement is confined to the region between the equipotential surfaces formed by the voltage sensing electrodes [48]. Properties between each pair of current carrying and voltage-sensing electrodes contribute significantly to the total measurement. Another formulation is necessary to better understand the tetrapolar measurement.

The spatial sensitivity of the measurement to each domain can be determined using the Geselowitz relationship [47-49]. Geselowitz uses a volume conductor model in his derivation. The relationship is extended to semiconductor dielectrics in the following derivation.

The domain is confined to a region with finite conductivity, σ, and permittivity, ϵ. Four electrodes are placed on the surface of the medium. The current, I, is applied between terminals A and B which results in the electric potential distribution $\varphi(\boldsymbol{r})$.

Alternatively, applying the same current between electrodes C and D results in the potential distribution $\psi(\boldsymbol{r})$. The measured impedance is the same under linear conditions due to reciprocity if the current and potential electrodes are swapped. This is only valid for the case where the positive current electrode is exchanged with the positive voltage electrode and the negative current electrode for the negative voltage electrode.

$$\boldsymbol{Z} = \frac{\varphi_{AB}}{I} = \frac{\psi_{CD}}{I} \tag{31}$$

This derivation closely follows Lehr's method, only here the combined translational and displacement current densities are used, $\boldsymbol{J}^* = (\sigma + j\omega\epsilon)\boldsymbol{E}$, rather than only the translational current, $\boldsymbol{J} = \sigma\boldsymbol{E}$. First, substitute $\psi(\sigma + j\omega\epsilon)\boldsymbol{E_\varphi}$ into the divergence theorem, and work toward a formulation of the measured impedance.

$$\begin{aligned} \iiint_{\mathrm{v}} \psi\left(\nabla \cdot \left[(\sigma + j\omega\epsilon)\boldsymbol{E_\varphi}\right]\right) + (\sigma + j\omega\epsilon)\boldsymbol{E_\varphi} \cdot \nabla\psi \, dv \\ = \oint_s \psi(\sigma + j\omega\epsilon)\boldsymbol{E_\varphi} \cdot d\boldsymbol{s} \end{aligned} \tag{32}$$

Since there are no sources within the medium, $\nabla \cdot \left[(\sigma + j\omega\epsilon)\boldsymbol{E_\varphi}\right] = 0$.

$$\iiint_{\mathrm{v}} (\sigma + j\omega\epsilon)\boldsymbol{E_\varphi} \cdot \nabla\psi \, dv = \oint_s \psi(\sigma + j\omega\epsilon)\boldsymbol{E_\varphi} \cdot d\boldsymbol{s} \tag{33}$$

The normal component of the electric field can be neglected on the surface at all points other than the applied current source and voltage sensing electrodes. Assuming that the current is supplied by a perfect conductor leaves only the applied current and potential.

$$\iiint_{\mathrm{v}} (\sigma + j\omega\epsilon)\boldsymbol{E_\varphi} \cdot \nabla\psi \, dv = \varphi_A I - \varphi_B I = \varphi_{AB} I \tag{34}$$

By dividing both sides of the equation by I^2 and substitute E_ψ for $\nabla\psi$,

$$\mathbf{Z} = \iiint_{\mathrm{v}} \frac{(\sigma + j\omega\epsilon)\boldsymbol{E_\varphi} \cdot \boldsymbol{E_\psi}}{I^2} \, dv = \frac{\varphi_{AB}}{I} \tag{35}$$

The equation can be manipulated to aid its interpretation by formulating it in terms of the combined translational and displacement current densities, $\boldsymbol{J}_{\boldsymbol{\varphi}}^{*}$ and $\boldsymbol{J}_{\boldsymbol{\psi}}^{*}$, rather than the electric fields.

$$\mathbf{Z} = \iiint_{\mathrm{v}} \frac{\boldsymbol{J}_{\boldsymbol{\varphi}}^{*} \cdot \boldsymbol{J}_{\boldsymbol{\psi}}^{*}}{(\sigma + j\omega\epsilon)I^2}\, dv \tag{36}$$

This equation reflects the measured impedance as would be observed with a tetrapolar configuration. This equation can be applied to a domain with non-uniform properties. Local integration of impedance only reflect the region's true impedance in domains oriented electrically in series. It is not valid for local integrations in parallel or mixed models since only part of the current is located in each domain, but the integration over the entire domain remains valid.

Conductivity and permittivity add in parallel. It is therefore best to analyze results in terms of admittance, Y, rather than impedance for the LV catheter. If equation (27) is multiplied by Y^2 the result is a novel form of the Geselowitz relation,

$$\mathbf{Y} = \iiint_{\mathrm{v}} \frac{\boldsymbol{J}_{\boldsymbol{\varphi}}^{*} \cdot \boldsymbol{J}_{\boldsymbol{\psi}}^{*}}{(\sigma + j\omega\epsilon)V^2}\, dv, \tag{37}$$

where V is the difference in potentials between the measurement electrodes.

Selection of the impedance or admittance formulation for analysis depends on the geometry of the model. The admittance formulation is preferred in problems such as the conductance catheter, where subdomains are electrically in parallel. Problems where subdomains are in series are best analyzed using the impedance formulation. Mixed domains present additional problems.

5.1.2 Impedivity-Sensitivity Product

The Geselowitz relationship can be plotted as a sensitivity field that shows the relative contribution of each point in the field [48]. The integrand of the impedance calculation with the local properties removed results in the sensitivity field,

$$\mathbf{S} = \frac{\boldsymbol{J}_{\boldsymbol{\varphi}}^{*} \cdot \boldsymbol{J}_{\boldsymbol{\psi}}^{*}}{I^2} \; [m^{-4}]. \tag{38}$$

This formulation works well for uniform media, but non-uniform media can better be visualized by including the local properties. If the impedivity-sensitivity product is used rather than the sensitivity alone, the result is the direct contribution to impedance per unit volume. Although the integration of the impedivity-sensitivity product over the domain results in the measured impedance, subdomain integration yields a local contribution to the measurement. The same material properties can contribute to varying intensities and some can regions even contribute negatively. Plots of the impedivity-sensitivity product show the contributions on a per unit volume basis, with local impedance,

$$\boldsymbol{Z}_{\boldsymbol{G}} = \frac{\boldsymbol{J}_{\boldsymbol{\varphi}}^{*} \cdot \boldsymbol{J}_{\boldsymbol{\psi}}^{*}}{(\sigma + j\omega\epsilon)I^2} \; [\Omega/\mathrm{m}^3] \tag{39}$$

The impedivity-sensitivity product of a 3D model with spherical electrodes in a tetrapolar measurement in uniform media is shown in Figure 47. This visualization shows the relative contribution each spatial location makes to the impedance measurement. If the local resistivity increases in a positive sensitivity zone, the measured impedance would increase. Negative sensitivity zones occur between the two stimulating and sensing pairs. Here, an increase in resistivity causes the measured impedance to decrease.

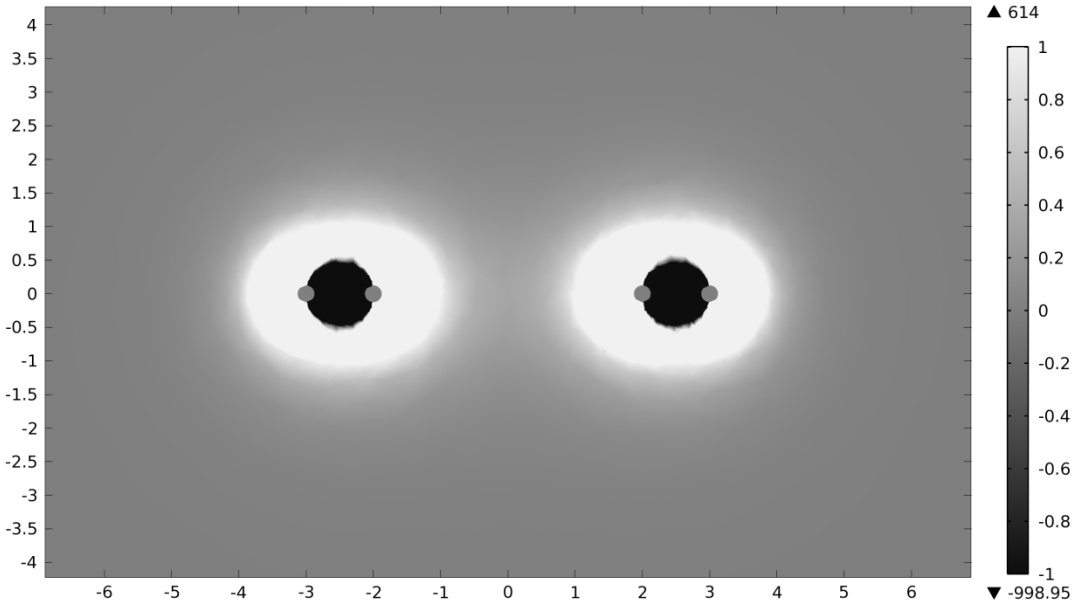

Figure 47: Impedivity-sensitivity product for tetrapolar measurement ($M\Omega/m^3$)

Due to the large range of relative contributions, the impedivity-sensitivity product was next plotted on a log scale, shown in Figure 48 in a zoomed out view. This plot shows that the contributions nearest the electrodes are at least an order of magnitude larger than the domain even 1 cm away.

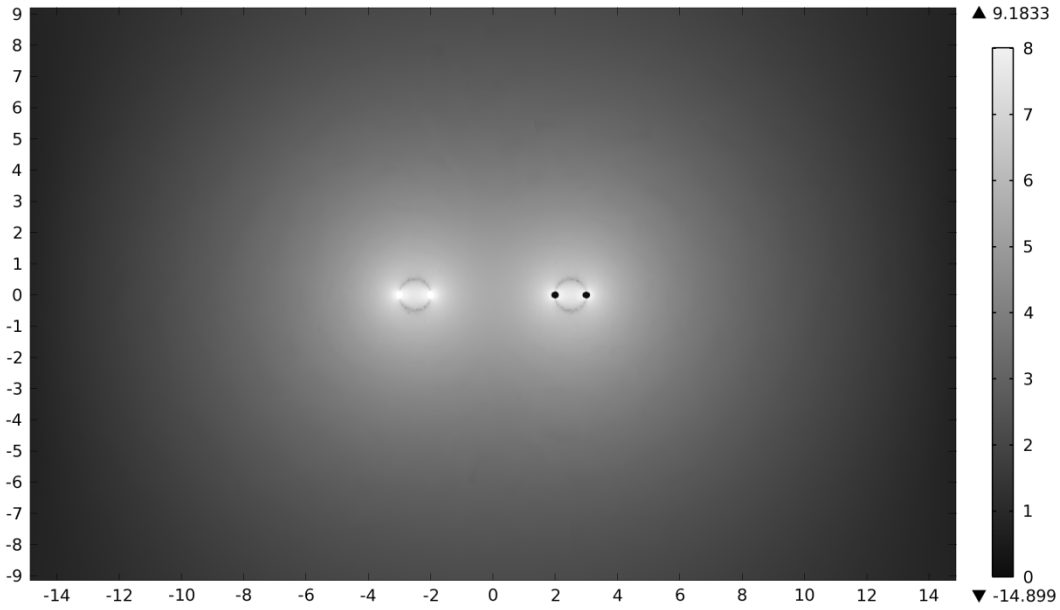

Figure 48: $\log_{10}$|impedivity-sensitivity product| ($\log_{10}(M\Omega/m^3)$) for tetrapolar measurement

5.1.3 Negative Sensitivity Zones

The existence of negative sensitivity zones is due to parallel current pathways and can be examined using a simplified circuit model. Figure 49-A represents an equivalent circuit model for the medium as seen by a tetrapolar measurement. Electrodes are labeled E1, E2, E3, and E4 and impedances represent the distributed impedance of the medium. This circuit can be further simplified by taking advantage of symmetry and removing redundant elements, resulting in the circuit shown in Figure 49-B. Here, a ground referenced current source has been applied at E1 and the voltage measurement is made at E2. This is equivalent to a differential symmetry assumption with $v_{cm} = 0$. Application of the Delta-to-Wye equivalent circuit to resistors R3, R4 and R5 allows the circuit to be solved analytically. The equivalent circuit is shown in Figure 49-C.

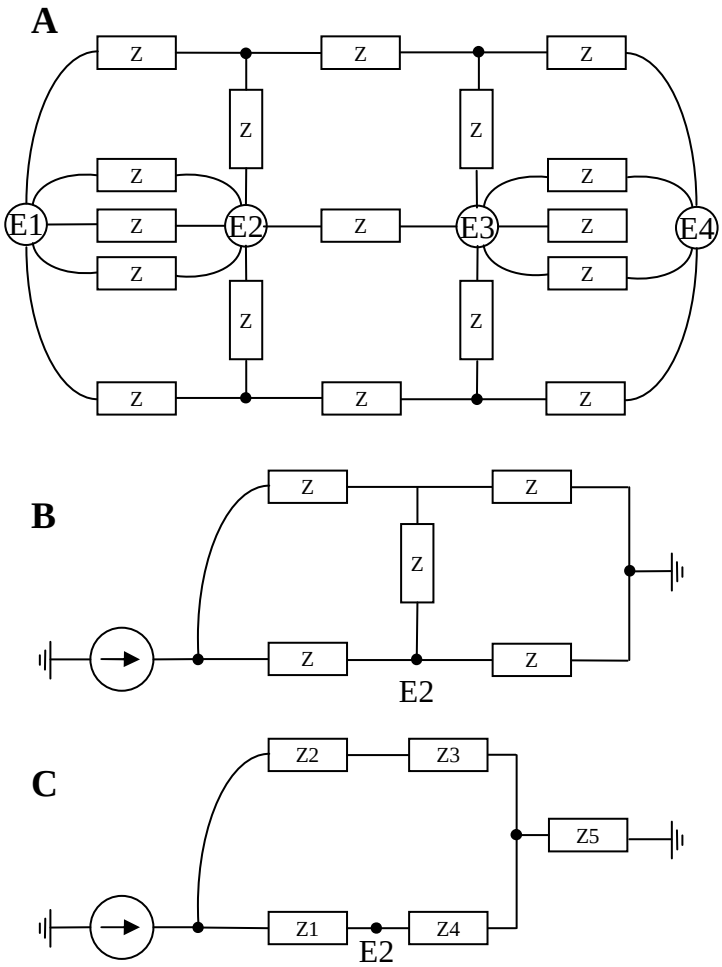

Figure 49: Equivalent circuit model as seen by a tetrapolar measurement

Solving for the measured impedance at E2 results in the following equation,

$$\boldsymbol{Z} = \frac{\boldsymbol{Z}_4(\boldsymbol{Z}_2 + \boldsymbol{Z}_3)}{\boldsymbol{Z}_1 + \boldsymbol{Z}_2 + \boldsymbol{Z}_3 + \boldsymbol{Z}_4} + \boldsymbol{Z}_5 \tag{40}$$

The relative sensitivities of the measurement to each of the impedances are,

$$\frac{\partial \boldsymbol{Z}}{\partial \boldsymbol{Z}_1} = -\frac{\boldsymbol{Z}_4(\boldsymbol{Z}_2 + \boldsymbol{Z}_3)}{(\boldsymbol{Z}_1 + \boldsymbol{Z}_2 + \boldsymbol{Z}_3 + \boldsymbol{Z}_4)^2} \tag{41}$$

$$\frac{\partial \boldsymbol{Z}}{\partial \boldsymbol{Z}_2} = \frac{\partial \boldsymbol{Z}}{\partial \boldsymbol{Z}_3} = +\frac{\boldsymbol{Z}_4(\boldsymbol{Z}_1 + \boldsymbol{Z}_4)}{(\boldsymbol{Z}_1 + \boldsymbol{Z}_2 + \boldsymbol{Z}_3 + \boldsymbol{Z}_4)^2} \tag{42}$$

$$\frac{\partial \boldsymbol{Z}}{\partial \boldsymbol{Z}_4} = +\frac{(\boldsymbol{Z}_1 + \boldsymbol{Z}_2 + \mathbf{Z}_3)(\boldsymbol{Z}_2 + \mathbf{Z}_3)}{(\boldsymbol{Z}_1 + \boldsymbol{Z}_2 + \mathbf{Z}_3 + \mathbf{Z}_4)^2} \tag{43}$$

$$\frac{\partial \boldsymbol{Z}}{\partial \boldsymbol{Z}_5} = +1 \tag{44}$$

The resulting sensitivity to changes in Z_2, Z_3, and Z_4 represent zones of positive sensitivity and Z_1 is a negative sensitivity zone. This inverse relation is due to the location of Z_1 which results in an increased current toward the sensing electrode with decreasing impedance.

Zones become either positive or negative depending on the angle between the current density fields, $\boldsymbol{J}_1$ and $\boldsymbol{J}_2$, which is due to the dot product operator in the sensitivity equation. To illustrate this point, a model was created with a material interface positioned inside the negative sensitivity zone of a tetrapolar measurement. The resulting sensitivity field near one of the pairs of electrodes is shown on the left hand side of Figure 50. In this model, medium 1 has a conductivity of 0.2 S/m and medium 2 has a conductivity of 0.7 S/m. A region of positive sensitivity is created inside the negative sensitivity zone at the material interface. The small positive sensitivity zone is present due to the change in direction of current near the interface. The higher conductivity in medium 2 draws in current from medium 1. This creates a positive sensitivity zone at the interface in medium 1. The right side of Figure 50 shows a close up view of the sensitivity zone at the medium interface, with increased contrast to show the positive and negative zones. The gray lines are current density lines of $\boldsymbol{J}_1$ and $\boldsymbol{J}_2$. Two sets of arrows help to visualize the dot product operation. Left of the medium interface, the angle between $\boldsymbol{J}_1$ and $\boldsymbol{J}_2$ is greater than 90 degrees, resulting in a negative sensitivity zone. The angle is less than 90 degrees near the material interface in medium 1, resulting in a positive sensitivity zone.

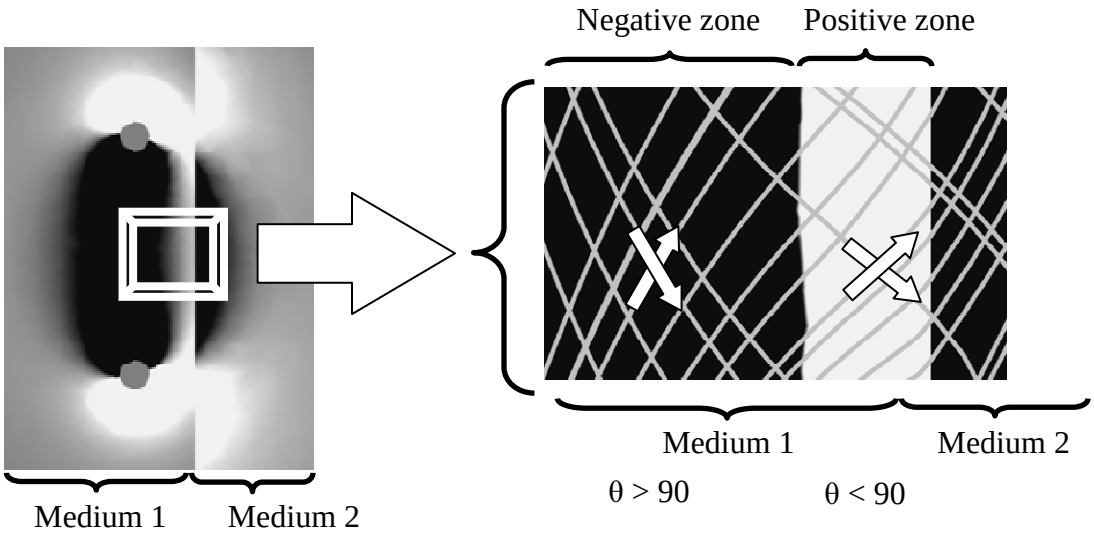

Figure 50: Current density streamlines in negative and positive sensitivity zones

5.1.4 Relative Subdomain Sensitivity

The large range of values in the impedivity-sensitivity product makes it necessary to integrate over subdomains in order to quantify local contributions to the total impedance measurement. Modifications to the tetrapolar model were made in order to allow integration over subdomains with a geometry that approximately fits the shape of the impedivitiy-sensitivity product. Concentric shells centered between each pair of stimulating and sensing electrodes are used for subdomain integration of the Geselowitz impedance. Subdomains and their relative contribution to the total measurement are shown in Figure 51.

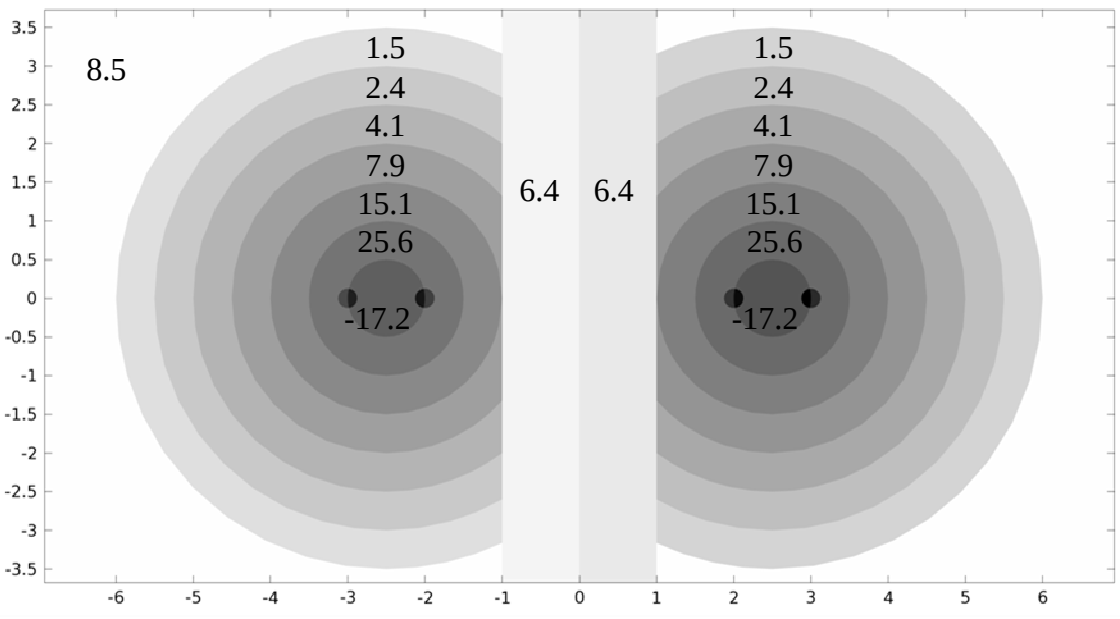

Figure 51: Relative sensitivity zones with impedance sensitivities (%)

A second method of visualizing the distribution of the impedance measurement is to use equipotential contours; evenly spaced equipotential contours on the centerline of the tetrapolar measurement are shown in Figure 52. Both methods show that the measurement is heavily weighted by the subdomains closest to the electrodes.

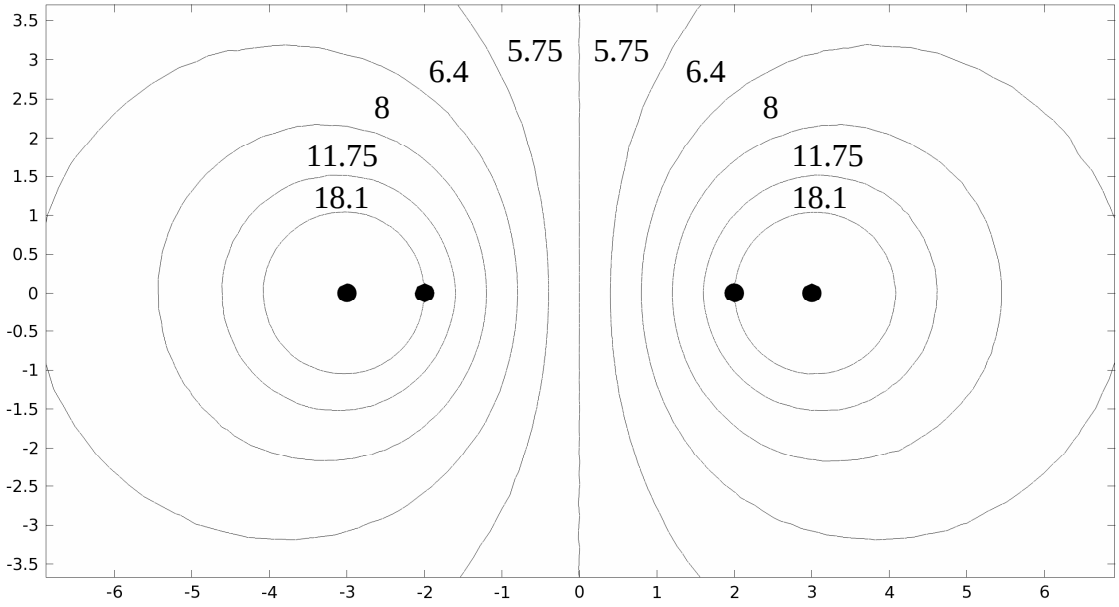

Figure 52: Equipotential contours with relative potential sensitivities [%]

5.2 CONDUCTANCE CATHETER IN THE MOUSE LV

The admittance formulation of the Geselowitz relation was applied to a murine conductance catheter with a measurement current of 10 μA_{RMS} at 20 kHz. Having a comparison method to calculate the contributions to the total admittance of each subdomain provides a means to evaluate the admittance method with conductance catheters.

5.2.1 Methods

Dimensions of the LV are based on ultrasound measurements by Gao *et al* [32], and Scisense PV mouse catheter dimensions are used for the conductance catheter. The different simulated subdomains of the model are shown in Figure 53 at diastole. Gao *et al* determined the murine LV blood diameter was 3.5 mm at diastole and 2.0 mm at systole.

The long axis of the blood cylinder was set to a constant value of 6 mm, and the exterior diameter of the LV at diastole was 5 mm. Systole corresponded to a volume of 16 μL and diastole to 48 μL. Further analysis was performed over a volume range of 15 to 60 μL for systole and diastole.

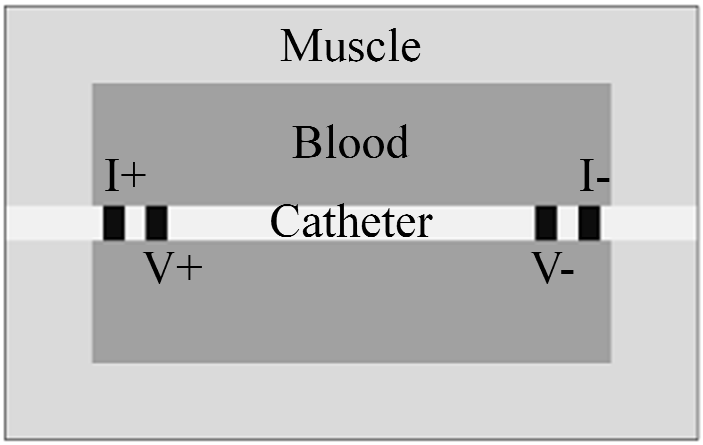

Figure 53: Mouse catheter subdomains

The catheter was placed in a simple cylinder model of the mouse left ventricle. Electrodes with a radius of 0.2 mm were spaced 4.75 mm from center to center between the inner electrodes and 5.75 mm spacing for the outer electrodes. The catheter radius was also 0.2 mm. A cross section of the mesh at 45 μL is shown in Figure 54. The mesh contains 55,547 elements, resulting in 151,480 degrees of freedom. The resulting mesh statistics are shown in Table 6.

Number of elements	55,547
Minimum element quality	0.4007
Average element quality	0.7994
Element volume ratio	1.551E-4

Table 6: Mesh statistics for murine LV model at 45 μL

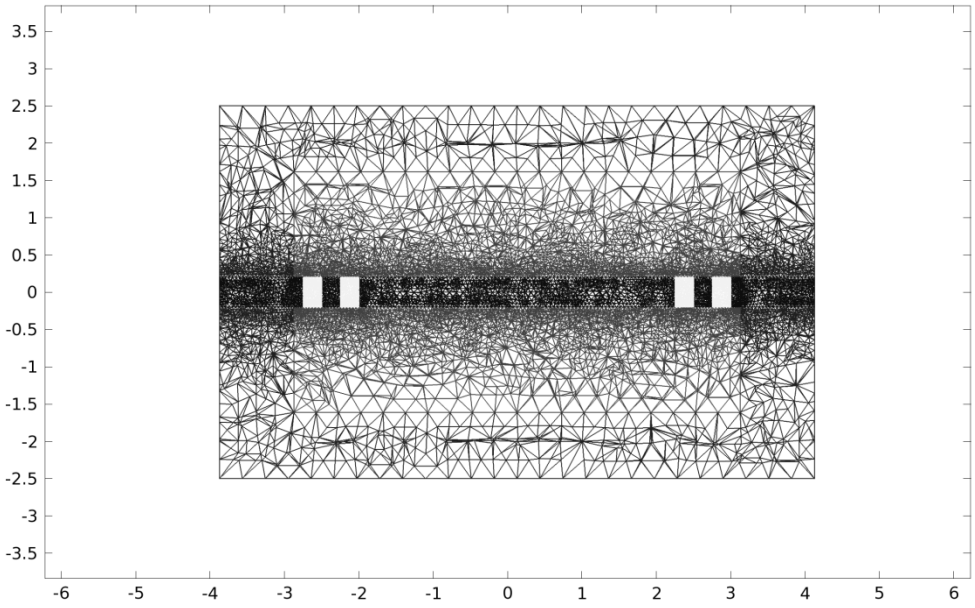

Figure 54: Cross section of murine mesh at 45 μL

Calculations of blood conductance using the admittance method and the Geselowitz relationship were compared, and blood conductance was converted to volume using Wei's equation. The hypertonic saline method was simulated by a parameter sweep on blood conductivity at systole and diastole. Blood conductivity was increased from the baseline value, 0.46 S/m, by 20% [50].

Analysis of the sensitivity distribution in the blood cavity was performed through computation of the contribution that each segmental volume makes to the total blood conductance. This was performed by integrating sensitivity over cylinders with a radius that extends to the LV endocardium, each with a height of 0.25 mm.

Surrounding's effects on admittance measurements were studied by adding a large cylinder around the simplified LV model, shown in Figure 55. The Geselowitz and admittance methods were again compared and Wei's equation was used to fit the results. A new correction factor is proposed that assumes knowledge of the true end-diastolic and end-systolic volumes, which would require the use of ultrasound experimentally.

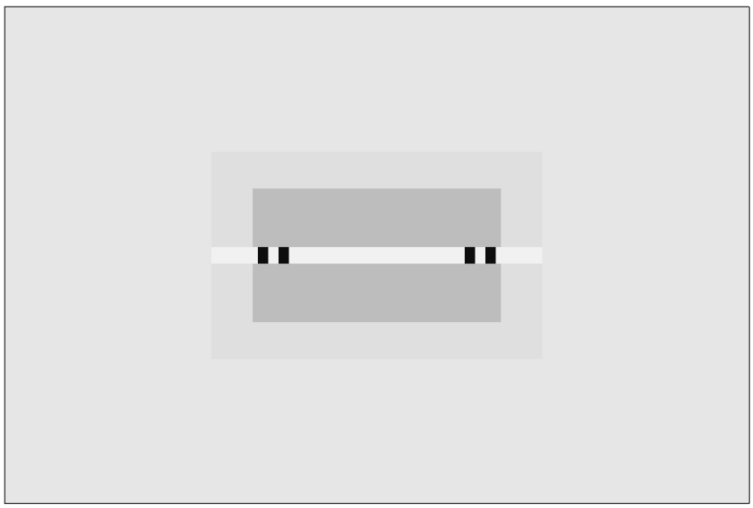

Figure 55: Mouse catheter subdomains with surroundings

5.2.1.1 Subdomain Properties

Values for conductivity and permittivity for each domain are shown in Table 7. Blood and muscle properties are based on measurements made by Raghavan *et al* [12]. A value of 0.1 S/m, based on lung measurements by Gabriel *et al* [51], was used for the surroundings in most models, and a parametric sweep was performed from 0.05 S/m to 0.4 S/m to determine the effects of conductivity on resistive losses outside the LV.

Subdomain	Conductivity (S/m)	Relative Permittivity
Blood	0.46	80
Muscle	0.16	11,800
Surroundings	0.10	80
Catheter (polymide)	10^{-12}	2

Table 7: Mouse model subdomain properties

5.2.2 Results

5.2.2.1 Mouse LV Without Surroundings

The impedivitiy-sensitivity product in the mouse LV is shown at 15 μL in Figure 56 to emphasize the removal of muscle using the admittance method. Prior to removal of the muscle signal, the muscle domain clearly contributes significantly to the measurement. Following removal using the admittance method, the contribution of the muscle domain is greatly reduced.

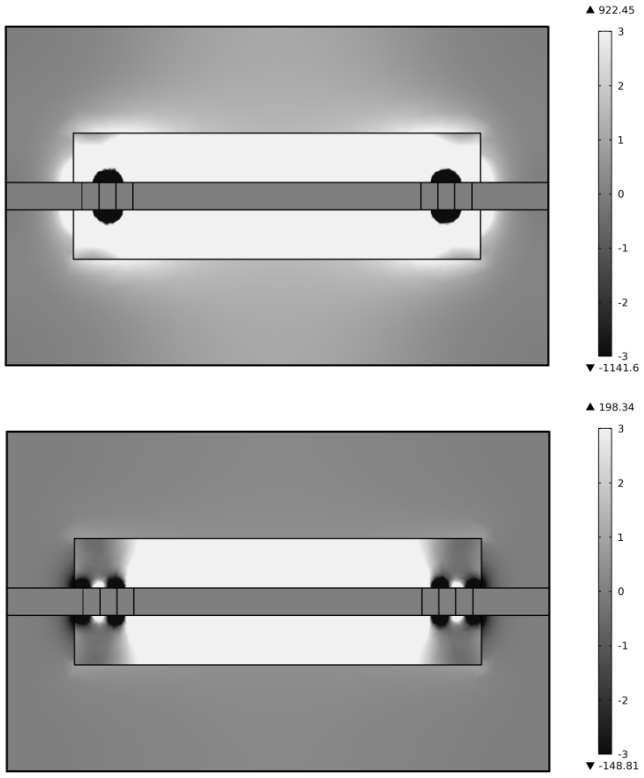

Figure 56: Product of impedivity and sensitivity (top) and the product of G_b and sensitivity (bottom) at 15 μL (μS/m^3)

Due to the large range of relative contributions, the impedivity-sensitivity product is next plotted on a log scale in Figure 57. This log plot shows that the muscle domain

still contributes to G_b, but the relative contributions are suppressed by an order of magnitude.

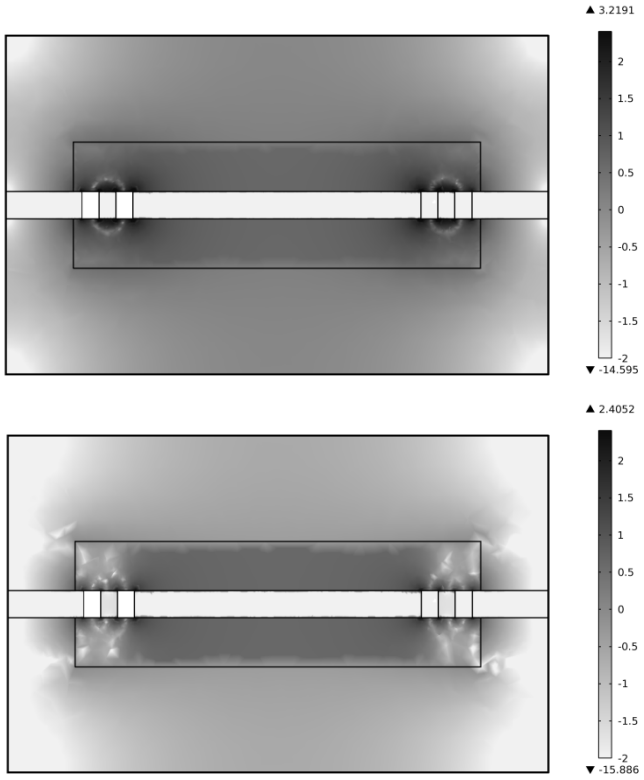

Figure 57: $\log_{10}|\text{impedivity} \cdot \text{sensitivity}|$ (top) and the $\log_{10}|G_b \cdot \text{sensitivity}|$ (bottom) at 15 μL ($\log_{10}(\mu S/m^3)$)

Relative contributions of each segmental volume in the blood cavity at various volumes are shown in Figure 58. Each point corresponds to integration over a cylinder with radius equal to the blood pool and a height of 0.25 mm, swept across the long axis of the LV at 24 locations. As expected, the greatest sensitivity is located near the electrodes. The contribution of volumes between the electrodes is comparable throughout the cardiac cycle.

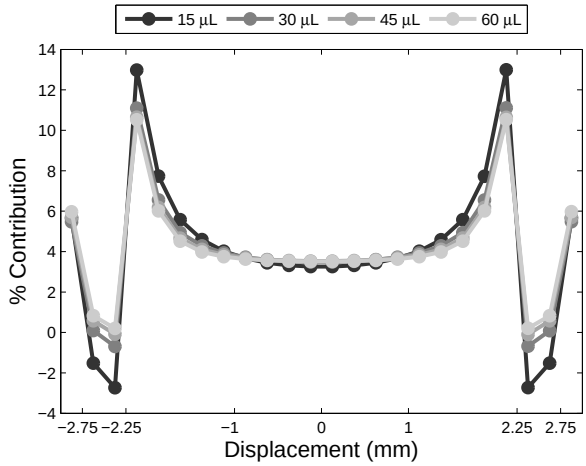

Figure 58: Percent contribution to G_b vs. displacement.

Blood conductance was then converted to volume using Wei's equation [31]. Although finite element models have previously been used to validate Wei's equation, this model includes the surrounding muscle. Volume is plotted against G_b in Figure 59. Points correspond to the data from Table 8 and the line is Wei's equation calibrated using the 15 µL and 60 µL data points. The Geselowitz and admittance methods produce nearly identical results. Wei's equation fits the blood conductance data from the mouse catheter with no surroundings. Calibration was applied using the SV and blood conductance data between 15 and 60 µL. The fit by Wei's equation correctly crosses through the origin.

Hypertonic saline simulations resulted in a least squares fit to the end-systolic and end-diastolic conductance of $G_{ES} = 0.43805 \cdot G_{ED} + 264.36$, with $R^2 = 0.99998$. Parallel conductance is found by finding the intersection of this fit to the line of identity. This results in a parallel conductance of 470 µS, which is larger than the true parallel conductance from the other methods.

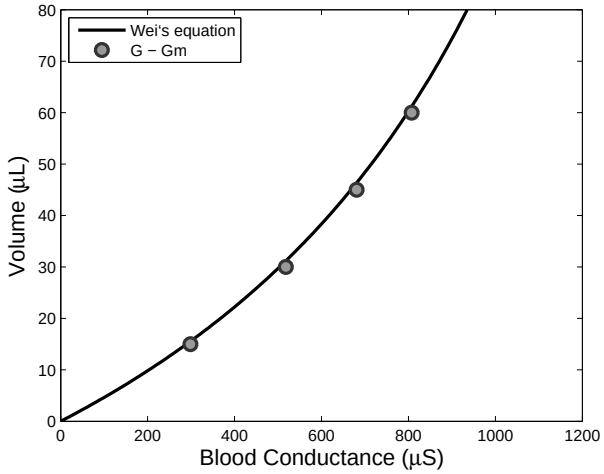

Figure 59: Volume vs. blood conductance for mouse catheter

	Admittance Method		Geselowitz Relation	
Volume (µL)	G_b (µS)	G_m (µS)	G_b (µS)	G_m (µS)
15	298.4	344.6	298.7	344.3
30	517.8	260.8	518.7	259.9
45	680.7	194.3	682.1	192.8
60	807.3	143.7	809.1	141.9

Table 8: Mouse catheter model G_b and G_m

5.2.2.2 Mouse LV with Surroundings

Results with the simple mouse LV surrounded by a conductive medium are shown in Table 9. The admittance method again correctly removes the muscle component of the signal, leaving the blood and surrounding tissue conductance. The Geselowitz relation is able to separate the blood and surrounding tissue components, and shows that the surrounding tissues contribution to measurement is significant. Results of the hypertonic saline simulation produced a value of 707 µS, much larger than the sum of muscle and surrounding conductance at any point in the cardiac cycle. The least squares fit to the

end-systolic and end-diastolic conductance was $G_{ES} = 0.47919 \cdot G_{ED} + 368.44$, with $R^2 = 0.99995$.

	Admittance Method		Geselowitz Relation		
Volume (μL)	G_b+G_s (μS)	G_m (μS)	G_b (μS)	G_m (μS)	G_s(μS)
15	521.6	395.5	372.7	393.6	150.7
30	783.7	288.5	617.2	285.7	169.4
45	943.6	21.1	775.3	214.7	171.6
60	1051.5	171.5	887.0	167.7	168.3

Table 9: Mouse model with surroundings results

An additional calibration step is necessary to remove the conductance of the surrounding tissue. If the measurement is calibrated using ultrasound, the volume is known at both systole and diastole. The conductance from surrounding tissue can be estimated as the value producing the least error at systole and diastole using Wei's equation. Application of this method to the model data results in an estimated surrounding conductance value of 77 μS. This method underestimates the true value of the surrounding conductance, but reduces the overestimation of volume from 10 μL to less than 5 μL.

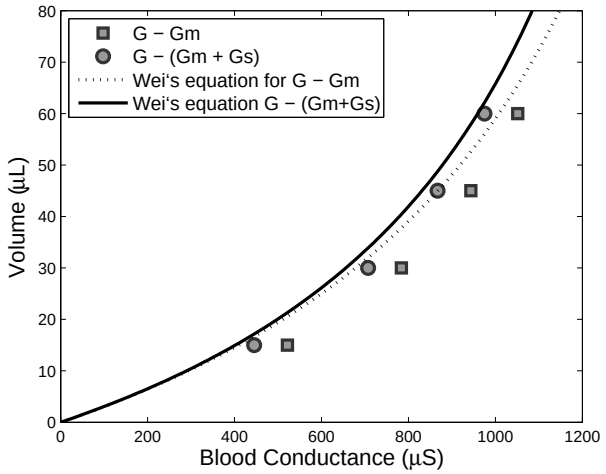

Figure 60: Mouse model results with surroundings using Wei's equation

Resistive losses from the parametric sweep over the conductivity of the surroundings are shown in Table 10 and range from 3.8 to 7.7 percent. Interestingly, the percent contribution of the surroundings to the total conductance ranges from 14 to 16 percent with conductivity of 0.1 S/m.

Surroundings Conductivity	Volume (μL) / Relative Resistive Losses (%)			
(S/m)	15	30	45	60
0.05	4.7	5.4	6.3	7.4
0.10	5.4	6.0	6.7	7.7
0.20	5.0	5.4	5.8	6.5
0.30	4.3	4.6	4.9	5.4
0.40	3.8	4.0	4.2	4.6

Table 10: Mouse model relative resistive losses

5.2.3 Discussion

Murine conductance catheter analysis demonstrates the effectiveness of the admittance method to remove parallel conductance. The calculations of blood conductance using the admittance method and the integration of the impedivitity-sensitivity product result in nearly equal values. Wei's equation correctly fits the blood conductance measurements when the surroundings are not present. In this model, addition of the surroundings shows that parallel conductance is significant from sources outside of the LV. Results using the Geselowitz method show that the percent contribution of the surroundings to the measured conductance are higher than the resistive losses suggest.

5.3 MULTI-SEGMENT CATHETERS

The admittance formulation of the Geselowitz relation was next applied to a multi-segment conductance catheter. The conductance catheter method was first

introduced as a multi-segment catheter by Baan [29]. Baan converts the segmental voltages to volume individually by assuming a uniform field, and then sums them for the total LV volume.

5.3.1 Methods

A five-segment conductance catheter was analyzed to determine the effect of multiple segments on the distribution of the sensitivity field. Each segment's sensitivity field is summed to produce the net sensitivity, according to the traditional conductance catheter method [29] with a measurement current of 100 μA_{RMS} at 20 kHz.

The catheter dimensions for this study are based on Scisense (London, Ontario) multi-segment catheters with 10 mm spacing between electrodes with the exception that the most distal electrodes are spaced 5 mm apart. The catheter geometry is shown in Figure 61. A cross section of the mesh is shown in Figure 62. The mesh consists of 38,693 elements, with 106,074 degrees of freedom. Mesh statistics are shown in Table 11.

Figure 61: Multi-segment catheter subdomains

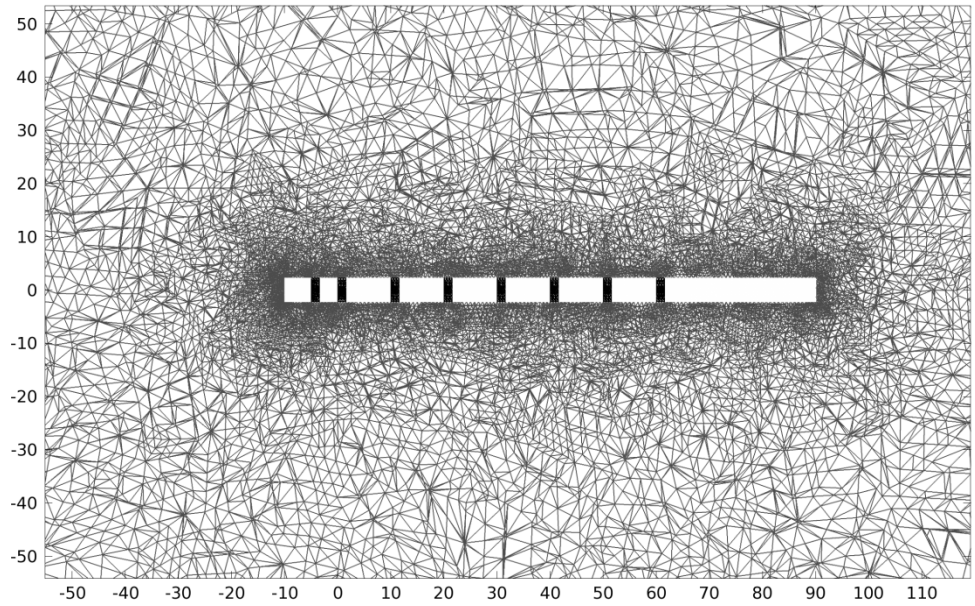

Figure 62: Cross section of multi-segment catheter mesh

Number of elements	38,693
Minimum element quality	0.2031
Average element quality	0.8045
Element volume ratio	5.193E-5

Table 11: Mesh statistics for multi-segment catheter

The five-segment catheter was placed in a cylinder of blood surrounded by muscle, in order to compare the results to the mouse catheter. The muscle radius was set to a constant value of 28 mm. The blood radius varied from to 0 to 23.2 mm, corresponding to volume up to 110 mL.

Analysis of the sensitivity distribution was performed in the same manner as the murine catheter. Sensitivity was integrated in segmental volumes in the LV blood pool in order to calculate the percent contribution to the total blood conductance. Each segmental radius extended to the myocardium with a height of 3 mm.

5.3.1.1 Subdomain Properties

Conductivity and permittivity of blood and muscle were set based on canine measurements in Chapter 4. Subdomain property values are shown in Table 12.

Subdomain	Conductivity (S/m)	Relative Permittivity
Blood	0.70	80
Muscle	0.20	20,000
Catheter (polymide)	10^{-12}	2

Table 12: Multi-segment catheter subdomain properties

5.3.2 Results

5.3.2.1 Sensitivity Field

The sensitivity field of each individual segment is shown in Figure 63. Although these five conductance signals are measured in series, Baan sums them directly, as each represents a volume signal. The result of a single segment measurement across the outermost electrodes is shown in Figure 64 along with the sum of the five conductance measurements. While the single segment sensitivity is weighted heavily towards the outermost electrodes, the multi-segment sensitivity is more evenly distributed.

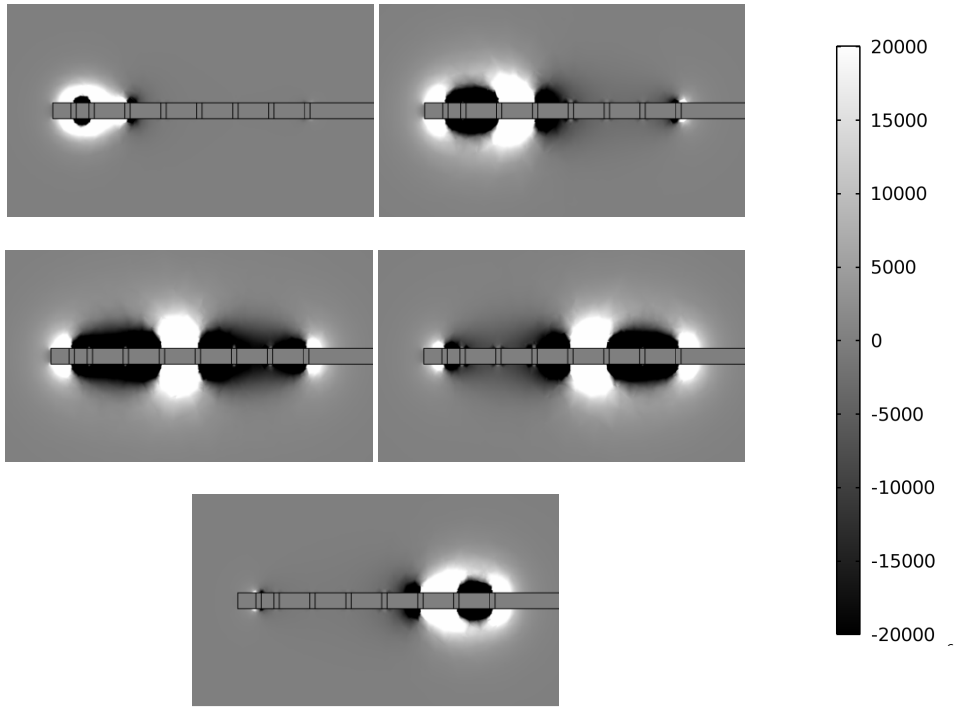

Figure 63: Five-segment catheter sensitivity for each individual segment (S/m^3)

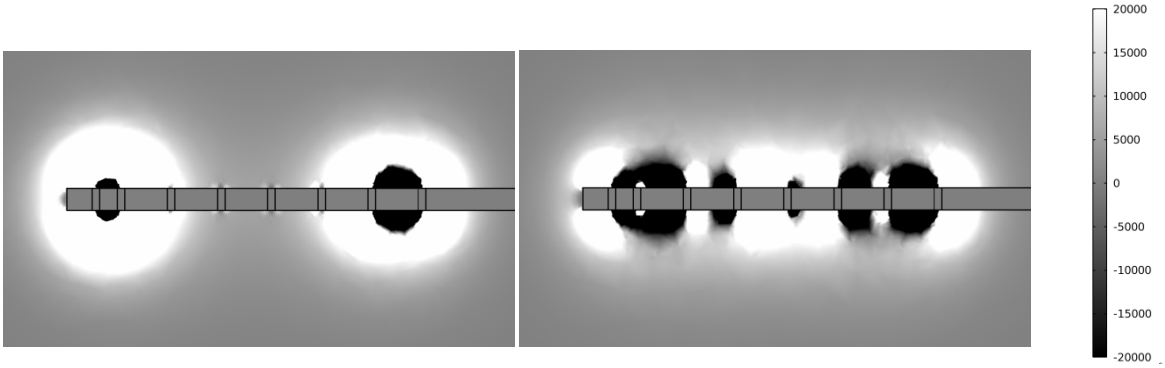

Figure 64: Sensitivity of single and multi-segment catheter measurements (S/m^3)

Next, $\log_{10}|\text{sensitivity}|$ is plotted due to the large range of relative contributions over the domain. Log plots show that the sensitivity field is more uniform the multi-segment catheter, even at larger distances from the catheter.

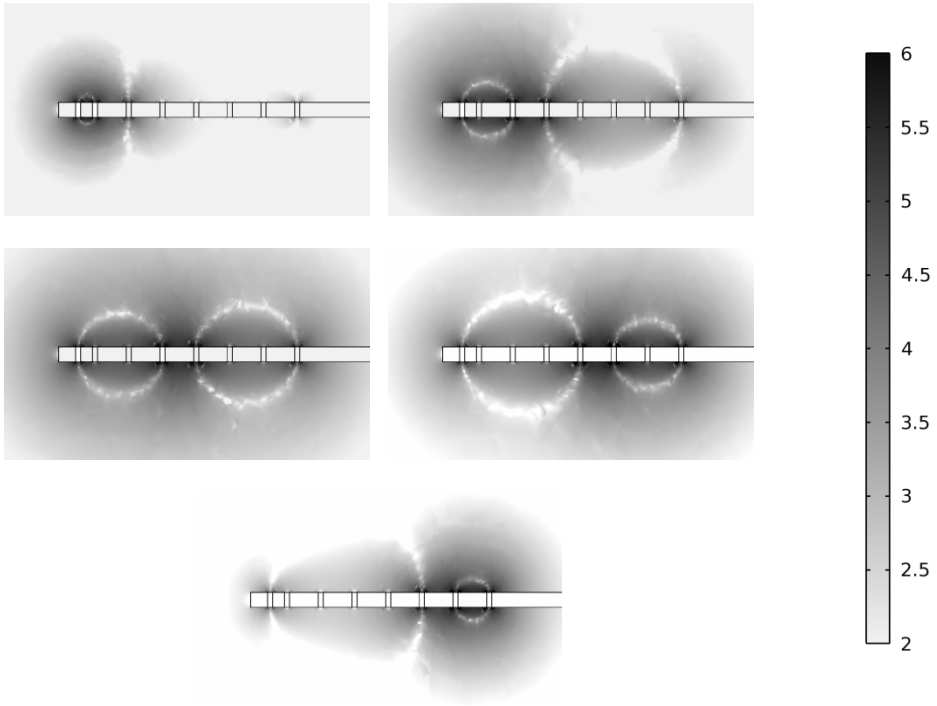

Figure 65: $\log_{10}|\text{sensitivity}|$ for each individual segment of a five-segment catheter

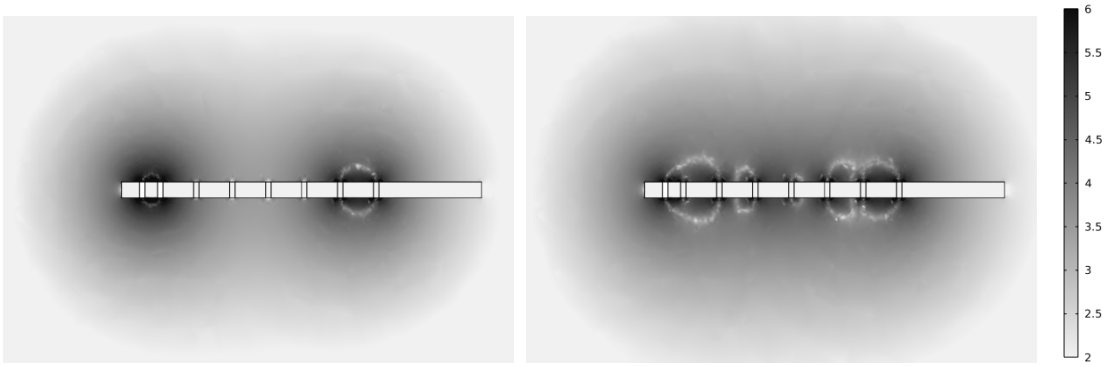

Figure 66: $\log_{10}|\text{sensitivity}|$ for single and multi-segment catheter measurements (S/m^3)

5.3.2.2 Multi-segment Catheter in a Simple LV Model

Blood and muscle conductance calculated with the admittance method and the Geselowitz relation tracked each other. Blood conductance was converted to volume using Wei's equation, and the results for single and multiple segment measurements are

shown in Figure 67 and 68. Both single and multi-segment measurements are nonlinear over this range of volumes.

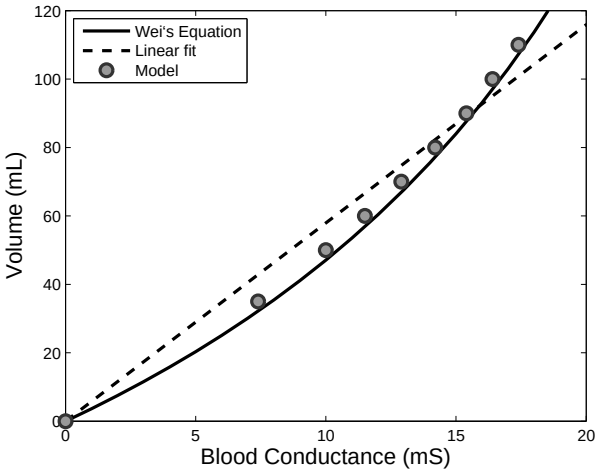

Figure 67: Large animal catheter volume vs. conductance using a single segment

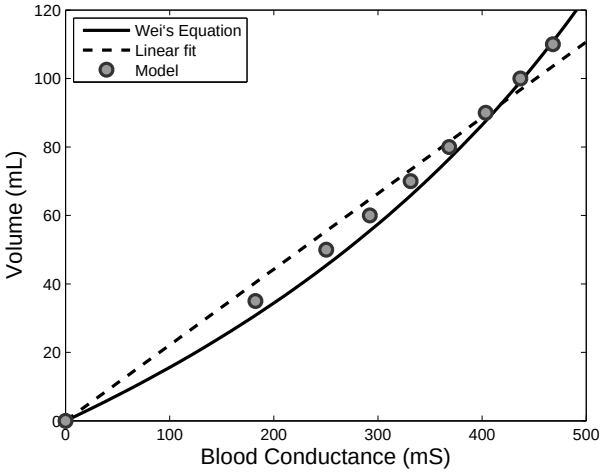

Figure 68: Large animal catheter volume vs. conductance using five segments

Segmental volume sensitivity results are shown as percent contributions in Figure 69. Single segment results are similar to murine catheter results, showing peaks at both ends of the catheter. This result is not symmetric due to a smaller spacing between the stimulating and sensing pair at the distal end of the catheter. Smaller spacing produces a

larger positive sensitivity region near the stimulating and sensing pair. Multi-segment segmental volume sensitivity results show a reduction in the peak sensitivity at the distal end of the catheter and an increase in the sensitivity of volume segments in the middle of the catheter.

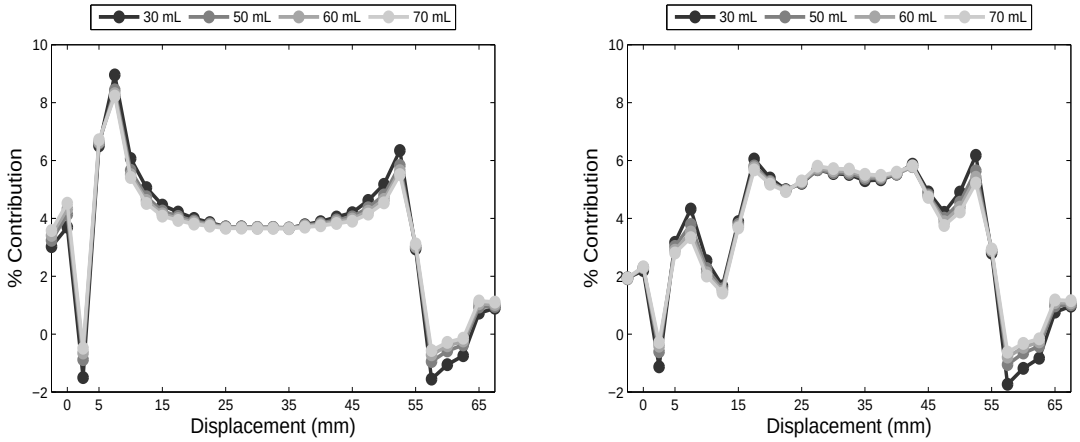

Figure 69: Single segment (left) and multi-segment (right) segmental volume sensitivity

Multi-segment measurements typically result in more physiological loops than single segment systems. This is exhibited in the experimental data discussed previously in Figure 4. Multi-segment loops stand upright while the single segment loops lean to the left. Model results show there is little difference between the single- and multi-segment measurements, but differences may be minimized due to the simple geometry of the model. *In vivo* measurements are subjected to larger variations in geometry near the apex and base of the ventricle. While these changes do affect blood volume, their influence may change the nonlinear relationship between conductance and volume. The ability of multi-segment systems to produce more physiological loops may be due to the more evenly distributed sensitivity field that is less dependent on geometry changes during isovolumic contraction and relaxation.

5.3.3 Discussion

The multi-segment conductance catheter's sensitivity field was determined using the Geselowitz relationship was formulated using admittance. This analysis shows the advantage of five segments that distribute the sensitivity field along the catheter. Analysis of blood conductance shows that both single- and multi-segment measurements can be fit using Wei's equation. Although these models suggest multi-segment measurements have no advantage, experimental data shows PV loops measured using multiple segments are more physiological than single segment loops. This is likely due to the concentration of the single segment sensitivity field to the apex and base of the LV, where the ventricle is not accurately approximated as a cylinder.

5.4 CROSS-CHAMBER MEASUREMENTS

Modeling studies are necessary to understand the origins of complex impedance measurements in the heart. This is especially true with cross-chamber impedance measurements where the signal is influenced by the geometry of blood and muscle, the distance between the electrodes, and non-uniform sensitivity. It is not possible to separate these variables in an *in vivo* experiment, but finite element models allow variations of each component independently.

5.4.1 Approximate Heart Geometry

An approximate model of the heart was constructed using dimensions from sonomicrometry crystal measurements in COMSOL Multiphysics. The geometry of the LV can be approximated as a half-prolate ellipsoid, but the RV geometry is more complex.

Sonometric crystal measurements by Rankin *et al* [46] are considered to be very accurate. Not only do their results match the stroke volume measured with an electromagnetic flow probe, the instantaneous flows also match closely. The mass of the LV varies by ± 6%.

Rankin *et al* only provide the diastolic and systolic dimensions of the LV. A linear fit between diastole and systole was used to scale the geometry to any point in the cardiac cycle. The fit was made by holding the muscle volume constant and scaling the internal dimensions linearly. The external dimensions were calculated using average value of the ratio of internal to external dimensions given at systole and diastole. The dimensions for the model are shown in Table 13. Variables *a* and *b* represent the short axis and long axis of a half prolate ellipse.

	Epicardium (cm)		**Endocardium (cm)**		
Cycle (%)	**ae**	**be**	**ai**	**bi**	**Blood Volume (ml)**
0	6.03	8.00	4.20	6.91	63.9
25	7.86	3.99	6.76	56.3	56.3
50	5.83	7.73	3.78	6.61	49.4
75	5.74	7.61	3.56	6.46	43.0
100	5.65	7.50	3.35	6.31	37.1

Table 13: Approximate Heart Geometry Dimensions.

This geometry exactly fits the interior dimensions at systole and diastole and the exterior dimensions are within 0.7 mm of the measured values. This fit geometry is preferred over the measured values as the muscle volume is held constant and parametric sweeps can quickly be run in COMSOL at any point between systole and diastole.

Electrodes are placed to represent the RV and lateral coronary vein (LCV) leads. The RV tip electrode is represented by a small cylinder placed just inside the surface of the septum and the RV ring electrode is a sphere 1 cm away from the tip. LCV electrodes

are placed on the surface of the LV and are surrounded by a small layer of muscle, which represents the lateral vein. LCV electrodes are separated by 2 cm.

The 3D rendering of the geometry is shown in Figure 70. A sphere with a radius of 10 cm encloses the approximate geometry and represents the surrounding tissues.

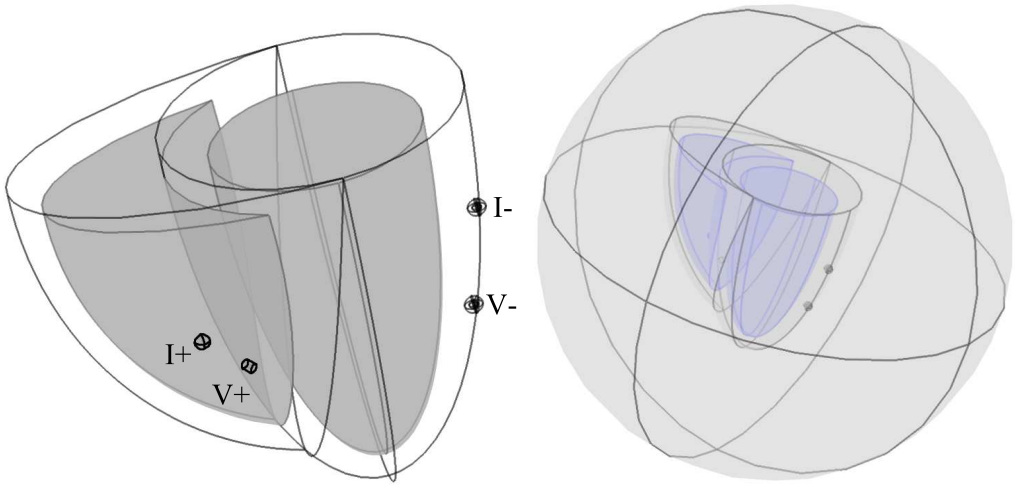

Figure 70: Approximate Heart Geometry

A cross section of the mesh is shown in Figure 71. The mesh contains 49,823 elements, resulting in 135,910 degrees of freedom. An iterative solver was used due to the large mesh size. Mesh statistics are shown in Table 14.

Number of elements	49,823
Minimum element quality	0.06852
Average element quality	0.7909
Element volume ratio	4.458E-8

Table 14: Mesh statistics for approximate heart geometry

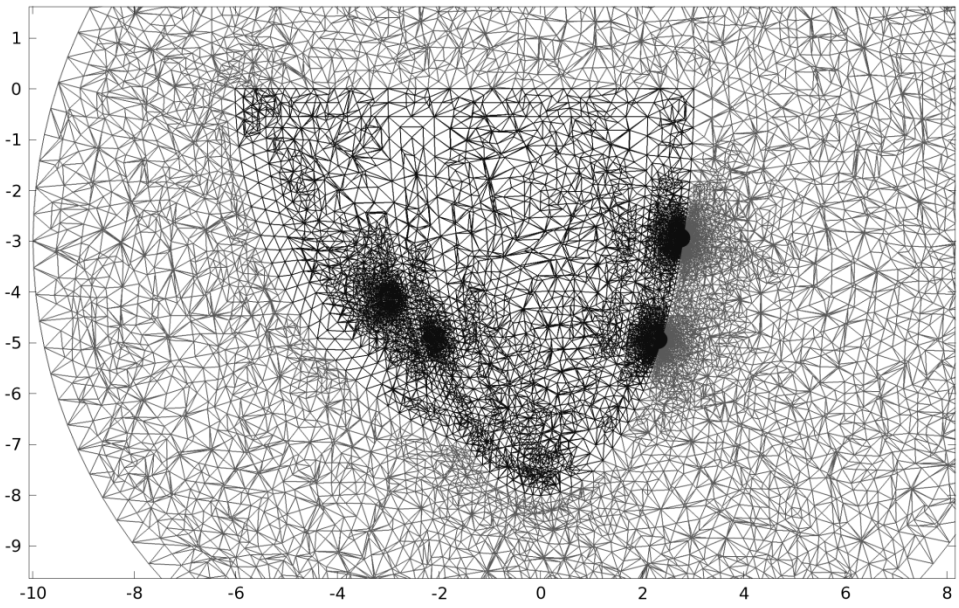

Figure 71: Cross section through mesh of the approximate heart geometry

5.4.2 Electrical Properties

The electrical properties of blood and muscle are based on measurements from the canine experiments in chapter 4. The value of surrounding tissue is from lung measurements [51].

Domain	σ (S/m)	ε_r
Blood	0.7	80
Muscle	0.2	20,000
Surrounding tissue	0.1	80

Table 15: Model electric properties

5.4.3 Boundary Conditions

A 20 kHz, 100 μA_{RMS} current source is applied between the upper electrodes in each pair. This is implemented using the terminal current source boundary condition. The external boundaries of the sphere are set to electric insulation.

5.4.4 Impedivity-Sensitivity Product

The resulting impedivity-sensitivity product is shown in Figure 72. Although the sensitivity is highest near the electrodes, the LV is predicted to make a significant contribution to the measurement.

Interestingly, the blood-muscle interface causes a zone of positive sensitivity at the muscle near the interface and a negative region in the blood. The mechanisms behind this result are described in the section 5.1.3.

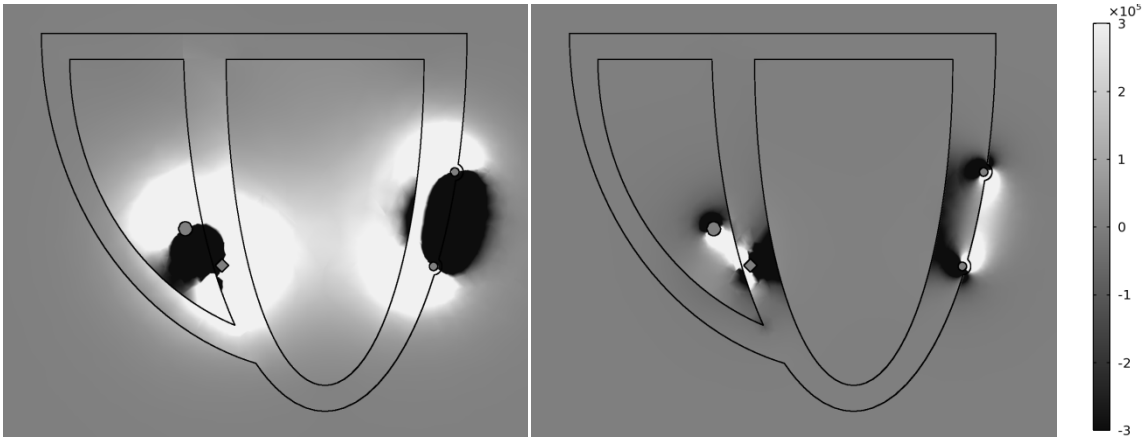

Figure 72: Approximate geometry impedivity-sensitivity product, Re{**Z**} (left) and Im{**Z**} (right) (Ω/m^3)

Due to the large range of relative contributions, the impedivity-sensitivity product is plotted on a log scale in Figure 73. The highest sensitivities are seen in close proximity to the electrodes.

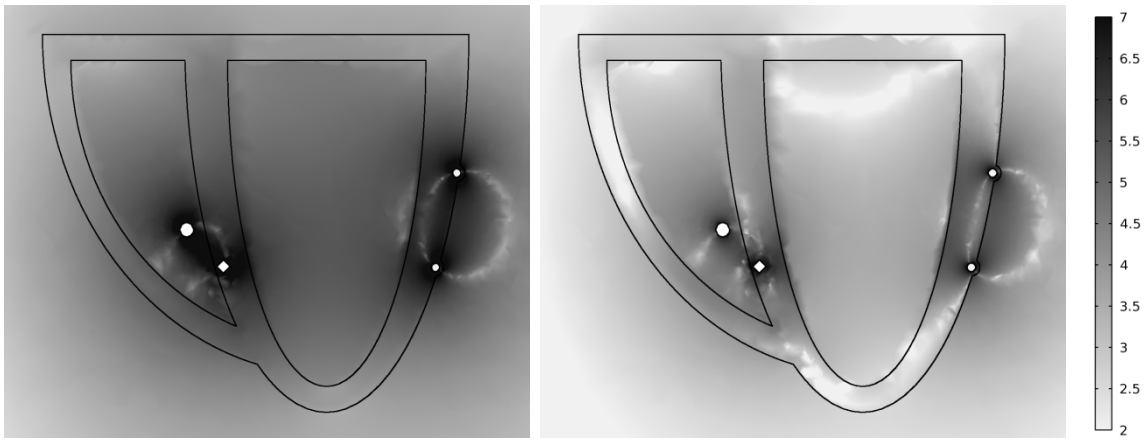

Figure 73: Approximate geometry $\log_{10}|$impedivity·sensitivity$|$, Re{**Z**} (left) and Im{**Z**} (right) (Ω/m^3)

5.4.5 Series Model Verification

The equivalent circuit model is neither series nor parallel, but a combination of the two. This study aimed to test the hypothesis that the model is more series than parallel. The sensitivity was calculated using the Geselowitz relationship using both the impedance and admittance formulations. Muscle resistance and conductance were removed by forcing either a series or parallel model, resulting in sensitivity maps for R_b and G_b. The G_b-sensitivity product from the parallel model and R_b-sensitivity product from the series model are shown in Figure 74. The scale of the G_b-sensitivity product was adjusted so that the integration over the entire domain matches for the two plots.

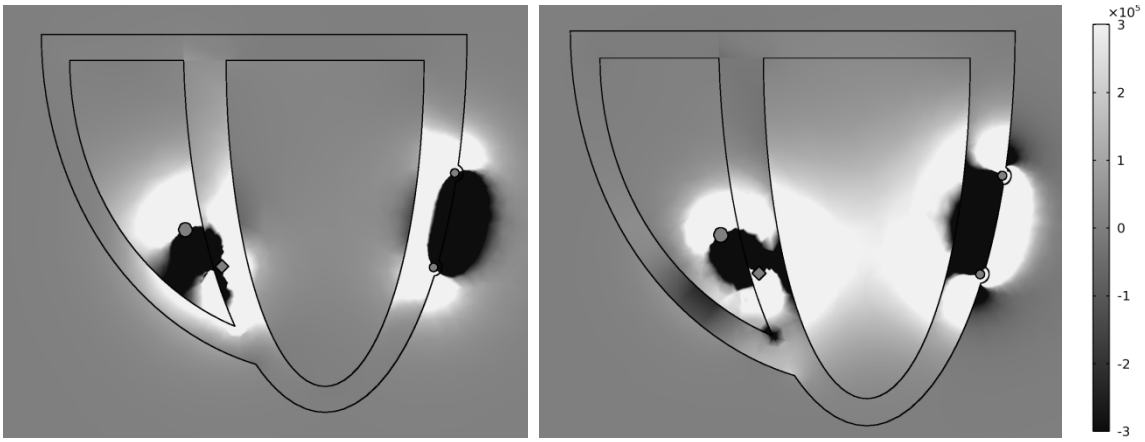

Figure 74: G_b·Sensitivity (S/m^3) from parallel model (left), R_b·sensitivity (Ω/m^3) from series model (right)

Integration of the sensitivity maps reveals the relative contribution of each subdomain. Results are shown in Table 16. The series model has significantly more contributions from the LV blood pool. These results support the use of the series model.

Subdomain	% G_b from parallel model	% R_b from series model
LV blood pool	4.2	50.2
LV muscle	16.7	6.6
RV blood pool	14.0	9.6
RV muscle	44.2	3.4
Septum	9.8	18.9
Surroundings	11.1	11.3

Table 16: Relative contributions using parallel and series models

5.4.6 Advantage of the Admittance Method with Cross-Chamber Measurements

The advantage of applying the admittance method to cross-chamber measurements is shown through comparison of relative contributions to R_b and Re{**Z**}. Relative contributions are calculated by dividing by the total Re{**Z**} and R_b. The real component of impedance is used for magnitude analysis, as the imaginary component is

small in comparison. A cross section of the relative distributions is shown in Figure 75, which demonstrates that the LV is emphasized after removal of the muscle in R_b. The scale is saturated to ±15,000 m^{-3} to emphasize the changes in the LV. The contributions from each subdomain are shown in Figure 76 and Table 17.

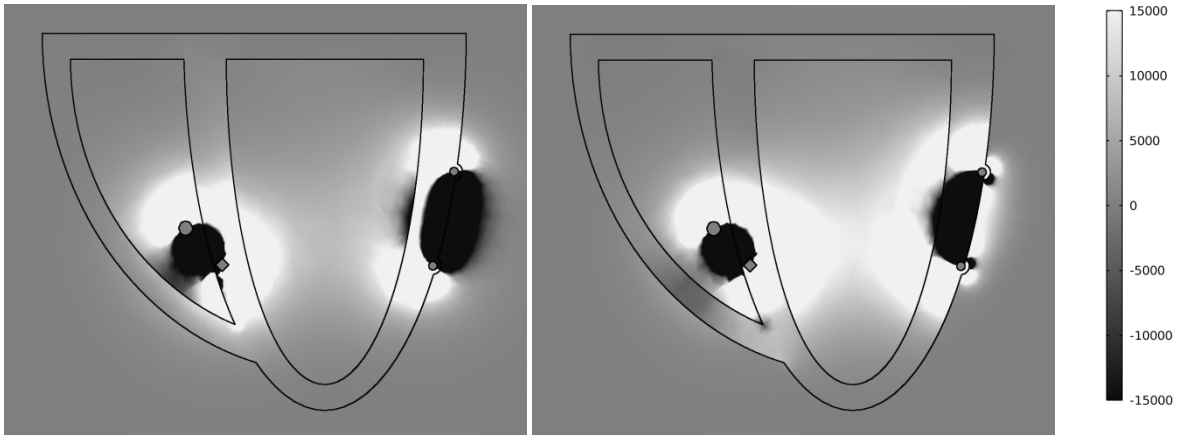

Figure 75: Relative contribution distribution for Re{**Z**} (left) and R_b (right) ($1/m^3$)

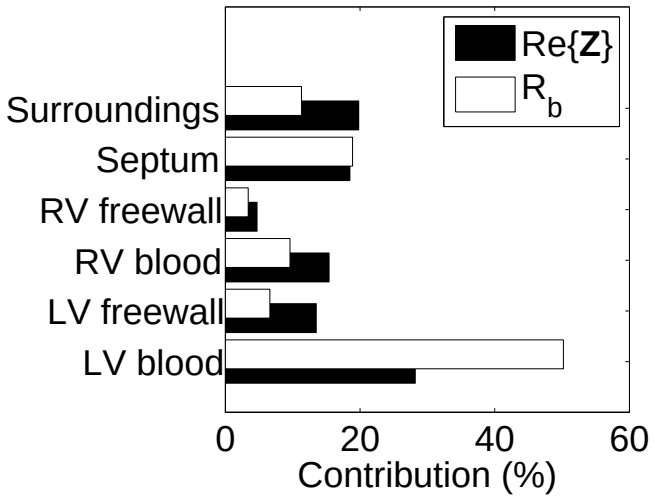

Figure 76: Relative contributions to Re{**Z**} and R_b

Subdomain	Re{**Z**} (Ω)	Im{**Z**} (Ω)	R_b (Ω)	% Re{**Z**}	% R_b
LV blood pool	8.67	0.12	9.73	28.2	50.2
LV muscle	4.16	-0.32	1.28	13.5	6.6
RV blood pool	4.73	-0.32	1.86	15.4	9.6
RV muscle	1.44	-0.09	0.66	4.7	3.4
Septum	5.71	-0.23	3.67	18.5	18.9
Surroundings	6.08	-0.43	2.19	19.8	11.3

Table 17: Relative contributions from each subdomain to Re{**Z**} and R_b

The relative contribution of the LV blood pool to R_b is greater in comparison to the Re{**Z**}. The admittance method is unable to completely remove the muscle contribution to the signal, but signal is still improved.

5.4.7 Cyclic Variations

The cycle model was employed to determine the real and imaginary values of impedance and blood conductance. The results are shown in Table 18. The real and imaginary components of impedance from the model have the opposite cyclic trend compared to *in vivo* measurements.

	Re{**Z**} (Ohms)	Im{**Z**} (Ohms)	G_b (mS)
Diastole	30.85	-1.27	51.45
Systole	33.95	-1.63	51.93

Table 18: Approximate heart geometry cyclic variation

Impedance measurements are a function of electrode geometry and domain properties. In a homogeneous conductor, impedance is proportional to the distance between the two electrode pairs. The impedance decreases as the distance between the pairs decreases. The properties of the materials between the electrodes can also change, such as the heart muscle thickening and the ejection of blood. Changing from blood to

muscle properties can either increase or decrease the impedance depending on the local sensitivity.

An additional model was created at systole to determine the magnitude of the effect of muscle in the negative sensitivity zone. The entire negative sensitivity zone was filled with muscle, and the resulting impedance is less than the diastolic value. This trend of maximums at diastole and minimums at systole, as shown in Table 19, matches the experimental results of Chapter 4. It is possible that the influence of the negative sensitivity zone in the right ventricle dominated the length and positive sensitivity zone effects. The presence of a papillary muscle alone did not reduce the impedance below the diastolic value.

	Re{**Z**} (Ohms)	Im{**Z**} (Ohms)	G_b (mS)
Diastole	33.27	-1.43	48.97
Systole	32.81	-1.25	46.40

Table 19: Systolic and diastolic measurements

A third model was created to simulate RV lead motion, see Figure 77. The RV screw electrode remains at a fixed position but the RV ring electrode moves towards the septum from diastole to systole. This type of motion is reasonable as the lead body is pushed towards the septum by the RV freewall during contraction. This model shows that Re{**Z**} and Gb decrease from diastole to systole but the Im{**Z**} increases. This small change in RV lead position causes a large enough change in the Re{**Z**} to wipe out the signal from the LV.

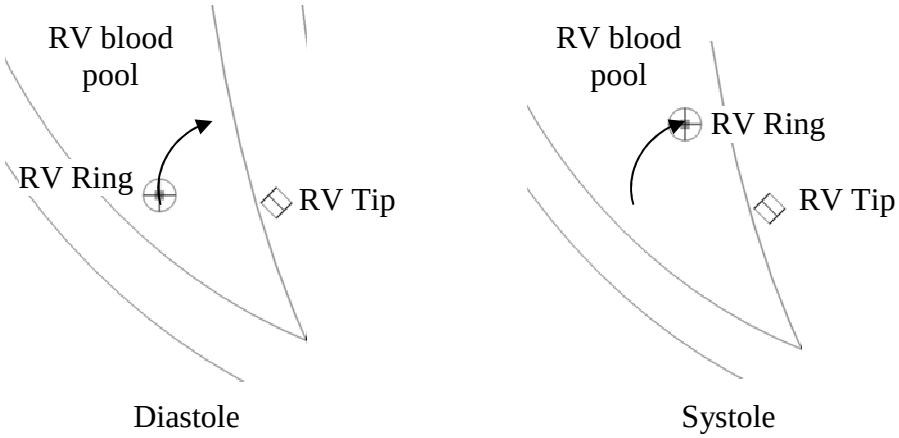

Figure 77: RV lead motion positions at diastole (left) and systole (right)

	Re{**Z**} (Ohms)	Im{**Z**} (Ohms)	G_b (mS)
Diastole	34.36	-1.44	21.42
Systole	33.94	-1.64	19.20

Table 20: RV lead motion model measurements

5.4.8 Lead Position Effects

The effects of lead position were studied by varying the position of the LV and RV leads. The LV lead was placed in the center, higher and lower freewall and also moved around the ventricle toward the RV. The RV lead was raised higher and laterally. The results of these two studies are shown in Figure 78 and Figure 79.

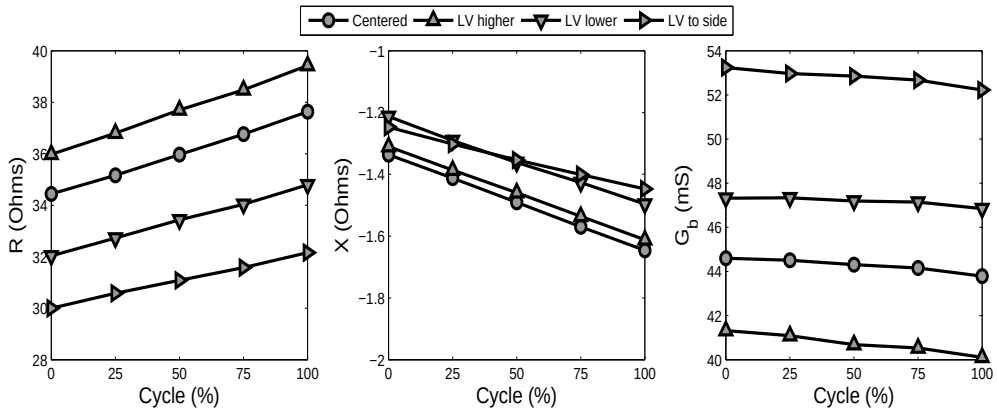

Figure 78: LV lead position effects

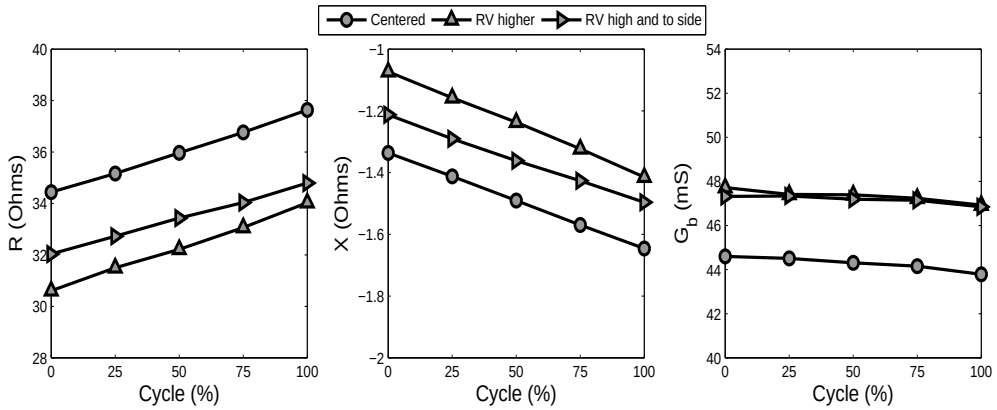

Figure 79: RV lead position effects

The same cyclic trends are observed in each of the lead positions. The highest resistance is measured when the sensing electrodes are far apart. Reactance is highest when the leads are centered.

5.4.9 Effects of the Atria

The effects of the atria on the measured impedance were studied while keeping the LV geometry constant. The atrial geometry is simply a scaled version of the ventricles. This approximation is sufficient to determine whether changes in the atrium

affect the measured impedance. The scaling factor of the atrium was varied from 20 to 60% of the original LV geometry height. The geometry is shown in Figure 80 and the results in Table 21.

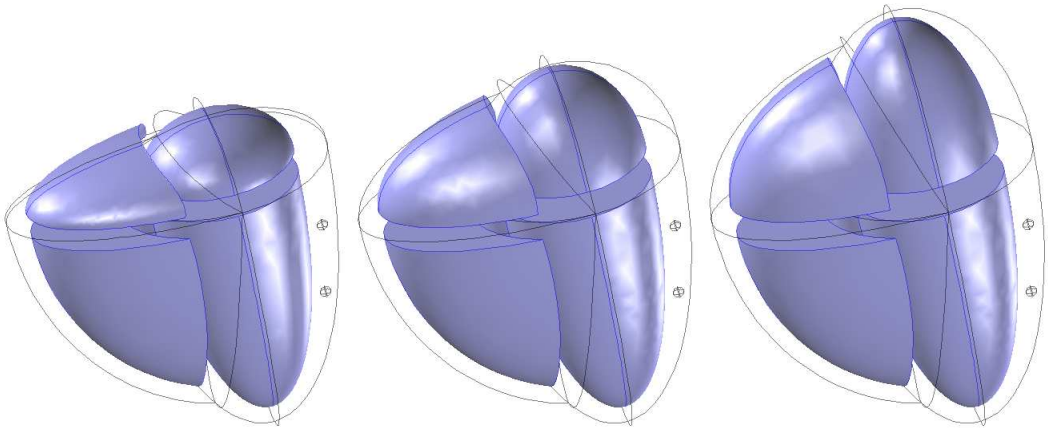

Figure 80: Approximate geometry with atrium

The approximate changes due to the cardiac cycle are 3 - j0.3 Ω and the changes due to the atrium scaling are 0.008 - j0.008 Ω. Changes in the measured impedance due to the atrium are insignificant compared to the cyclic changes.

Scaling (%LV)	Re{**Z**} (Ohms)	Im{**Z**} (Ohms)	G_b (mS)
20	36.102	-1.379	42.18
30	36.044	-1.379	42.28
40	36.002	-1.380	42.37
50	36.024	-1.383	42.38
60	36.094	-1.387	42.32

Table 21: Measurement sensitivity to atrium geometry

Valves were also simulated using cylinders to connect between the atrium and ventricles. The change from open to closed valves resulted in an impedance change of 0.18 - j0.014 Ω. This resulted in an insignificant change in the measured impedance.

5.4.10 Surrounding Tissue Effects

To study the effects of nearby tissue on the measured signal, the conductivity of the surrounding sphere was varied between 0.01 S/m and 0.30 S/m. This parallels an *in vivo* study in pigs using epicardial electrodes where a pleural effusion was simulated by filling the chest cavity with 0.8 S/m saline [3].

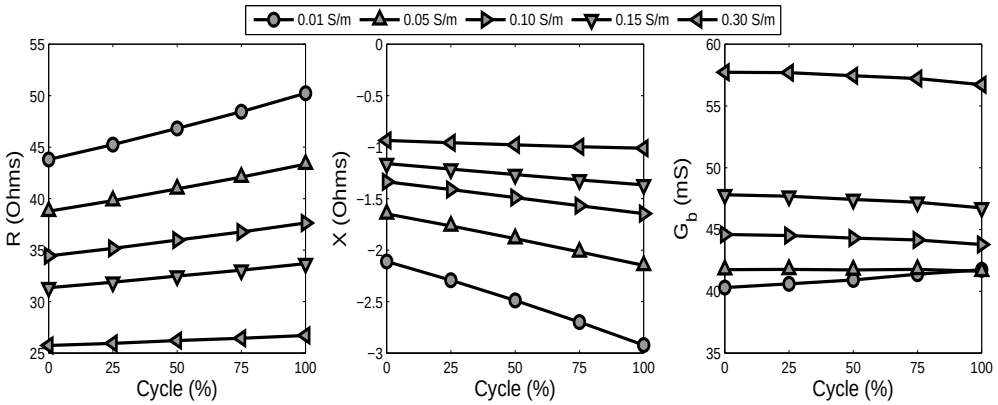

Figure 81: Parametric sweep of surrounding tissue conductivity

As shown, the conductivity of surrounding tissue greatly affects the measurement. As surrounding tissue conductivity increases, the real and imaginary components of impedance decrease in magnitude. The cyclic trend of G_b reverses once the surrounding conductivity reaches 0.01 S/m.

Previous results in pigs did not show a statistically significant change of G_b in the pleural effusion study. Due to this discrepancy, a new model was made to more closely model the pleural effusion study [3]. Electrodes were placed on opposing sides of the LV. Rather than suspending the heart in saline, it was placed on a medium with constant properties. This mimics the heart sitting on the lungs. A saline medium partially surrounds the rest of heart. The geometry is shown in Figure 82 and the results of the study in Figure 83.

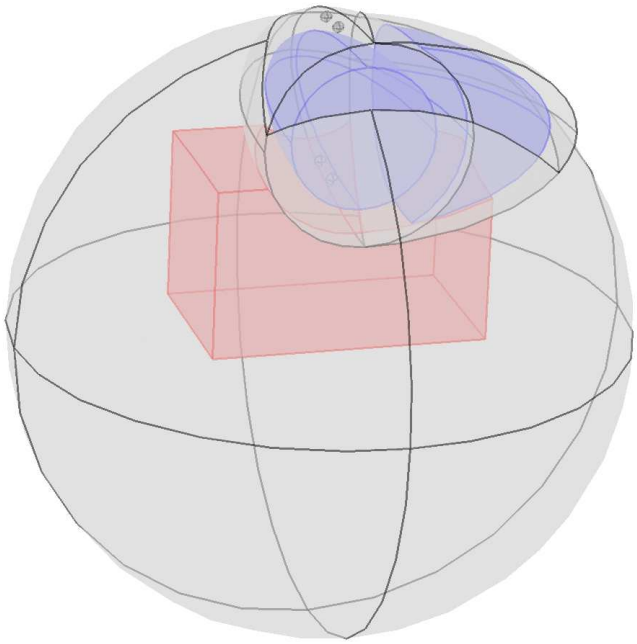

Figure 82: Pleural effusion model

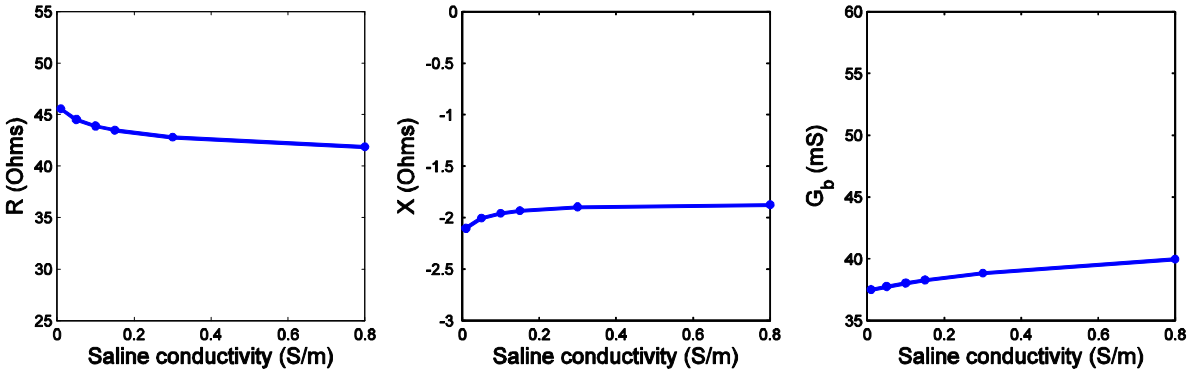

Figure 83: Pleural effusion results

These results are more comparable to the *in vivo* study as they show relatively small changes to the measured signals compared to the results in Figure 81. It is likely the shielding of the electrodes is responsible for the difference between these two studies.

5.4.11 Defibrillator Lead Effects

The majority of BiV pacemakers include defibrillation leads to recover normal sinus rhythm in the case of ventricular fibrillation or unstable tachycardia. This study examines the effect of the large defibrillator lead on the sensitivity field. The sensitivity plot is shown in Figure 84 and the current density in Figure 85. The outline of the shocking lead coil can be seen in the upper part of the RV chamber. Interestingly, the upper region of the coil exhibits a region of high sensitivity, perhaps due to the position of the lower end of the coil in the high sensitivity region near the measurement electrodes. Current is shunted through the coil, creating the higher sensitivity region in the upper region of the coil.

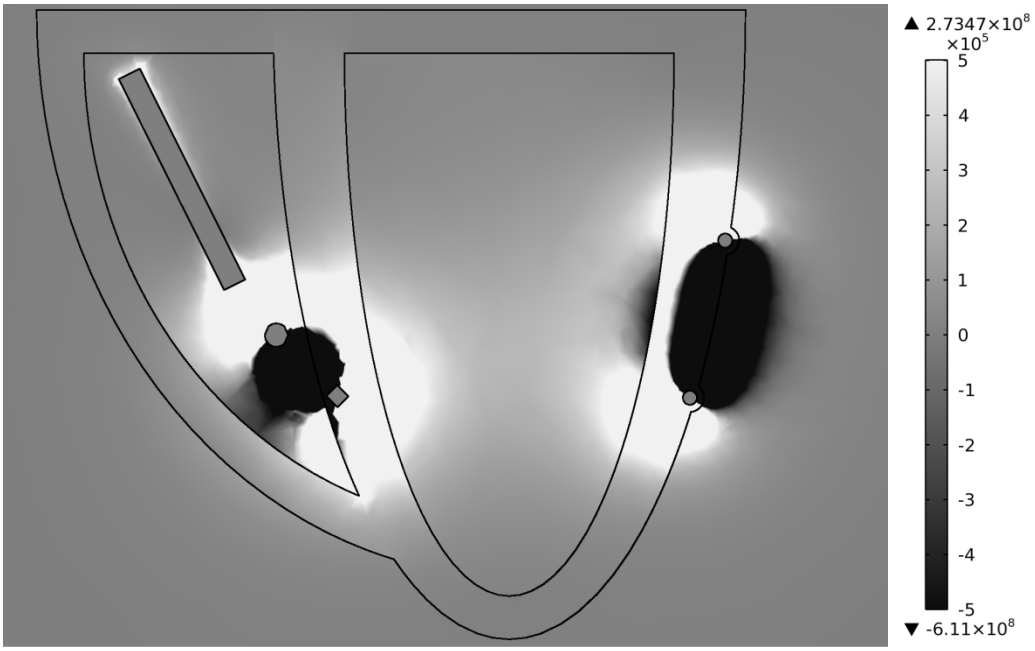

Figure 84: Impedivity-sensitivity product with shocking coil [Ω/m^3]

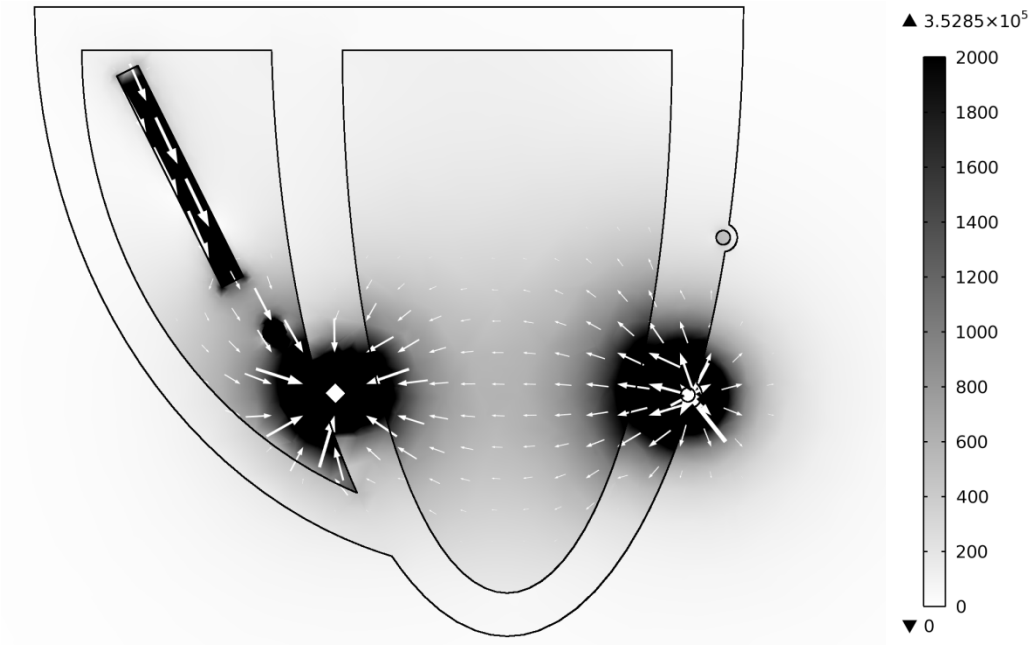

Figure 85: Current density with shocking lead [A/m^2]

	Z_G (Ω)		
Subdomain	**Original model**	**With shocking lead**	**Difference**
LV blood pool	8.65 – j0.12	8.53 – j0.12	0.13 – j0.00
LV muscle	9.91 – j0.55	9.62 – j0.54	0.28 – j0.01
RV blood pool	4.73 – j0.32	4.57 – j0.30	0.16 – j0.02
RV muscle	1.42 – j0.09	1.37 – j0.08	0.07 – j0.00
Surroundings	6.10 – j0.43	6.05 – j0.43	0.05 – j0.00
Total	30.90 – j1.27	30.21 – j1.24	0.69 – j0.04

Table 22: Comparison of cross-chamber measurements with and without a shocking lead

5.4.12Alternative Measurement Configurations

Modification of the spacing between RV and LCV leads was examined to determine if different electrode spacing may enhance the LV portion of the measurement. Analysis was performed using the Geselowitz method to integrate the relative contribution from each subdomain. Additional lead configurations were also analyzed where all four electrodes are located in the LCV.

5.4.12.1 Modified RV and LV Electrode Positions

Models were analyzed with the RV electrodes spaced at 1 cm and 4 cm. LCV electrodes were spaced at 1 cm, 2 cm, and 4 cm. Results from the models are shown in the following tables. Although two configurations increase the contribution of R_b to over 70%, another configuration reduces the contribution from the septum to less than 1%.

	RV / LCV Spacing, Re{Z_G} contribution (%)			
Subdomain	1 cm / 2 cm	4 cm / 2cm	4 cm / 1cm	4 cm / 4 cm
LV blood pool	28.2	40.4	29.3	39.2
LV freewall	13.5	20.5	34.7	13.0
RV blood pool	15.4	-9.7	-5.1	-13.8
RV freewall	4.7	2.4	1.1	4.1
Septum	18.5	16.4	8.0	25.4
Surroundings	19.8	30.0	31.9	32.1

Table 23: Relative contribution to Re{Z_G} with various electrode spacings

	RV / LCV Spacing, $R_{b\text{-}G}$ contribution (%)			
Subdomain	1 cm / 2 cm	4 cm / 2 cm	4 cm / 1 cm	4 cm / 4 cm
LV blood pool	50.2	71.9	54.9	73.4
LV freewall	6.6	11.3	37.3	5.4
RV blood pool	9.6	-8.2	-4.9	-11.2
RV freewall	3.4	-0.8	-0.4	-1.3
Septum	18.9	8.8	4.5	14.7
Surroundings	11.3	17.0	8.6	19.0

Table 24: Relative contribution to R_b with various electrode spacings

	$Re\{Z_G\}$ (Ω)							
	1 cm / 2 cm		4 cm / 2 cm		4 cm / 1cm		4 cm / 4 cm	
Subdomain	Diastole	Systole	Diastole	Systole	Diastole	Systole	Diastole	Systole
LV blood pool	8.67	6.39	7.30	5.48	11.30	7.98	4.23	3.21
LV freewall	4.16	5.60	3.70	5.40	13.38	17.50	1.41	2.02
RV blood pool	4.73	4.98	-1.76	-1.88	-1.95	-2.09	-1.49	-1.58
RV freewall	1.44	1.45	0.43	0.57	0.44	0.56	0.44	0.59
Septum	5.17	7.36	2.96	4.14	3.06	4.30	2.74	3.74
Surroundings	6.08	8.06	5.42	7.32	12.30	15.56	3.47	4.73
Total	30.79	33.83	18.06	21.04	38.53	43.81	10.80	12.72

Table 25: Real part of Geselowitz impedance with different electrode spacings

	$R_{b\text{-}G}$ (Ω)							
	1 cm / 2 cm		4 cm / 2 cm		4 cm / 1cm		4 cm / 4 cm	
Subdomain	Diastole	Systole	Diastole	Systole	Diastole	Systole	Diastole	Systole
LV blood pool	9.73	7.47	7.83	6.21	11.83	8.70	4.52	3.74
LV freewall	1.28	2.59	1.23	2.47	8.02	11.20	0.33	0.60
RV blood pool	1.86	1.84	-0.89	-0.93	-1.05	-1.11	-0.69	-0.72
RV freewall	0.66	0.52	-0.09	-0.14	-0.09	-0.14	-0.08	-0.14
Septum	3.67	5.29	0.95	1.92	0.97	1.99	0.91	1.80
Surroundings	2.19	1.64	1.85	1.33	1.85	0.71	1.17	1.03
Total	19.38	19.34	10.89	10.85	21.54	21.34	6.15	6.31

Table 26: R_b from the Geselowitz impedance with different electrode spacings

5.4.12.2 Tetrapolar LCV Lead

St. Jude recently introduced the first quadrapolar pacing system for BiV pacemakers with the Quartet™ Quadrapolar, left-ventricular pacing lead. This lead includes four electrodes on the LCV lead rather than the traditional two electrode leads. While this product is designed to allow different pacing configurations, the four electrodes may also be used for an impedance measurement. Models were created to quantify the relative contributions from each subdomain using this new LCV lead. Two configurations were modeled with the lead all the way down the lateral wall and one with two electrodes remaining the LCV, see Figure 86. Each configuration was modeled using both 1 cm spacing between stimulating and sensing pairs as well as 0.5 cm spacing.

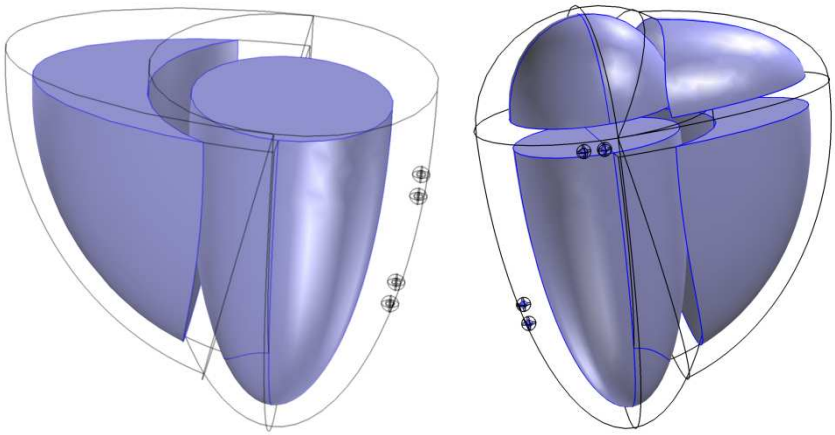

Figure 86: Tetrapolar LCV lead placements

The plot of the real part of the impedivitiy-sensitivity product, Figure 87, shows that most of the sensing field is confined to the LV freewall. The relative contributions from each domain are shown in Table 26 and Table 28, and the actual contributions are shown in Table 29 and Table 30.

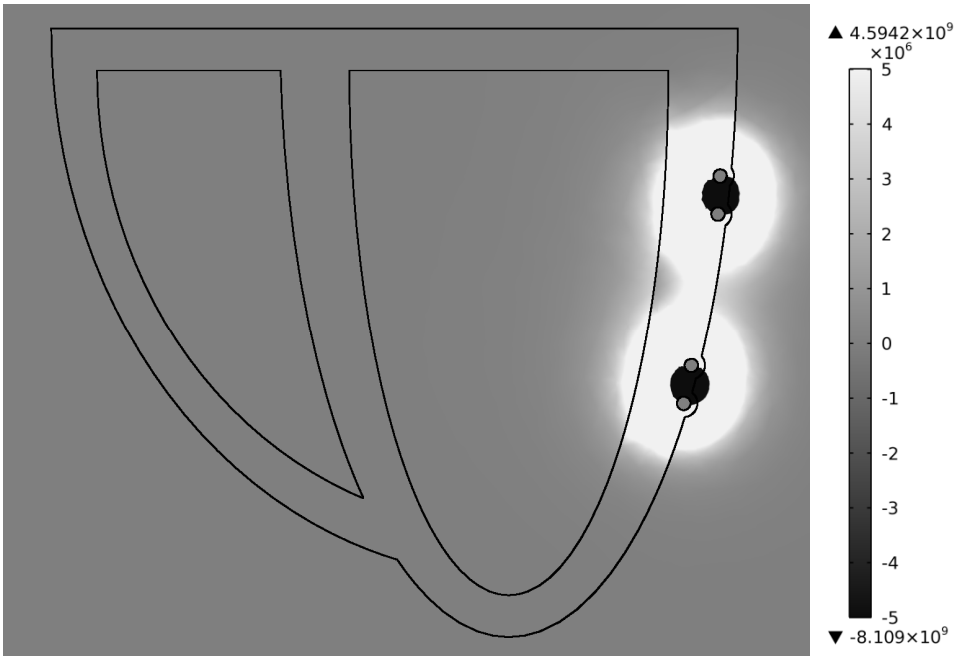

Figure 87: Tetrapolar LCV lead impedivity-sensitivity product [Ω/m^3]

When all electrodes are in the lateral wall, Table 27 shows that the best lead spacing based on relative contribution % is 1 cm between all electrodes, and that R_b focuses the sensitivity towards the LV. With two electrodes in the AV groove and two in the lateral coronary vein, Table 28 shows that both electrode spacings are comparable with regard to the sum of LV free wall and blood pool, and that the 1 cm spacing has higher sensitivity in the LV blood pool than the free wall.

	Contribution (%)			
	1 cm-1 cm-1 cm Spacing		0.5 cm-2 cm-0.5 cm Spacing	
Subdomain	$Re\{Z_G\}$	Rb	$Re\{Z_G\}$	Rb
LV blood pool	15.6	32.5	9.1	22.6
LV free wall	50.8	68.0	58.8	85.8
RV blood pool	0.1	0.2	0.0	0.2
RV free wall	0.0	0.1	0.0	0.1
Septum	0.1	0.4	0.1	0.3
Surroundings	33.4	-1.2	32.0	-9.0

Table 27: Relative contribution to $Re\{Z_G\}$ for all electrodes down lateral wall

	Contribution (%)			
	1 cm-5 cm-1 cm Spacing		0.5 cm-5 cm-0.5 cm Spacing	
Subdomain	$Re\{Z_G\}$	Rb	$Re\{Z_G\}$	Rb
LV blood pool	16.3	30.1	10.1	20.5
LV free wall	33.7	42.1	36.6	53.8
RV blood pool	0.5	0.9	0.5	1.0
RV free wall	0.3	0.7	0.4	0.8
Septum	1.6	2.9	2.2	4.1
LA blood pool	2.7	4.6	1.5	2.9
LA muscle	9.9	11.7	11.3	14.8
RA blood pool	0.1	0.2	0.2	0.3
RA free wall	0.1	0.2	0.2	0.3
Surroundings	34.8	6.6	37.1	1.5

Table 28: Relative contribution to R_b for electrodes in AV groove and lateral wall

Raw measurements show that R_b changes little from diastole to systole, 23.0 Ω to 23.4 Ω and 61.1 Ω to 62.67 Ω with 1 cm-1 cm-1 cm and 0.5 cm-2 cm-0.5 cm spacing in the lateral wall, respectively, and 44.6 Ω to 43.3 Ω and 73.8 Ω to 73.0 Ω with 1 cm-5 cm-1 cm and 0.5 cm-5 cm-0.5 cm spacing, respectively, in the AV groove and lateral coronary vein. This is due to the contributions from the LV freewall and blood pool moving in opposite directions from diastole to systole. Re{**Z**} exhibits a larger change from diastole to systole as shown in Table 29 and Table 30.

	$Re\{Z_G\}$ (Ω)			
	1 cm-1 cm-1 cm Spacing		0.5 cm-2 cm-0.5 cm Spacing	
Subdomain	Diastole	Systole	Diastole	Systole
LV blood pool	7.44	4.5	13.60	8.23
LV freewall	24.28	28.93	88.30	96.56
RV blood pool	0.04	0.05	0.07	0.09
RV freewall	0.01	0.02	0.03	0.03
Septum	0.07	0.13	0.13	0.25
Surroundings	15.94	19.16	48.08	54.84
Total	48.17	53.12	150.40	160.02

Table 29 Real part of Geselowitz impedance for tetrapolar LCV lead down lateral wall

	Re{Z_G} (Ω)			
	1 cm-5 cm-1 cm Spacing		0.5 cm-5 cm-0.5 cm Spacing	
Subdomain	Diastole	Systole	Diastole	Systole
LV blood pool	13.38	8.85	16.36	10.63
LV freewall	27.65	32.22	77.00	83.10
RV blood pool	0.40	0.45	0.47	0.54
RV freewall	0.28	0.33	0.36	0.43
Septum	1.34	1.93	1.81	2.53
LA blood pool	2.25	1.34	2.43	1.44
LA muscle	8.10	9.96	14.62	16.88
RA blood pool	0.11	0.15	0.13	0.17
RA freewall	0.09	0.14	0.13	0.17
Surroundings	28.56	32.61	54.73	60.33
Total	82.16	87.97	168.02	175.87

Table 30: R_b from the Geselowitz impedance for electrodes in AV groove and lateral wall

5.4.13 Discussion

While the effects of surrounding tissue have the potential to greatly affect the impedance measurement, the lungs have relatively low and constant conductivity. The larger vessels are primarily responsible for lung compliance. Capillaries make up most of the lungs have a near-constant flow. While it is unlikely that the bulk conductivity of the lungs would vary enough to have effects on the cyclic impedance measurement, pulmonary edema would likely shift the level of the measurement.

All of the new electrode pacing configurations should be investigated experimentally as they have the potential to improve the measurement. The RV spacing of 4 cm and the LCV of 1 cm may be the largest improvement, as the contribution of the septum is greatly diminished. This is of significant importance because the septum may be the largest source of artifact due to the proximity of the RV lead. The large spacing the RV lead reduces the sensitivity near the septum.

Analysis of tetrapolar leads located in the LV lateral wall and AV groove shows that it may be possible to obtain a volume dependent signal, but the application of the admittance method may not improve the measurement. Although R_b has a higher sensitivity to the LV blood pool and freewall, the signal change from diastole to systole is small. This measurement may be better than magnitude only analysis if a large enough signal to noise ratio can be achieved.

5.5 MRI STUDY

A gated cardiac MRI was performed to construct a mesh that is closer to the exact geometry of the heart. Short-axis slices were acquired using a Siemens TIM TRIO 3T whole-body MRI system at the University of Texas Health Science Center at San Antonio Research Imaging Center. Images were converted to a volumetric mesh using Simpleware (Exeter, United Kingdom).

Cardiac muscle and blood were tagged by hand and then slices were modified to create a smooth mesh. Electrodes were placed using the Simpleware CAD module. LCV electrodes were placed in the LV freewall and RV electrodes were placed in the RV blood pool near the septum. Two models were studied. In both models the RV electrodes were separated by 1 cm. In the first model the LCV leads are separated by 2 cm and in the second 0.5 cm. Meshes were exported and solved using COMSOL.

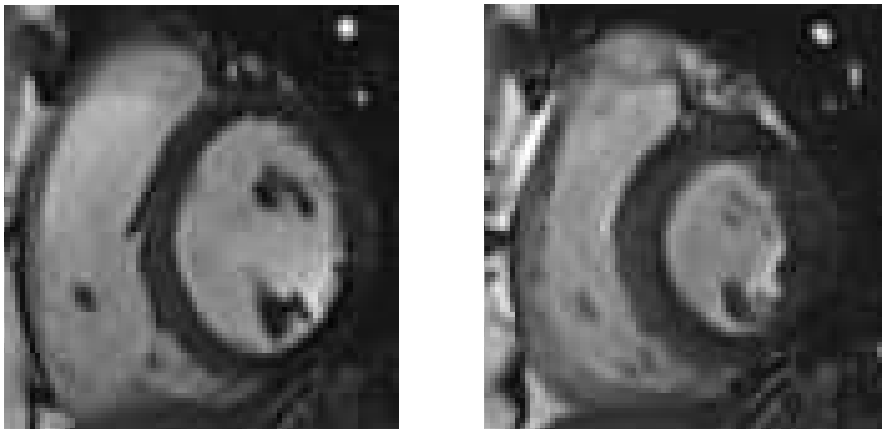

Figure 88: Representative MRI slices at diastole and systole

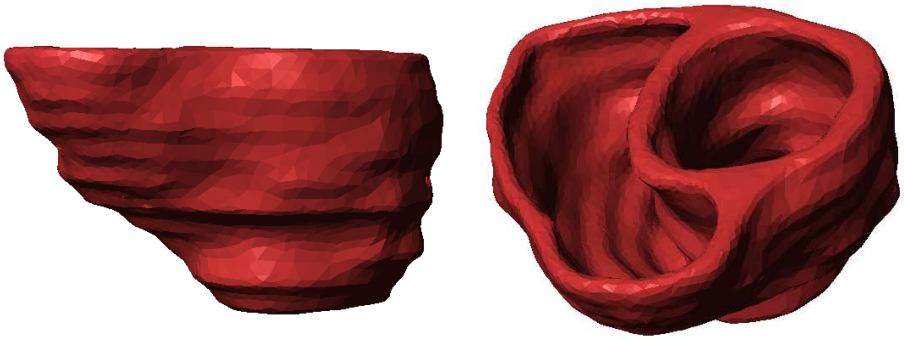

Figure 89: MRI mesh at diastole

There are 91,608 mesh elements which result in 277,002 degrees of freedom. Mesh statistics for the heart at diastole are shown in Table 31.

Number of elements	91,608
Minimum element quality	0.04054
Average element quality	0.6907
Element volume ratio	3.904E-5

Table 31: Mesh statistics for MRI study with 2 cm LCV electrode spacing at diastole

Results of the impedance measurements are shown in Table 32 and Table 33. The 2 cm spacing LCV electrode spacing model results in measurements comparable to

experimental and approximate geometry measurements. The second model with 0.5 cm LCV electrode spacing results in much larger impedances, and the trends from diastole to systole match those of the approximate geometry models. It is not clear why the diastole to systole trend in the measurements from the 2 cm model do not match the other models. The relatively small changes in impedance compared to the 0.5 cm spacing model may be overcome by errors in electrode placement differences between the diastolic and systolic models.

	Re{**Z**} (Ohms)	Im{**Z**} (Ohms)	Gb (mS)
Diastole	35.81	-1.54	45.5
Systole	35.24	-1.85	53.7

Table 32: 2cm LCV electrode spacing measurements with MRI model

	Re{**Z**} (Ohms)	Im{**Z**} (Ohms)	G_b (mS)
Diastole	127.44	-9.14	40.07
Systole	142.00	-11.34	45.29

Table 33: 0.5 cm LCV electrode spacing measurements with MRI model

5.6 DISCUSSION

This numerical model analysis applied the Geselowitz formulation to the admittance method, allowing the spatial contributions to be analyzed for the first time. Analysis was performed on tetrapolar measurements including the murine conductance catheter, a five-segment conductance catheter, and cross-chamber models. The Geselowitz relationship revealed the sensitivity field and the contributions of each subdomain.

Cross-chamber impedance measurements have the potential to aid pacemakers and ICD algorithms in the assessment of cardiac hemodynamics. Analysis of these measurements show that the measured impedance is derived from many sources

including the distance between the pairs of electrodes, the LV blood pool, the RV blood pool, both LV and RV myocardium, the septum, and surrounding tissue. The high concentration of the sensitivity field near the electrodes makes the measurement of LV volume difficult due to dynamic changes in the RV. Movement of the RV lead relative to the endocardium has the potential of increasing or decreasing the signal due to the presence of both positive and negative sensitivity zones. Analysis using the Geselowitz relationship shows that application of the series blood-muscle model results in higher sensitivity to the LV. However, subtraction of the muscle conductance does not completely remove the muscle signal. The inability of the admittance method to fully separate blood and muscle signals is due to the geometry, where blood and muscle are neither in series nor parallel, but a mixture of the two.

Despite the inherent difficulties in cross-chamber impedance measurements, experimental data shows that it has the potential to measure changes in cardiac hemodynamics. Optimization of electrode spacing on the RV and LCV leads shows that improved sensitivity to the LV blood pool can be obtained by lengthening the RV lead and shortening the LCV lead. Another potential measurement technique uses four electrodes on the LCV lead. Experimental investigation is necessary to further study these electrode configurations.

Chapter 6: Conclusion

This work has used numerous methods to analyze bulk measurements and property measurements using the admittance method. The key findings of this work are:

1) The admittance method can successfully be extended to multi-segment conductance catheters for the determination of LV volume.
2) Parasitic circuit elements of admittance probes are responsible for the imaginary component of admittance in saline and can be reduced through reduction of parasitic capacitance.
3) Biventricular pacing leads can be used to monitor LV hemodynamics using the admittance method.
4) In finite element models, the admittance method correctly removes muscle conductance in conductance catheters and improves the spatial sensitivity of cross-chamber measurements using biventricular pacing leads.

For the first time, the admittance method was applied to a multi-segment conductance catheter. Experiments show that it is possible to obtain parallel conductance in real time using the admittance method and that volume derived using Wei's equation is comparable to both 2D crystal derived volume and the traditional magnitude analysis.

The effects of parasitic elements on the calibration of admittance measurements were determined using modeling and experimentation. Results show that interwire capacitance and electrode impedance are responsible for the imaginary component of admittance that is measured in saline. Reduction of this effect can be accomplished through reduction of electrode impedance and/or interwire capacitance. Active probe designs show it is possible to reduce the effects, but they are unable to remove them entirely.

Acute experiments in canines show that biventricular pacing leads can be used to monitor LV hemodynamics more reliably using the admittance method than traditional magnitude only analysis. A good correlation was observed between ΔG_b and LV SV. G_b also tracked LV volume during simulated VT. These results demonstrate the feasibility of incorporating the admittance method into ICD algorithms to decrease inappropriate shocks to patients. This is likely to have the largest impact the admittance method serves to make to clinical applications.

Application of the Geselowitz relation to tetrapolar measurements allows quantification of the spatial sensitivity of the admittance method for the first time. Results show that the admittance method correctly identifies the signal from the LV blood pool using single and multi-segment conductance catheters. Analysis of cross-chamber measurements using biventricular leads show the admittance method focuses the measurement on the LV blood pool.

This work advances the understanding of tetrapolar admittance measurements and explores new applications of the method. Experimental findings using biventricular pacing leads warrant further development of the method and may someday be incorporated into ICDs.

Appendix

A - Porcine Conductance Catheter Data and Analysis

/Pig #/	Folder containing data and analysis files for Pig #.
Pig # - MS Analyze.m	This file can be configured to analyze the data using the admittance method or traditional conductance with the hypertonic saline technique. Conductance to volume can be set to Baan's equation, SV calibration, or Wei's equation.
/Pig # Results/	Folder containing data from analysis, a script to generate high quality figures, and the exported figure images.

B - Infarct Data and Analysis

AFG - Frequency Sweep v1_1.VI	LabVIEW program to sweep frequencies with Agilent 331XX function generator.
Infarct_Study_Results.m	MATLAB code to calculate mean electrical property values and generate figures.

C - Tetrapolar Circuit Models

Full_model_admittance_matrix_vary_freq.m	MATLAB code to sweep frequency with the tetrapolar circuit model.
Full_model_admittance_matrix_vary_Ze.m	Runs the tetrapolar model with three different values for the electrode impedance.
Full_model_admittance_matrix_vary_Cp.m	Runs the model with different values for the interwire capacitance.
Full_model_admittance_matrix_vary_Inductance.m	Runs the model with different values for the wire inductance.

D - Active Surface Probe Design and Analysis

ASP - Large Animal - v1_2 – Schematic.dch	Diptrace PCB schematic for active surface probe.
ASP - Large Animal - v1_2 – Layout.dip	Diptrace layout file.
ASP - Large Animal - v1_3 – Schematic.dch	Schematic for new version of active surface probe with low input-capactiance op-amps.
ASP - Rat - v1_3 – Layout.dip	Layout file for new active surface probe.

E - Biventricular Impedance and Pacing Instrument Design Files

Design files for the instrument used in Chapter 4 are included as an attachment. The instrument includes an impedance measurement using synchronous demodulation at 20 kHz, one surface ECG channel, three intracardiac EGM channels, and three isolated pacing channels.

BiV *Pacemaker Schematic v2_0.sch*	Mentor Graphics PADs schematic
BiV Pacemaker Schematic v1_0.pdf	PDF version of schematic
BiV Pacemaker - Layout 2_1.pcb	Mentor Graphics PADs PCB layout
BiV Pacer BOM v1_0.xls	Bill of materials

F - Stroke Volume Monitoring Experimental Results

/Data and Analysis/	Files related to data analysis and figure generation.
/Statistical Analysis/	R code used to perform statistical analysis on the data.

G - FINITE ELEMENT MODELS

/3D Tetrapolar in Uniform Media/	COMSOL model files for tetrapolar analyzed using the Geselowitz relation in uniform media.
/Approximate Canine Geometry/	Model incorporating approximate geometry from [46] for cross-chamber impedance measurements.
/Canine Conductance Catheter/	Five-segment conductance catheter analyzed using the Geselowitz relation.
/Mouse Conductance Catheter/	Murine conductance catheter models
/MRI Study/	MRI study and resuling model with electrodes configured for a cross-chamber impedance meaurememnt.

References

[1] D. Lloyd-Jones, R. Adams, M. Carnethon *et al.*, "Heart disease and stroke statistics--2009 update: a report from the American Heart Association Statistics Committee and Stroke Statistics Subcommittee," *Circulation,* vol. 119, no. 3, pp. e21-181, 2009 Jan 27 (Epub 2008 Dec, 2009.

[2] J. E. Porterfield, A. T. G. Kottam, K. Raghavan *et al.*, "Dynamic correction for parallel conductance, G(P), and gain factor, alpha, in invasive murine left ventricular volume measurements," *Journal of Applied Physiology,* vol. 107, no. 6, pp. 1693-1703, Dec, 2009.

[3] J. E. Porterfield, E. R. Larson, J. T. Jenkins *et al.*, "Left ventricular epicardial admittance measurement for detection of acute LV dilation," *Journal of Applied Physiology,* vol. 110, no. 3, pp. 799-806, Mar, 2011.

[4] J. D. Mishkin, S. J. Saxonhouse, G. W. Woo *et al.*, "Appropriate Evaluation and Treatment of Heart Failure Patients After Implantable Cardioverter-Defibrillator Discharge Time to Go Beyond the Initial Shock," *Journal of the American College of Cardiology,* vol. 54, no. 22, pp. 1993-2000, Nov 24, 2009.

[5] S. J. Connolly, A. P. Hallstrom, R. Cappato *et al.*, "Meta-analysis of the implantable cardioverter defibrillator secondary prevention trials," *European Heart Journal,* vol. 21, no. 24, pp. 2071-2078, Dec, 2000.

[6] T. M. Hurst, M. Hinrichs, C. Breidenbach *et al.*, "Detection of myocardial injury during transvenous implantation of automatic cardioverter-defibrillators," *Journal of the American College of Cardiology,* vol. 34, no. 2, pp. 402-408, Aug, 1999.

[7] J. E. Poole, G. W. Johnson, A. S. Hellkamp *et al.*, "Prognostic importance of defibrillator shocks in patients with heart failure," *New England Journal of Medicine,* vol. 359, no. 10, pp. 1009-1017, Sep 4, 2008.

[8] J. P. Daubert, W. Zareba, D. S. Cannom *et al.*, "Inappropriate implantable cardioverter-defibrillator shocks in MADIT II," *Journal of the American College of Cardiology,* vol. 51, no. 14, pp. 1357-1365, Apr 8, 2008.

[9] B. L. Wilkoff, B. D. Williamson, R. S. Stern *et al.*, "Strategic programming of detection and therapy parameters in implantable cardioverter-defibrillators reduces shocks in primary prevention patients - Results from the PREPARE (Primary Prevention Parameters Evaluation) study," *Journal of the American College of Cardiology,* vol. 52, no. 7, pp. 541-550, Aug 12, 2008.

[10] R. C. Klein, M. H. Raitt, B. L. Wilkoff *et al.*, "Analysis of implantable cardioverter defibrillator therapy in the Antiarrhythmics Versus Implantable Defibrillators (AVID) Trial," *Journal of cardiovascular electrophysiology,* vol. 14, no. 9, pp. 940-8, 2003-Sep, 2003.

[11] G. Kaye, D. Edgar, T. Mudawi *et al.*, "Can transventricular intracardiac impedance measurement discriminate haemodynamically unstable ventricular arrhythmias in human?," *Europace,* vol. 9, no. 2, pp. 122-126, Feb, 2007.

[12] K. Raghavan, J. E. Porterfield, A. T. G. Kottam *et al.*, "Electrical Conductivity and Permittivity of Murine Myocardium," *IEEE Transactions on Biomedical Engineering,* vol. 56, no. 8, pp. 2044-2053, Aug, 2009.

[13] R. Magjarevic, and B. Ferek-Petric, "Implantable Cardiac Pacemakers-50 Years from the First Implantation," *Zdravniski Vestnik-Slovenian Medical Journal,* vol. 79, no. 1, pp. 55-67, Jan, 2010.

[14] C. J. Finelli, L. A. Dicarlo, J. M. Jenkins *et al.*, "Effects of Increased Heart-rate and Sympathetic Tone on Intraventricular Electrogram Morphology," *American Journal of Cardiology,* vol. 68, no. 13, pp. 1321-1328, Nov 15, 1991.

[15] C. D. Swerdlow, M. L. Brown, K. Lurie *et al.*, "Discrimination of ventricular tachycardia from supraventricular tachycardia by a downloaded wavelet-transform morphology algorithm: A paradigm for development of implantable cardioverter defibrillator detection algorithms," *Journal of Cardiovascular Electrophysiology,* vol. 13, no. 5, pp. 432-441, May, 2002.

[16] J. N. Koneru, C. D. Swerdlow, M. A. Wood *et al.*, "Minimizing Inappropriate or "Unnecessary" Implantable Cardioverter-Defibrillator Shocks Appropriate Programming," *Circulation-Arrhythmia and Electrophysiology,* vol. 4, no. 5, pp. 778-790, Oct, 2011.

[17] C. Stahl, W. Beierlein, T. Walker *et al.*, "Intracardiac impedance monitors hemodynamic deterioration in a chronic heart failure pig model," *Journal of Cardiovascular Electrophysiology,* vol. 18, no. 9, pp. 985-990, Sep, 2007.

[18] M. Bocchiardo, D. M. Z. Vilsendorf, C. Militello *et al.*, "Intracardiac impedance monitors stroke volume in resynchronization therapy patients," *Europace,* vol. 12, no. 5, pp. 702-707, 2010.

[19] M. Bocchiardo, D. M. Z. Vilsendorf, C. Militello *et al.*, "Resynchronization therapy optimization by intracardiac impedance," *Europace,* vol. 12, no. 11, pp. 1589-1595, Nov, 2010.

[20] C. Stahl, T. Walker, A. Straub *et al.*, "Assessing Acute Ventricular Volume Changes by Intracardiac Impedance in a Chronic Heart Failure Animal Model," *Pace-Pacing and Clinical Electrophysiology,* vol. 32, no. 11, pp. 1395-1401, Nov, 2009.

[21] M. Maines, D. Catanzariti, C. Cemin *et al.*, "Usefulness of intrathoracic fluids accumulation monitoring with an implantable biventricular defibrillator in reducing hospitalizations in patients with heart failure: A case-control study," *Journal of Interventional Cardiac Electrophysiology,* vol. 19, pp. 201-207, 2007.

[22] J. Ritzema, R. Troughton, I. Melton *et al.*, "Physician-Directed Patient Self-Management of Left Atrial Pressure in Advanced Chronic Heart Failure," *Circulation,* vol. 121, no. 9, pp. 1086-1095, 2010.

[23] L. Zipes, Bonow, Braudwald, "Braunwald's Heart Disease. A Textbook of Cardiovascular Medicine," Saunders (Elsevier), 2005, p. 540.

[24] R. C. Bourge, W. T. Abraham, P. B. Adamson *et al.*, "Randomized controlled trial of an implantable continuous hemodynamic monitor in patients with advanced heart failure - The COMPASS-HF study," *Journal of the American College of Cardiology,* vol. 51, no. 11, pp. 1073-1079, 2008.

[25] C. M. Yu, L. Wang, E. Chau *et al.*, "Intrathoracic impedance monitoring in patients with heart failure - Correlation with fluid status and feasibility of early warning preceding hospitalization," *Circulation,* vol. 112, no. 6, pp. 841-848, 2005.

[26] L. Wang, "Fundamentals of intrathoracic impedance monitoring in heart failure," *American Journal of Cardiology,* vol. 99, no. 10A, pp. 3G-10G, 2007.

[27] P. Delnoy, J. P. Ottervanger, H. O. Luttikhuis *et al.*, "Pressure-volume loop analysis during implantation of biventricular pacemaker/cardiac resynchronization therapy device to optimize right and left ventricular pacing sites," *European Heart Journal,* vol. 30, no. 7, pp. 797-804, 2009.

[28] P. Steendijk, S. A. F. Tulner, M. Wiemer *et al.*, "Pressure-volume measurements by conductance catheter during cardiac resynchronization therapy," *European Heart Journal Supplements,* vol. 6, no. D, pp. D35-D42, 2004.

[29] J. Baan, J. Koops, E. T. Vandervelde *et al.*, "Dynamic Absolute Left-Ventricular Volume Measured with the Conductance Catheter," *Circulation,* vol. 64, no. 4, pp. 177-177, 1981.

[30] E. Larson, "Design and Analysis of an Admittance-Based, Isolated, Multi-Segment Pressure-Volume Instrument for Human Use," Master's Thesis, Electrical Engineering, The University of Texas at Austin, Austin, 2008.

[31] C. L. Wei, J. W. Valvano, M. D. Feldman *et al.*, "Nonlinear conductance-volume relationship for murine conductance catheter measurement system," *IEEE Transactions on Biomedical Engineering,* vol. 52, no. 10, pp. 1654-1661, Oct, 2005.

[32] X. M. Gao, A. M. Dart, E. Dewar *et al.*, "Serial echocardiographic assessment of left ventricular dimensions and function after myocardial infarction in mice," *Cardiovascular Research,* vol. 45, no. 2, pp. 330-338, Jan 14, 2000.

[33] A. Kottam, "Measurement of Electrical Admittance to Study the Onset and Progression of Myocardial Ischemia," Biomedical Engineering, The University of Texas at Austin, 2007.

[34] A. Kottam, "Determination of Parasitic Circuit Elements in Cardiac Conductance Catheters," Electrical Engineering, The University of Texas at Austin, Austin, 2003.

[35] G. J. Brug, A. L. G. Vandeneeden, M. Sluytersrehbach *et al.*, "The analysis of electrode impedances complicated by the presence of a constant phase element," *Journal of Electroanalytical Chemistry,* vol. 176, no. 1-2, pp. 275-295, 1984, 1984.

[36] R. W. Parker. "Circuits I Have Known," 8/17/2011, 2011; http://controlsignalconverter.com/docs/circuits_i_have_known.pdf.

[37] T. J. Kao, G. J. Saulnier, D. Isaacson *et al.*, "A Versatile High-Permittivity Phantom for EIT," *IEEE Transactions on Biomedical Engineering*, vol. 55, no. 11, pp. 2601-2607, Nov, 2008.

[38] S. Rush, J. A. Abildskov, and McFeer, "Resistivity of body tissues at low frequencies," *Circulation research*, vol. 12, pp. 40-50, 1963, 1963.

[39] S. A. P. Haddad, R. P. M. Houben, and W. A. Serdijn, "The evolution of pacemakers," *IEEE Engineering in Medicine and Biology Magazine*, vol. 25, no. 3, pp. 38-48, May-Jun, 2006.

[40] J. W. Gaynor, M. P. Feneley, S. A. Gall *et al.*, "Measurement of left-ventricular volume in normal and volume-overloaded canine hearts," *American Journal of Physiology*, vol. 266, no. 1, pp. H329-H340, Jan, 1994.

[41] J. G. Lainchbury, D. M. Meyer, M. Jougasaki *et al.*, "Effects of adrenomedullin on load and myocardial performance in normal and heart-failure dogs," *American Journal of Physiology-Heart and Circulatory Physiology*, vol. 279, no. 3, pp. H1000-H1006, Sep, 2000.

[42] R Development Core Team, "R: A Language and Environment for Statistical Computing,," R Foundation for Statistical Computing, 2012.

[43] D. Bates, M. Maechler, and B. Bolker, "lme4: Linear mixed-effects models using S4 classes," R package version 0.999375-42 http://CRAN.R-project.org/package=lme4, 2011.

[44] M. Wathen, "Implantable cardioverter defibrillator shock reduction using new antitachycardia pacing therapies," *American heart journal*, vol. 153, no. 4 Suppl, pp. 44-52, 2007-Apr, 2007.

[45] B. L. Wilkoff, M. Hess, J. Young *et al.*, "Differences in tachyarrhythmia detection and implantable cardioverter defibrillator therapy by primary or secondary prevention indication in cardiac resynchronization therapy patients," *Journal of Cardiovascular Electrophysiology*, vol. 15, no. 9, pp. 1002-1009, Sep, 2004.

[46] J. S. Rankin, P. A. McHale, C. E. Arentzen *et al.*, "3 Dimensional Dynamic Geometry of the Left-Ventricle in Conscious Dogs," *Circulation Research*, vol. 39, no. 3, pp. 304-313, 1976.

[47] D. Geselowitz, "Application of electrocardiographic lead theory to impedance plethysmography," *IEEE Transactions on Biomedical Engineering*, vol. BM18, no. 1, pp. 38-&, 1971.

[48] S. Grimnes, and O. G. Martinsen, "Sources of error in tetrapolar impedance measurements on biomaterials and other ionic conductors," *Journal of Physics D-Applied Physics*, vol. 40, no. 1, pp. 9-14, Jan 7, 2007.

[49] J. Lehr, "Vector derivation useful in impedance plethysmographic field calculations," *IEEE Transactions on Biomedical Engineering*, vol. BM19, no. 2, pp. 156-157, 1972, 1972.

[50] J. Baan, E. T. Vandervelde, H. G. Debruin *et al.*, "Continuous Measurement of Left-Ventricular Volume in Animals and Humans by Conductance Catheter," *Circulation*, vol. 70, no. 5, pp. 812-823, 1984.

[51] S. Gabriel, R. W. Lau, and C. Gabriel, “The dielectric properties of biological tissues .2. Measurements in the frequency range 10 Hz to 20 GHz,” *Physics in Medicine and Biology,* vol. 41, no. 11, pp. 2251-2269, Nov, 1996.